Int. J. Advanced Design and Manufacturing Technology, 2025, Vol. 18, No. 2, pp. 1-8

DOI: *ISSN: 2252-0406* *https://admt.isfahan.iau.ir*

Nonlinear Wheel Slip Control of Electric Vehicles with In-Wheel BLDC Motors

Majid Majidi[1, *]
Department of Mechanical Engineering, Qa.C., Islamic Azad University, Qazvin, Iran
E-mail: majid.majidi@iau.ac.ir
*Corresponding author

Pouyan Ahmadizadeh[2]
School of Automotive Engineering, Iran University of Science and Technology, Tehran, Iran
E-mail: p.ahmadizadeh@gmail.com

Received: 10 November 2024, Revised: 4 February 2025, Accepted: 10 March 2025

Abstract: This paper introduces a vehicle wheel slip tracking using an in-wheel BLDC (brushless direct current) motor. The control objective is to track a reference input wheel slip. The control architecture consists of a two-layer structure. In the upper level of the control system, the controller design is based on a sliding mode control strategy and generates the required torque for each wheel as the wheel slip tracks the reference value. In the lower level, the torque controller is a current controller with the duty cycle of the PWM (pulse width modulation) pulses to achieve the desired torque demanded by the upper level. In torque controller, a BLDC motor controller with a three-phase inverter is designed using Hall Effect sensor feedback and current sensors. The design is performed so that the wheel slip tracks any reference input wheel slip. Simulations are performed to demonstrate the effectiveness of the proposed two-layer controller.

Keywords: BLDC Motor, Sliding Mode Control, Wheel Slip Control

Biographical notes: Majid Majidi received his PhD in Automotive Engineering from Iran University of Science and Technology in 2015. He has worked as an assistant professor at the Department of Mechanical Engineering, Qazvin Islamic Azad University, since 2015. His current research interests include vehicle dynamics and control, modeling, simulation, and control of hybrid and electric vehicles. **Pouyan Ahmadizeh** received his PhD in Automotive Engineering from Iran University of Science and Technology in 2017. His current research interests include vehicle dynamics and control, hybrid and electric vehicles powertrain.

Research paper

COPYRIGHTS
© 2025 by the authors. Licensee Islamic Azad University Isfahan Branch. This article is an open access article distributed under the terms and conditions of the Creative Commons Attribution 4.0 International (CC BY 4.0) (https://creativecommons.org/licenses/by/4.0/)

1 INTRODUCTION

Electric motors have good performance for motion control applications since their torque response is quite fast and accurate. The application of in-wheel motors in hybrid or electric vehicles is an object of intense research activities, for some earlier studies [1-4]. In this way, the motor torque of each wheel can be controlled independently without requiring any additional actuators. Such an arrangement permits dynamic control to be realized using only software and delivers the benefits of the inherently rapid, precise torque controllability. For the lower layer controller, slip control is being done with the use of vehicle stability control known as DYC (direct yaw-moment control) in EVs (electric vehicles) [5-6]. In this approach, by using in-wheel motors, the anti-directional torque generation is applied on the left and right wheels [7-8]. The main difficulty arising in the design of a wheel slip control is due to the strong nonlinearity and uncertainty in the problem [9]. Therefore, sliding mode control is a preferable approach for this kind of problem because of its robustness. Sliding mode controllers have been designed previously for the purpose of controlling wheel slip [10]. For tracking a reference wheel slip by electrical motor, information on the longitudinal (tractive/braking) tire force of each wheel must be supplied to the controller. Since electrical motor torque is easily comprehensible, there exists little uncertainty in driving or braking torque generated by the motor, compared to that of an internal combustion engine or hydraulic brake. Therefore, a simple driving force observer can achieve a real-time observation of the driving/braking force between the tire and the road surface [11-12]. This paper describes the control method devised to enhance slip tracking for traction application of EVs. This paper proposes a wheel slip control method based on the feedback of wheel angular velocity, which is easily measured. If every wheel has a driving motor, this slip controller can be applied to every wheel. By maintaining the wheel slip at the desired level, the desired longitudinal (tractive) tire force is generated, and the desired longitudinal speed due to driving command is, therefore, achieved. The control algorithm developed in this paper uses a nonlinear tire model to provide the tire forces for simulation purposes.

2 MODELING

In this section, the dynamic models of the vehicle, wheel, and BLDC motors are presented to set up the control problem and simulation.

Vehicle Modeling

Vehicle models are available with several complexities. More complex models could have accurate results but take more simulation time. On the other hand, less complex models are simple for simulation but might have less accuracy. The models with basic properties of the system have often been preponderant for many applications and have reliable results. The vehicle model considered here for simulation purposes consists of 8 degrees of freedom (DOF). These include longitudinal and lateral motions, yaw and body roll motions, as well as the rotational dynamics of the four wheels. In addition, the steering system is assumed to be stiff, and the drive line dynamics is neglected for simplicity (driving/braking torques are thus applied directly to the wheels) [13]. Figure 1 shows the free-body form of the vehicle model, and “Fig. 2” shows the layout of the wheel dynamics.

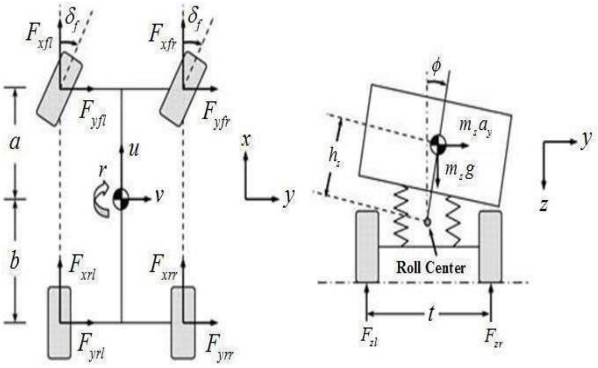

Fig. 1 Vehicle model in free-body form [14].

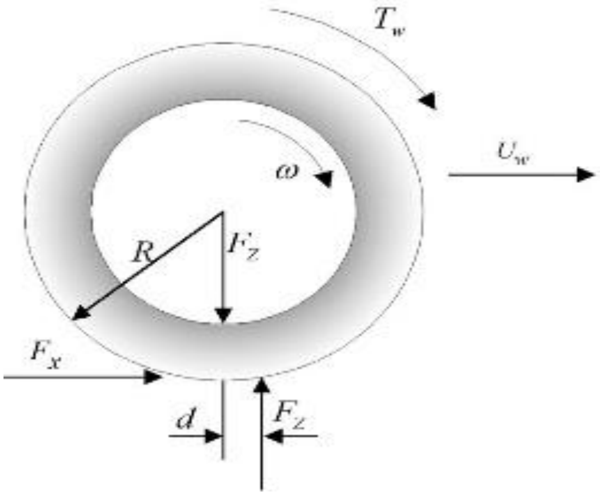

Fig 2. Wheel dynamics layout [14].

The Equation of wheel dynamics is needed for sliding mode control, that is:

$$\dot{\omega} = \frac{1}{J_w}\left(T_w - F_x R - F_z d\right) \quad (1)$$

Where J_w is the mass moment inertia of the wheel and connecting parts about the axis of rotation, T_w is the wheel torque, F_z and F_z are the wheel longitudinal and normal forces respectively, R is the wheel radius and d is the distance between the spin axis and the road vertical reaction force.

Tire Model

In order to simulate the tire model, the nonlinear magic formula tire [15] model with combined longitudinal and lateral slip is employed due to the capability of this model to simulate the limit handling situations where strong nonlinearity is present.

BLDC Motor Model

BLDC motor [16] is one kind of permanent magnet synchronous motor, with permanent magnets on the rotor and trapezoidal shape back EMF (electromotive forces). The BLDC motor employs a DC power supply switched to the stator phase windings of the motor by power devices, the switching sequence being determined from the rotor position. The phase current of BLDC motor, typically in a rectangular shape, is synchronized with the back EMF to produce constant torque at a constant speed. BLDC motors have higher efficiency compared with brushed DC motor due to the elimination of magnetizing current and copper loss in the rotor. It is also easier to achieve high-performance torque control with them. Owing to these advantages, BLDC motors have been widely used in a variety of applications in industrial automation and consumer electric appliances. Recent advancements in permanent magnetic materials have made the PM (permanent magnet) motor a great candidate for traction motors in electrical vehicle applications. The BLDC motor used here has 4 magnetic pole pairs on the rotor and a three-phase star connected with windings on stator. The governing Equations of BLDC motor can be represented as:

$$\begin{cases} \dfrac{d}{dt} i_a = \dfrac{1}{3L_s}\left(2V_{ab} + V_{bc} - 3R_s i_a - 2E_a + E_b + E_c\right) \\ \dfrac{d}{dt} i_b = \dfrac{1}{3L_s}\left(-V_{ab} + V_{bc} - 3R_s i_b + E_a - 2E_b + E_c\right) \\ \dfrac{d}{dt} i_c = -\dfrac{d}{dt}\left(i_a + i_b\right) \end{cases} \quad (2)$$

Where V_{ab} and V_{bc} are '*ab*' and '*bc*' phase to phase voltages, R_s and L_s are phase resistance and inductance; i_a , i_b , and i_c are phase currents and E_a, E_b, and E_c are back EMFs. The induced EMF are all assumed to be trapezoidal, given by:

$$\begin{cases} E_a = p\lambda_m \phi_a\left(\theta_e\right)\omega_m \\ E_b = p\lambda_m \phi_b\left(\theta_e\right)\omega_m \\ E_c = p\lambda_m \phi_c\left(\theta_e\right)\omega_m \end{cases} \quad (3)$$

Where λ_m is amplitude of the flux induced by the permanent magnets of the rotor in the stator phases; p is number of pole pairs; $\phi_a\left(\theta_e\right), \phi_b\left(\theta_e\right)$, and $\phi_c\left(\theta_e\right)$ are functions having the same shapes as back EMF with a maximum magnitude of ± 1. Electrical rotor position θ_e and rotor speed ω_e can be defined as:

$$\begin{cases} \theta_e = p\theta_m \\ \omega_e = p\omega_m \end{cases} \quad (4)$$

Where θ_m and ω_m are mechanical rotor angular position and angular speed, respectively. The generated electromagnetic torque is given by:

$$T_e = \frac{E_a i_a + E_b i_b + E_c i_c}{\omega_m} = p\lambda_m\left(\phi_a i_a + \phi_b i_b + \phi_c i_c\right) \quad (5)$$

The mechanical angular acceleration of rotor is given by:

$$\dot{\omega}_m = \frac{1}{J_m}\left(T_e - B_m\omega_m - T_m\right) \quad (6)$$

Where J_m is the mass moment inertia of the rotor about the axis of rotation, B_m is viscous friction coefficient and T_m is shaft mechanical torque applied on rotor. The parameters characterizing BLDC motor are shown in "Table 1".

Table1 Parameters characterizing BLDC motor

V_{dc}	L_s	λ_m	R_s	p
240	8.5e-3	0.192	0.05	4

3 CONTROLLER DESIGN

Upper Layer Controller

The controller gives the desired torque that BLDC motor should produce. To improve the system's robustness, given the presence of modeling uncertainties, a sliding mode controller (SMC) has been considered. The BLDC motor is connected to a reduction gear system, so the angular speed and torque of the motor and wheel are related by:

$$\omega = \frac{\omega_m}{n} \quad T_w = nT_m \quad (7)$$

Where n is the reduction ratio. Substituting "Eqs. (6) and (7)" into "Eq. (1)" yields:

$$\dot{\omega}=\frac{1}{J_{eq}}\left(nT_e-B_{eq}\omega-T_L\right) \tag{8}$$

Where:

$$J_{eq}=J_w+n^2J_m \quad B_{eq}=n^2B_m \quad T_L=F_xR+F_zd$$

The wheel slip in the vehicle accelerating mode is given as:

$$\lambda=1-\frac{U_w}{R\omega} \tag{9}$$

Differentiating "Eq. (9)" with respect to time gives the derivative form:

$$\dot{\lambda}=\frac{U_w}{R\omega^2}\dot{\omega}-\frac{\dot{U}_w}{R\omega} \tag{10}$$

Substituting "Eq. (8)" into "Eq. (10)" and using the longitudinal acceleration of the vehicle instead of a wheel, the nonlinear first-order differential Equation of wheel slip is obtained as:

$$\dot{\lambda}=\frac{(1-\lambda)}{J_{eq}\omega}\left(nT_e-B_{eq}\omega-T_L-\frac{J_{eq}}{(1-\lambda)}\frac{a_x}{R}\right) \tag{11}$$

The control objective is to drive the state λ to the reference value λ_d. In accordance with the typical methodology of the design of the SMC system, the following definition for the sliding surface s has been given:

$$s=\lambda-\lambda_d \tag{12}$$

The sliding law is defined as [17]:

$$\dot{s}=-K\,\mathrm{sgn}(s) \tag{13}$$

Where, K is the controller gain and the discontinuous switching function $\mathrm{sgn}(s)$ can result in chattering during the sliding motion. In general, chattering must be eliminated for the controller to perform properly. A solution to this problem is to replace the discontinuous switching with smooth, continuous switching, such as the saturation function defined as:

$$\mathrm{sat}\left(\frac{s}{\phi}\right)=\begin{cases}\mathrm{sgn}(s) & \left|\frac{s}{\phi}\right|>1\\ \frac{s}{\phi} & \left|\frac{s}{\phi}\right|<1\end{cases} \tag{14}$$

Where ϕ, is a design parameter denoting the boundary layer thickness. The sliding mode controller law could be stated by using "Eqs. (11), (12), (13), and (14)" as:

$$\begin{aligned}T_e=\frac{1}{n}\{&B_{eq}\omega+\frac{J_{eq}}{(1-\lambda)}\frac{a_x}{R}+T_L+\frac{J_{eq}\omega}{(1-\lambda)}\dot{\lambda}_d\\&-\frac{J_{eq}\omega}{(1-\lambda)}K\ \mathrm{sat}\left(\frac{\lambda-\lambda_d}{\phi}\right)\}\end{aligned} \tag{15}$$

The torque given by "Eq. (15)" is the desired value for the lower controller, which will be described in the next section.

Lower Layer controller

Figure 3 illustrates the block diagram of a torque control scheme for a BLDC motor drive.

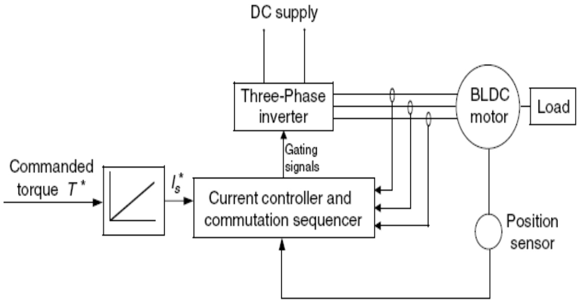

Fig. 3 Torque control of a BLDC motor drive [1].

The desired current I_s^* is derived from the commanded torque T^* through the upper layer controller. The current controller and commutation sequencer receive the desired current I_s^* position information from the position sensors, and the current feedback through current transducers, and then produce gating signals. These gating signals are sent to the three-phase inverter (power converter) to produce the phase current desired by the BLDC machine. The three-phase inverter consists of six transistors connected in a bridge form. The structure of the inverter is shown in "Fig. 4". The same information is presented in "Table 2".

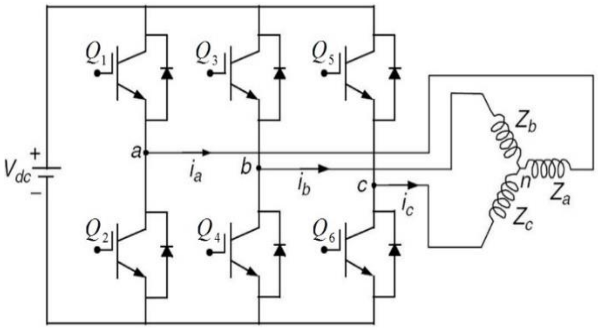

Fig. 4 Three-phase BLDC Power Stage.

Table2 Six step commutation sequence

Hall effect sensor value ($H_aH_bH_c$)	Phase	Switches
101	*a-b*	Q_1; Q_4
100	*a-c*	Q_1; Q_6
110	*b-c*	Q_3; Q_6
010	*b-a*	Q_3; Q_2
011	*c-a*	Q_5; Q_2
001	*c-b*	Q_5; Q_4

The BLDC motor is equipped with three Hall effect sensors. This signal is very useful to control directly the power switches. The Hall-effect sensors produce three 180-degree (electrical) overlapping signals as shown in "Fig. 4". The Hall effect signal provides a logical indication of the back EMF positioning; thus, it provides six mandatory commutation points. The Hall effect sensor outputs are directly connected to the current controller. These signals must be decoded before being applied to the switches to generate the necessary switching sequence as per commutation.

Figure 5 and "Table 2" show that during any 120-degree interval of electrical rotation, two phases are conducting, so from "Eq. (5)", the desired current of torque control is obtained as [16]:

$$I_s^* = \frac{T^*}{2p\lambda_m} \tag{16}$$

By multiplying the desired current I_s^* with the decoded Hall effect sensor signals, the desired current in each of the three phases can be obtained. The PWM width is determined by comparing the measured actual current with the desired reference current in any phase. The logic used by the current controller is to drive the actual current to the desired value. For example, the controller that controls phase '*a*', it checks to see whether the actual current in phase '*a*' is greater than the required current; if it is, then it will activate transistor Q_2. Otherwise, it will activate transistor Q_1.

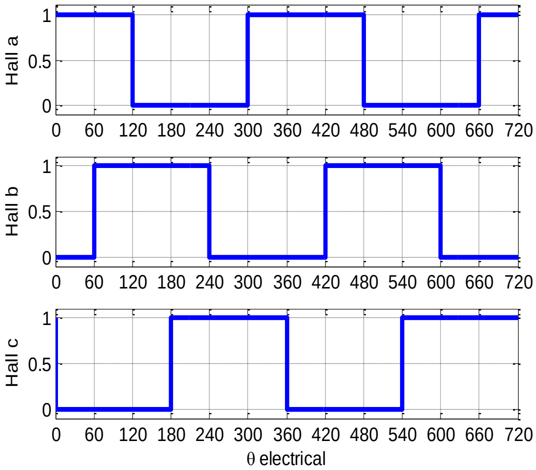

Fig. 5 Hall effect sensor output in 720-degree electrical rotation.

4 SIMULATIONS

In this section, the proposed control system is simulated using MATLAB/Simulink software. The simulations performed are straight-line maneuvers where the reference input wheel slip on each wheel is constant. The simulations include acceleration maneuvers on different road conditions. Table 3 shows the simulation parameters for the sliding mode controller.

Table 3 The simulation parameters

ϕ	K
0.1	20

In the first simulation, the vehicle is accelerating on a dry road with reference wheel slip, $\lambda_d = 0.1$, which is the desired value for maximum acceleration. Simulation results for the first maneuver are shown in "Figs. 6 to 9". Figure 6 shows the actual and desired wheel slip, while "Fig. 7" illustrates the wheel slip tracking error. The desired torque calculated by the sliding mode controller and the torque generated by BLDC motor via the current controller are shown in "Fig. 8". It is evident from "Fig. 6" that the actual slip follows the desired value precisely. However, as depicted in "Fig. 7", the tracking error is quite "noisy" which is expected when using PWM inverters. The noise introduced by the PWM inverter is also noticeable in the electromagnetic torque waveform. Additionally, "Fig. 9" demonstrates the stepped square shape of the motor currents, a result of the DC bus applying a constant voltage to the motor inductances during 120 electrical degrees.

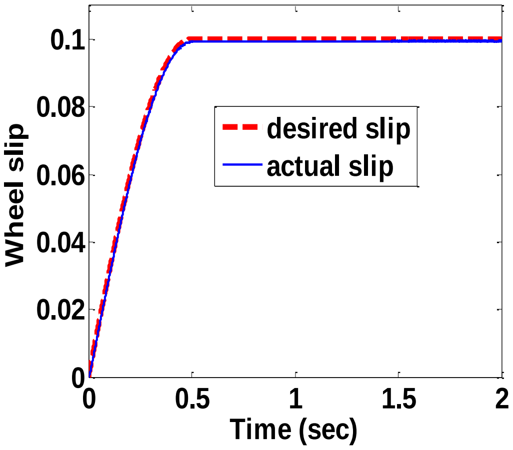

Fig. 6 Actual and desired wheel slip for accelerating on dry road.

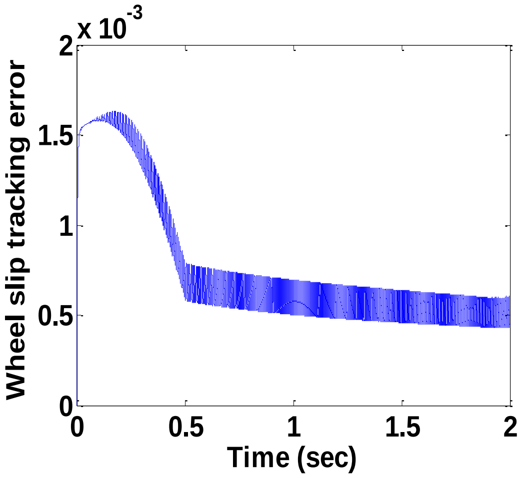

Fig. 7 Wheel slip tracking error for accelerating on dry road.

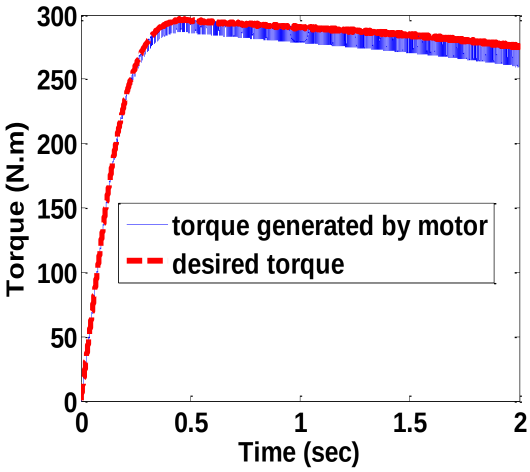

Fig. 8 The desired torque and torque generated by motor for accelerating on dry road.

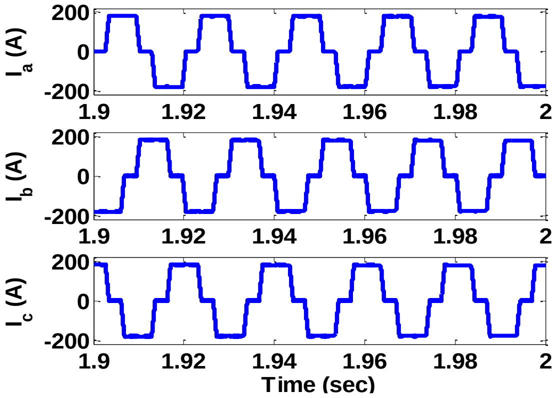

Fig. 9 Three-phase current of BLDC motor for accelerating on dry road.

In the second simulation, the vehicle is accelerating on a slippery road ($\mu = 0.4$), with reference wheel slip, $\lambda_d = 0.1$, which is the desired value for maximum acceleration on a slippery road without wheel spinning. Simulation results for the second maneuver are shown in "Figs. 10 to 13".

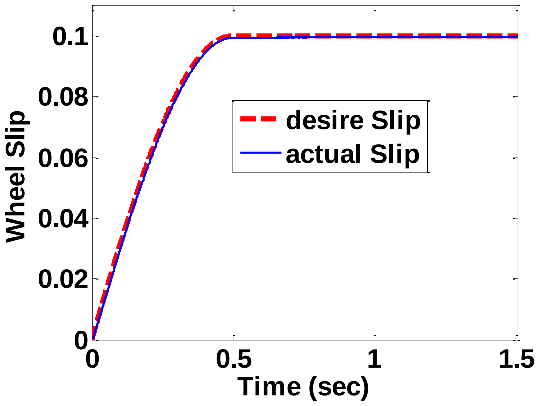

Fig. 10 Actual and desired wheel slip for accelerating on slippery road.

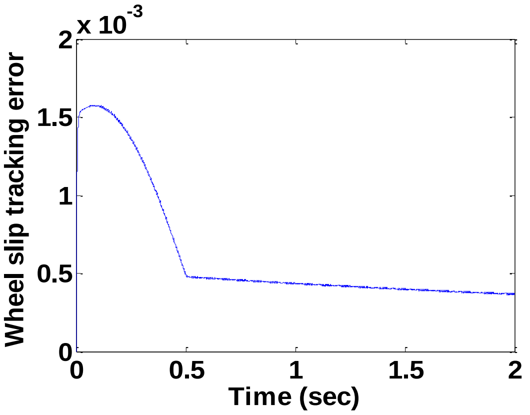

Fig. 11 Wheel slip tracking error for accelerating on slippery road.

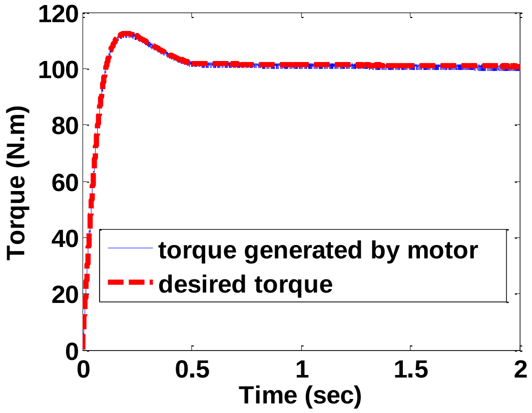

Fig. 12 The desired torque and torque generated by the motor for accelerating on a slippery road.

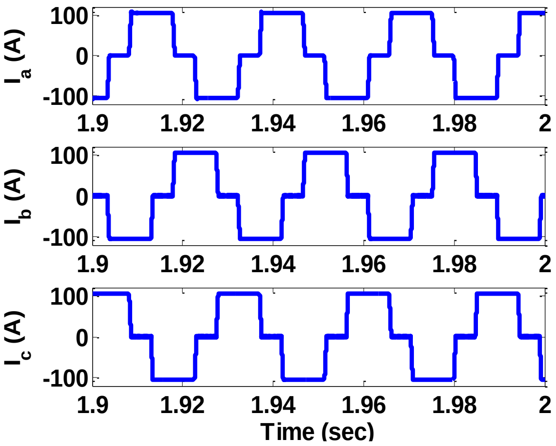

Fig. 13 Three-phase current of BLDC motor for accelerating on slippery road.

As depicted in "Figs. 10 and 11", the slip controller effectively tracks slip in slippery conditions. Additionally, "Figs. 12 and 13" demonstrate that the motor torque during the first maneuver on a dry road is higher compared to the torque on a slippery road. This is due to the reduced load torque applied to the wheel on slippery surfaces. Consequently, the phase current is also lower in comparison to the previous scenario.

5 CONCLUSIONS

In this paper, a sliding mode control strategy for controlling wheel slip with an in-wheel electric motor has been developed. This controller may be part of a vehicle dynamics stability system for in-wheel electric vehicles. The control objective is to track a reference wheel slip. To achieve this, a two-layer controller is proposed in such a way that the upper-layer controller tracks the slip reference using sliding mode and provides the desired torque for the lower-layer controller. The controller requires information on the longitudinal tire forces, which can be obtained through actual sensor signals or observers. The lower controller is the torque controller for the BLDC motor, which operates by controlling the motor's current to achieve the desired torque. The precise results of computer simulations demonstrate the good performance of the proposed control system under both normal and severe road conditions.

REFERENCES

[1] Ehsani, M., Gao, Y., and Emadi, A., Modern Electric, Hybrid Electric, and Fuel Cell Vehicles: Fundamentals, Theory, and Design, 2nd ed., CRC Press, Taylor & Francis Group, Boca Raton, Florida, USA, 2010.

[2] Chen, Y., Hedrick, J. K., and Guo, K., A Novel Direct Yaw Moment Controller for In-Wheel Motor Electric Vehicles, Vehicle System Dynamics, Vol. 51, No. 6, 2013, pp. 925-942, doi: 10.1080/00423114.2013.773453.

[3] Hu, J. S., Wang, Y., Fujimoto, H., and Hori, Y., Robust Yaw Stability Control for In-Wheel Motor Electric Vehicles, IEEE/ASME Transactions On Mechatronics, Vol. 22, No. 3, 2017, pp. 1360-1370, doi: 10.1109/TMECH.2017.2677998.

[4] Majidi, M., Asiabar, A. N., Stability Enhancement of In-Wheel Motor Drive Electric Vehicle Using Adaptive Sliding Mode Control, ADMT Journal, Vol. 15, No. 2, 2022, pp. 23-33, doi: 10.30486/admt.2022.1938721.1311.

[5] Shino, M., Nagai, M., Yaw-Moment Control of Electric Vehicle for Improving Handling and Stability, JSAE Review, Vol. 22, No. 4, 2001, pp. 473-480, doi: 10.1016/S0389-4304(01)00130-8.

[6] Shino, M., Nagai, M., Independent Wheel Torque Control of Small-Scale Electric Vehicle for Handling and Stability Improvement, JSAE Review, Vol. 24, No. 4, 2003, pp. 449-456, doi: 10.1016/S0389-4304(03)00080-8.

[7] Wang, Z., Wang, Y., Zhang, L., and Liu, M., Vehicle Stability Enhancement Through Hierarchical Control for A Four-Wheel-Independently-Actuated Electric Vehicle, Energies, Vol. 10, No. 7, 2017, pp. 947, doi: 10.3390/en10070947.

[8] Pande, S. D., and *et al.*, A Fuzzy-Based Slip Resistive Controller for Front Wheel Drive Autonomous Electric Vehicle, Electric Power Components and Systems, Vol. 52, No. 10, 2024, pp. 1821-1831.

[9] He, Z., Shi, Q., Wei, Y., Gao, B., Zhu, B., and He, L., A Model Predictive Control Approach With Slip Ratio Estimation for Electric Motor Antilock Braking of Battery Electric Vehicle, IEEE Transactions on Industrial Electronics, Vol. 69, No. 9, 2021, pp. 9225-9234.

[10] Mirzaeinejad, H., Mirzaei, M., A Novel Method for Non-Linear Control of Wheel Slip in Anti-Lock Braking Systems, Control Engineering Practice, Vol. 18, No. 8, 2010, pp. 918-926, doi: 10.1016/j.conengprac.2010.03.015.

[11] De Castro, R., Araújo, R. E., Tanelli, M., Savaresi, S. M., and Freitas, D., Torque Blending and Wheel Slip Control in Evs with In-Wheel Motors, Vehicle System Dynamics, Vol. 50, No. 1, 2012, pp. 71-94, doi: 10.1080/00423114.2012.666357.
[12] Yuan, L., Zhao, H., Chen, H., and Ren, B., Nonlinear MPC-Based Slip Control for Electric Vehicles with Vehicle Safety Constraints, Mechatronics, Vol. 38, 2016, pp. 1-15, doi: 10.1016/j.mechatronics.2016.05.006.
[13] Mashadi, B., Majidi, M., Integrated AFS/DYC Sliding Mode Controller for A Hybrid Electric Vehicle, International Journal of Vehicle Design, Vol. 56, No. 1-4, 2011, pp. 246-269, doi: 10.1504/IJVD.2011.043268.
[14] He, J., Crolla, D. A., Levesley, M., and Manning, W., Coordination of Active Steering, Driveline, and Braking for Integrated Vehicle Dynamics Control, Proceedings of the Institution of Mechanical Engineers, Part D: Journal of Automobile Engineering, Vol. 220, No. 10, 2006, pp. 1401-1420, doi: 10.1243/09544070JAUTO265.
[15] Pacejka, H., Tire and Vehicle Dynamics, Elsevier, 2005.
[16] Murugan, R., Nandakumar, S., and Mohiyadeen, M., DSP-Based Electric Power Assisted Steering Using BLDC Motor, Sadhana, Vol. 33, 2008, pp. 581-590, doi: 10.1007/s12046-008-0044-z.
[17] Slotine, J. J. E., Li, W., Applied Nonlinear Control, Prentice Hall, Englewood Cliffs, NJ, USA, 1991.

Comparison and Verification of The Results of The GTN Damage Model and The Porous Metal Plasticity Model in The Square Deep Drawing Process

Navid Givianpour[1]
Department of Mechanical Engineering,
Aligoudarz Branch, Islamic Azad University,
Aligoudarz, Iran
E-mail: Navidgivianpour@gmail.com

Hamed Deilami Azodi[2,*]
Department of Mechanical Engineering,
Arak University of Technology, Arak, Iran
E-mail: hamed.azodi@gmail.com
*Corresponding author

Shahrouz Yousefzadeh[3]
Department of Mechanical Engineering,
Aligoudarz Branch, Islamic Azad University, Aligoudarz, Iran
E-mail: sh.yousefzadeh@yahoo.com

Siamak Mazdak[4]
Engineering faculty, Tafresh University, Tafresh, Iran
E-mail: si.mazdak@tafreshu.ac.ir

Received: 19 August 2024, Revised: 15 January 2025, Accepted: 18 February 2025

Abstract: One of the main goals in the deep drawing process is to achieve a greater drawing depth without causing damage to the sheet; therefore, the drawing ratio is critical in this process. Maximizing the drawing depth has always been the goal of many studies. In this paper, the square deep drawing process is modeled in ABAQUS/Standard finite element software, and then the process is analyzed using the GTN damage model that is implemented by writing a UMAT subroutine. The process is also analyzed based on the porous metal plasticity model available in ABAQUS. The results obtained from these two analyses are compared, providing a comprehensive understanding of the different approaches in deep drawing process analysis. By examining the results, it was found that the results obtained using the GTN damage model are more consistent with the results obtained using the experimental method than the porous metal plasticity model.

Keywords: ABAQUS, Deep Drawing, Drawing Depth, GTN Damage Model, Porous Metal Plasticity

Biographical notes: Navid Givianpour received his MSc from Aligoudarz Branch, Islamic Azad University in 2008. His research interests include metal forming and machining. **Hamed Deilami Azodi** received his Ph.D. in Mechanical

Engineering from Tarbiat Modarres University, Tehran, Iran in 2008. His research interests include metal forming and advanced mechanical systems. **Shahrouz Yousefzadeh** received his Ph.D. in Mechanical Engineering from the Science and Research Branch of Islamic Azad University in 2011. His research interests focus on computational and applied mechanics. **Siamak Mazdak** received his Ph.D. in Mechanical Engineering from Tarbiat Modares University in 2013. His research interests include the finite element method, metal forming, and numerical analysis.

1 INTRODUCTION

The deep drawing process is widely used among metal forming processes because it can create different geometries. In this process, the sheet is formed in the space between the punch and the die by applying force. Regarding the sheet's fracture, the drawing depth in this process is crucial because the strain is usually a tensile strain [1-2].

In general, the deep drawing process involves parameters such as the blank holder force, clearance between punch and die, surface conditions of sheet and tools, geometry of die, and corner radius of punch and die that affect the maximum drawing depth. The effect of each parameter can be investigated using experimental tests or numerical analyses.

Usually, defects such as wrinkling, earing, and rupture may occur in this process, which can be fixed to a large extent by modifying the parameters affecting the process [3]. The deep drawing process is widely used in forming parts in the automotive industry. Since one of the goals in the automotive industry is to reduce weight along with the necessary strength of the car body, alloys with this feature are usually considered. However, these sheets may be prone to failure due to their anisotropic properties. It is necessary to evaluate their behavior with damage models to predict the sheet behavior [4]. In the metal forming processes, various factors affect the successful forming of the sheet, one of the most important of which is the sheet's formability. Usually, in deep drawing, the main goal is to increase the drawing depth, so to optimize this parameter, it can be simulated and numerically analyzed with existing damage models. Chen and Lin [5] studied the square deep drawing process and its effective parameters experimentally and numerically. In a study by Padmanabhan et al. [6], the effect of friction coefficient, blank holder force, and punch radius in the deep drawing process was investigated.

The Gurson damage model [7], a significant development in the field, is one of the various damage models used for the numerical analysis of sheet behavior in metal forming processes. According to Gurson's point of view, the evolution of the voids leads to a decrease in the load-bearing capacity (force) and, finally, the ductile failure of the material. In this model, the nucleation of the new voids during the application of strain is not considered. In other words, only the growth of pre-existing voids is considered.

Tvergaard and Needleman [8-10] proposed a model based on the Gurson model, in which the nucleation of new voids is also considered, and they named this new model Gurson-Tvergaard-Needleman (GTN). In both Gurson and GTN damage models, it is assumed that the matrix metal is isotropic and obeys the von Mises yield function. The GTN damage model, validated by experimental results, has been used to investigate damage in various processes [11-13]. Khademi et al. [14] analyzed the stretch-bending process using the GTN damage model, and their analysis results agreed with experimental tests with reasonable accuracy. Using the GTN model, Sun et al. [15] accurately predicted the experimental forming limit diagrams (FLDs) of the AZ31 sheet, which were in good agreement with reality. In their research, Kami et al. [4] applied the anisotropic GTN model to the square deep drawing process of AA6016. Banabic and Kami [16] also implemented the anisotropic GTN model to investigate the role of voids in the matrix material of sheet metal.

In damage mechanics models based on finite element solutions, when the material enters the softening zone, changing the mesh size affects the accuracy of the analysis results. This problem is more apparent in porous materials because increasing porosity leads to softening [17]. Santos et al. [18] analyzed the behavior of advanced high-strength steels (AHSS) based on the GTN model using uniaxial tensile data and initial microvoids.

Porous metal plasticity is based on Gurson's porous metal plasticity theory. In the original formulation of the Gurson model, only the growth of pre-existing voids is considered. In other words, this model does not consider the creation of voids while inducing strain on the material. While the GTN damage model considers the creation of voids, the results obtained from this method are more accurate and closer to reality.

In this paper, the drawing depth of the St12 sheet in the square deep drawing process is obtained using numerical analysis with the GTN damage model and the porous metal plasticity model. The results obtained from the two models are examined and compared. Abaqus software was used to analyze the process numerically. GTN damage model has been implemented into the Abaqus software by writing a UMAT subroutine. Another numerical analysis was done using the porous metal plasticity model available in Abaqus software, and the results of these two analyses were compared.

2 DAMAGE MODELS

2.1. GTN Damage Model

Many of the damages in structures, metal, and non-metal parts, etc., are due to defects such as poor design, defects in the structure of engineering materials, and insufficient attention to phenomena such as fatigue, corrosion, etc. Extensive research has been done to identify the causes of these problems and prevent their occurrence, which is the starting point of failure mechanics. This research examines how the cracks are created and grown. The analysis of damage caused to materials is done with several models. One of the models presented based on the combination of plasticity and damage, is the Gurson model [7], which describes the behavior of porous materials. Then, the Gurson model was modified by Tvergaard and Needleman and presented as the Gurson-Tvergaard-Needleman (GTN) model. This model is considered to describe the behavior of ductile porous materials in ductile failure. According to the GTN model, the ductile failure of the material is divided into three stages [19]. The first stage is the nucleation of the voids, the second stage is the growth of the voids, and the third stage is the coalescence of micro-cracks, while the Gurson model considers only the first stage (nucleation of voids).

According to the GTN damage model, ductile failure occurs in the following three stages:

1. The nucleation of voids is due to the separation of particle breakage, the contact surface between the matrix material and particles, or micro-cracks of the matrix material.
2. The growth of voids leads to the growth of the existing voids.
3. The coalescence of micro-cracks is caused by voids when the void volume fraction (VVF) reaches the final value, which leads to a decrease in the load-bearing capacity of the material.

Because the Gurson model, unlike the triaxial stress state, for low-stress triaxialities greatly exaggerated the failure strains, Tvergaard et al. [20] rewrote the model as follows by adding three parameters q_1, q_2, and q_3 to the Gurson model:

$$\emptyset = \frac{\sigma_{eq}^2}{\sigma_y} + 2q_1 f \cosh\left[\frac{3}{2} q_2 \frac{\sigma_m}{\sigma_y}\right] - (1 + q_3 f^2) = 0 \tag{1}$$

Where $\emptyset$, σ_{eq}, σ_y, σ_m and f are yielding potential, Von-Mises equivalent stress, matrix yield strength, hydrostatic stress, and porosity, respectively.

To take into account the fast softening of the material during the coalescence of voids, Tvergaard and Needleman [20-22] added the function $f^*(f)$ to the model (1), and the new yield function is called Gurson-Tvergaard-Needleman (GTN) as follows:

$$\emptyset = \frac{\sigma_{eq}^2}{\bar{\sigma}^2} + 2q_1 f^* \cosh\left[\frac{3}{2} q_2 \frac{\sigma_m}{\bar{\sigma}}\right] - \left(1 + q_1^2 f^{*2}\right) = 0 \tag{2}$$

$\bar{\sigma}$ is the equivalent tensile flow stress, indicating the matrix material's microscopic stress-state [20]. f^* is the modified porosity, which is calculated as follows:

$$f^*(f) = \begin{cases} f & if \;\; f < f_c \\ f_c + \delta(f - f_c) & if \;\; f_c < f < f_F \\ f_U^* & if \;\; f > f_F \end{cases} \tag{3}$$

Where δ represents the acceleration of coalescence and is equal to:

$$\delta = \frac{f_U^* - f_C}{f_F - f_C} \tag{4}$$

Where f_U^* is ultimo value (is reached when the macroscopic fracture occurs) and is obtained as $f_U^* = \frac{1}{q_1}$ when $q_3 = q_1^2$. f_c is the critical porosity corresponding to the beginning of the coalescence, and f_F is the porosity corresponding to the final fracture of the material.

The porosity evolution is due to void growth and void nucleation, so:

$$\dot{f} = \dot{f}_{growth} + \dot{f}_{nucleation} \tag{5}$$

Assuming matrix incompressibility:

$$\dot{f}_{growth} = (1 - f)\dot{\varepsilon}_{kk}^P \tag{6}$$

Where $\dot{\varepsilon}_{kk}^P$ is the trace of the macroscopic strain rates tensor.

$\dot{f}_{nucleation}$ is the contribution of the nucleation for the cases in which the plastic strain controls the nucleation:

$$\dot{f}_{nucleation} = A\dot{\bar{\varepsilon}}^P \tag{7}$$

Where $\bar{\varepsilon}^P$ is the equivalent plastic strain.

Chu and Needleman [23] proposed the normal distribution of void nucleation as follows:

$$A = \frac{f_N}{S_N\sqrt{2\pi}} exp\left[-\frac{1}{2}\left(\frac{\bar{\varepsilon}^P - \varepsilon_N}{S_N}\right)^2\right] \tag{8}$$

Where ε_N is the mean strain and S_N is the standard deviation.

GTN damage model has nine parameters that can be classified into three categories [19]:

Constitutive parameters: q_1, q_2, and q_3. These parameters are commonly fixed.

Nucleation parameters: ε_N, S_N, and f_N. The values of ε_N and S_N are usually considered to be 0.3 and 0.1 for most materials, respectively. f_N is the volume fraction of particles available for void nucleation. In contrast, the initial void volume fraction (VVF) parameter f_0 concerns all the inclusions [24-25].

Porosity parameters: f_0, f_c, and f_F. These three parameters are considered as material parameters. The initial VVF parameter f_0 indicates the initial state of the material obtained by microscopic analysis of the undamaged material. The critical void volume fraction f_c is the volume fraction of voids that when the porosity of the specimen reaches this value, the rigidity of the specimen drops suddenly. There are several methods to determine f_c, but it is complicated. Sun et al. [26-28] stated that f_c can be obtained by fitting the numerical curve with the experimental one. The final void volume fraction f_F indicates the state of the material at the fracture phase. This parameter has a constant value, its value for each material can be obtained experimentally [29] and is considered an unimportant parameter [30].

2.2. The Porous Metal Plasticity Model

The porous metal plasticity model models materials behavior with a dilute concentration of voids with a relative density greater than 0.9. This model is based on Gurson's porous metal plasticity theory (Gurson, 1977) with void nucleation and, in BAQUS/Explicit, a failure definition defines the inelastic flow of the porous metal based on a potential function that characterizes the porosity in terms of a single state variable, the relative density.

3 NUMERICAL SIMULATION OF DEEP DRAWING PROCESS

ABAQUS/CAE standard/FEM commercial software was used to determine the maximum drawing depth in the square deep drawing process of the St12 steel sheet. The geometrical model for numerical simulation of the process is shown in “Fig. 1”. The punch, die, and blank holder were modeled as rigid parts, while the metal sheet was modeled as deformable bodies with 4-node shell elements (S4R). The die was constrained in all degrees of freedom. The punch and the blank holder were fixed about all rotations and restricted to only moving downwards in the vertical direction along the y-axis. A friction coefficient of 0.1 was considered between all faces of the die and the sheet.

The fracture limits were determined based on the GTN damage model (by writing the UMAT subroutine) and the porous metal plasticity model.

Mechanical properties of St12 blanks obtained by standard uniaxial tensile test (ASTM E8/E8M) are given in “Table 1”.

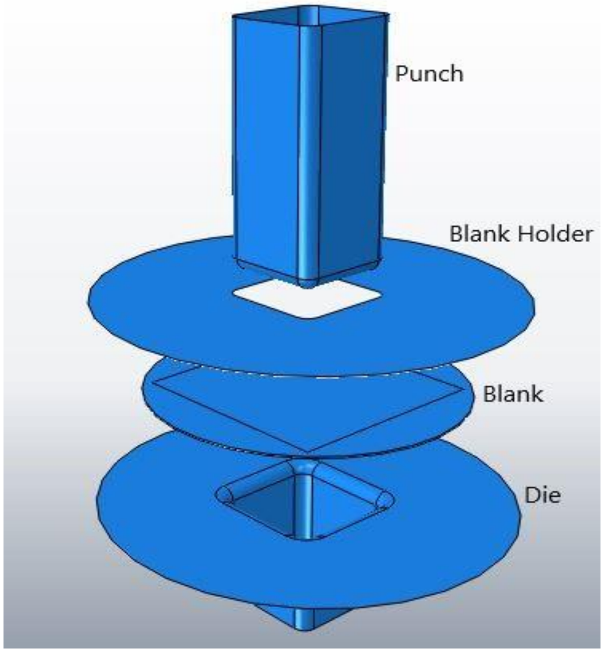

Fig. 1 Geometrical model of the deep drawing process in Abaqus software.

Table 1 Mechanical properties of St12

Variables (Unit)	Values
Thickness, *t (mm)*	0.7
Young's modulus, *E (GPa)*	210
Poisson's ratio, *v*	0.3
Density ($^{Kg}/_{m^3}$)	7850
Strength coefficient, *K (MPa)*	510
Strain hardening exponent, *n*	0.21
Strain rate sensitivity exponent, *m*	0.006

3.1. Determining the Maximum Drawing Depth Using Gtn Damage Model

As mentioned, the GTN damage model (implemented to ABAQUS by writing UMAT subroutine) and the porous metal plasticity damage model (available in the ABAQUS software) have been used to determine the maximum drawing depth in the deep drawing process. The parameters of the GTN damage model should be determined correctly, usually by comparing experimental data and numerical results [19]. Since the determination of these parameters requires a lot of experimental data [19], [31-33] and may not lead to unique results [34-35], the values suggested by

Tvergaard/Needleman are usually used for q_1, q_2, and q_3. Values of these parameters are listed in “Table 2” [4].

Table 2 Values of GTN model parameters suggested by Needleman/Tvergaard [4]

Parameter	q_1	q_2	q_3 (q_1^2)	ε_N	S_N
Value	1.5	1	2.25	0.6	0.175

In the GTN model, the nucleation void volume fraction (f_N) and Critical void volume fraction (f_C) parameters play decisive roles in the ductile fracture of the material. In this paper, the values of parameters f_0, f_N and f_F for carbon steel St12 sheet are taken from other research [36]. The value of the parameter f_C is considered to be 0.1 [37] (“Table 3”).

Table 3 Values of GTN model parameters for St12 [36-37]

Parameter	f_0	f_N	f_F	f_C
Value	0.00005	0.1	0.01	0.005

3.2. Determining the Maximum Drawing Depth Using Porous Metal Plasticity Damage Model

To determine the maximum drawing depth based on the porous metal plasticity model, values of the model parameters are considered as given in “Table 4”.

Table 4 Values of porous metal plasticity damage model parameters for St12

Parameter	q_1	q_2	q_3	f_F
Value	1.5	1	2.25	0.01
Parameter	f_C	ε_N	S_N	f_0
Value	0.005	0.6	0.175	0.00005

4 EXPERIMENTAL PROCEDURES

In experimental work, a deep drawing die assembly for square cross-section cups consisting of die, punch, blank holder, spacer, and punch guide, as shown in “Fig. 2”, was designed and made.

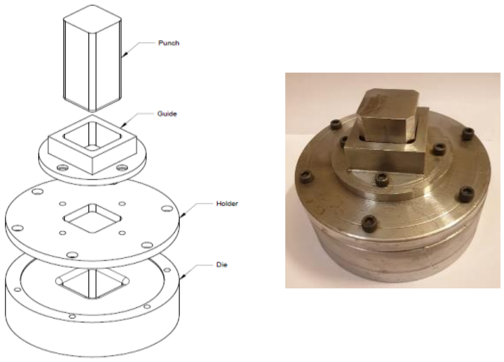

a **b**

Fig. 2 Designed die: (a): Parts of the die and, (b): Die assembly.

Experimental tests were performed using the SANTAM universal testing machine, STM 150 model (150 KN capacity). The experimental setup is shown in “Fig. 3”.

Fig. 3 Experimental setup.

The 120 mm diameter circular blanks made of a 0.7 mm-thickness sheet of carbon steel St12 were used for experimental tests. The chemical composition of this material is given in “Table 5”.

Table 5 Chemical composition of St12

Material	Mn	C	Al	Ni	Cu
St12	0.21	0.049	0.029	0.024	0.017
Material	Cr	P	S	N	Si
St12	0.016	0.008	0.008	0.003	0.002
Material	Ti	B	Fe		
St12	0.001	2×10^{-4}	Bal.		

Mechanical properties of St12 blanks are obtained by standard uniaxial tensile test (ASTM E8/E8M).

5 RESULTS AND DISCUSSION

Figure 4 shows the drawn blank at the moment of fracture in experimental tests, the numerical simulation done by ABAQUS software using the GTN model, and the Porous metal plasticity model.

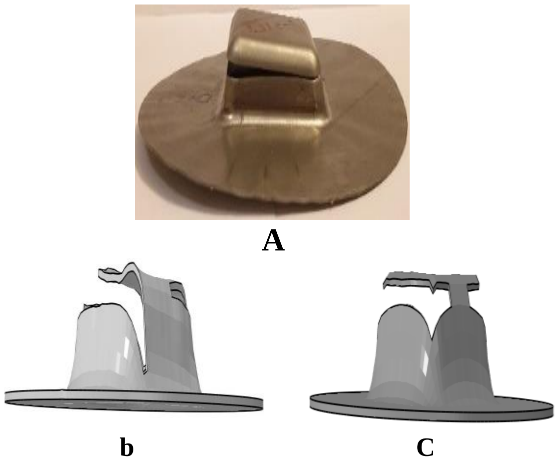

Fig. 4 Comparison of the blank at the moment of failure: (a): Experimental test, (b): Based on GTN damage model, and (c): Based on Porous metal plasticity model

The strain distribution in the sheet at the moment of sheet fracture was investigated to compare the two models. For this purpose, a path on the sheet was defined from the center of the sheet to near the outer edge of the sheet at the moment of fracture, then the strain distribution in the sheet on this path was determined based on both GTN and porous metal plasticity models. The defined path is shown in “Fig. 5”.

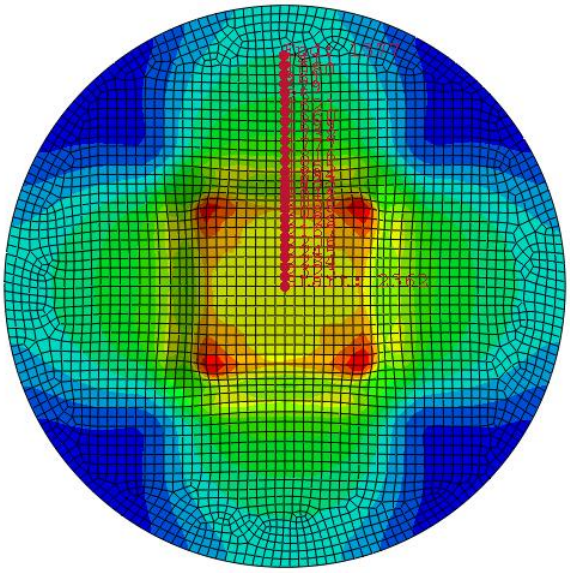

Fig. 5 The path defined to investigate the strain distribution at the moment of fracture.

Figure 6 shows the strain distribution of the specified path at the moment of sheet fracture for GTN and porous metal plasticity models. As it is evident in this figure, the stress value obtained based on the GTN damage model on this path is lower than the results of the porous metal plasticity model, which is closer to reality because, unlike the porous metal plasticity model, the GTN damage model considers the coalescence of micro-cracks.

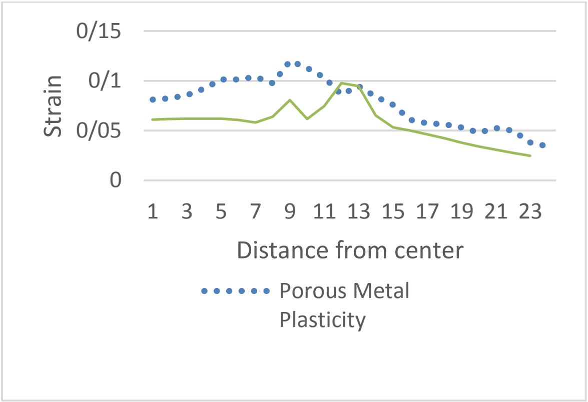

Fig. 6 Comparison of the strain distribution in the sheet at the moment of fracture based on the GTN and Porous Metal Plasticity models on the considered path.

In another comparison, the strain distribution at the moment of sheet fracture was investigated. For this purpose, an element on the drawn sheet wall was selected at the moment of fracture. Then, the strain distribution in the sheet on this element was determined based on GTN and porous metal plasticity models. The selected element is shown in “Fig. 7”. The reason for choosing this element is that it is located on the wall of the cup, which is under tension, and strain changes in this area occur relatively quickly.

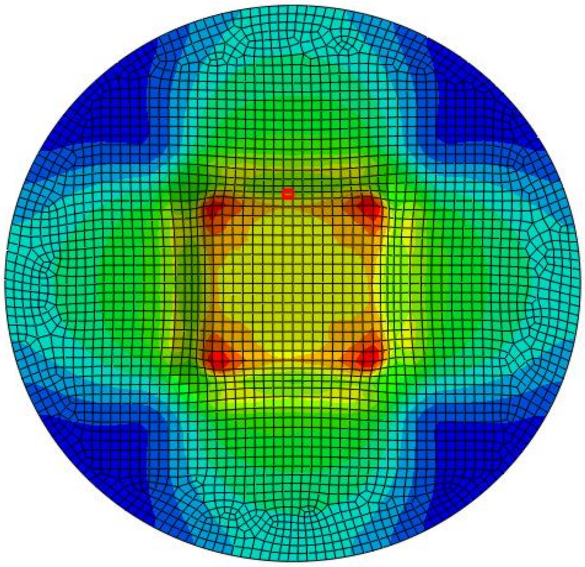

Fig. 7 The element considered to check the strain changes at the moment of sheet fracture.

In “Fig. 8”, the strain changes in the desired element at the moment of the sheet fracture are compared based on two damage models. Examining the strain changes in this element makes it possible to obtain the moment when the strain suddenly increases, which is when the fracture occurs.

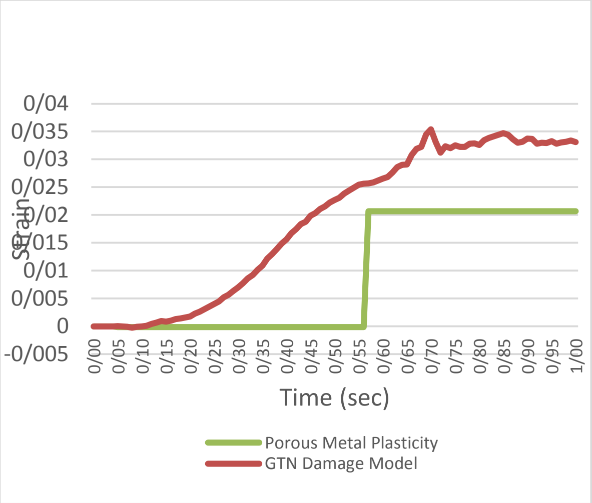

Fig. 8 Strain distribution on the considered element based on the GTN model and Porous Metal Plasticity.

Table 6 compares the fracture depth in numerical simulations based on the GTN damage model and porous metal plasticity model with the experimental one. As evident in this table, the results obtained from the GTN damage model are closer to the experimental results than the results of the Porous metal plasticity model, because, in the Porous model, the coalescence of micro-cracks is not considered.

Table 6 Depth of sheet fracture based on GTN damage model, Porous metal plasticity, and experimental test

Depth of fracture		
GTN (mm)	Porous metal plasticity (mm)	Experimental test (mm)
8.7	8.55	8.8

Figure 9 shows the effect of the friction coefficient between sheet metal, punch, and die on the maximum drawing depth for GTN and the porous metal plasticity models. As expected, by increasing the friction coefficient between the sheet and the punch and the matrix, the sheet fracture should happen earlier (the drawing depth decreases), which, as is evident in this figure, the GTN model has a better match than the porous metal plasticity model in this regard. The reason for this is that the results of the GTN damage model are more accurate due to the consideration of the coalescence of micro-cracks, unlike the porous metal plasticity model.

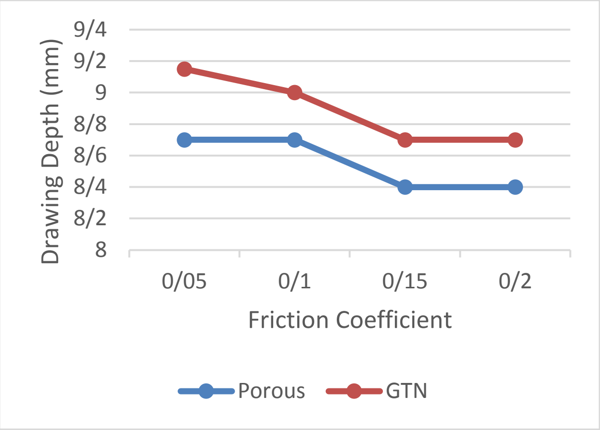

Fig. 9 Comparing the drawing depth obtained from the analysis based on the GTN model and the porous metal plasticity model in different friction coefficients.

The effect of the punch velocity on the maximum drawing depth in numerical simulations based on GTN and porous metal plasticity models is represented in “Fig. 10”. As it is evident in this figure, by increasing the speed of the punch, or in other words, by increasing the drawing speed, the sheet fracture happens sooner (the drawing depth decreases).

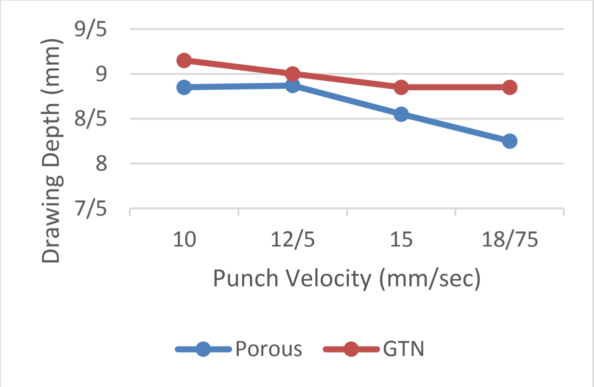

Fig. 10 Comparison of the drawing depth obtained from the analysis based on the GTN damage model and the porous metal plasticity model at different punch velocities.

Li et al.'s research was reviewed to verify the analyses' results. They analyzed the incremental sheet forming process based on the GTN damage model and the Hill 48 yield criterion by writing VUMAT in ABAQUS software. They compared the analyses' results with the results of experimental tests and observed that the GTN model's results were in good agreement with the test results [38].

6 CONCLUSIONS

In this paper, the deep drawing process was modeled in ABAQUS/Standard finite element software, and the process analysis was done based on the GTN damage model and porous metal plasticity model. Next, to verify the numerical results obtained from the analysis, these results were compared with those obtained from the experimental tests, and the following results were obtained from this comparison:

- Both model results are in good agreement with the results of the tests.
- By comparing the drawing depth obtained from the GTN damage model and porous metal plasticity model to the result of experimental tests, it is found that the GTN damage model results are more consistent with the experimental tests.
- By examining how the drawing depth changes by changing the friction coefficient between the sheet and the die, it is concluded that the GTN damage model better analyzes the behavior of the sheet during forming.
- The changes in the drawing depth in the deep drawing process were investigated by changing the speed of the punch movement, and again, the results of the GTN model are more consistent with reality than the porous metal plasticity model.

In short, it can be said that the GTN damage model has more capabilities than the porous metal plasticity model for the analysis of sheet behavior because, firstly, the porous metal plasticity model does not take into account the f_N parameter that is present in the GTN model. Secondly, in the subroutine written for the GTN model, the mechanical properties of the sheet can be defined more precisely and comprehensively, which results in better results from the analysis based on the GTN model.

REFERENCES

[1] Hosford, W. F., Caddell, R. M., Metal Forming: Mechanics and Metallurgy, Cambridge University Press, 2011.

[2] Lange, K., Handbook of Metal Forming, McGraw-Hill Book Company, 1985, pp. 1216.

[3] Johnson, W., Mellor, P. B., Engineering Plasticity, John Willey & Sons: New York, 1983.

[4] Kami, A., Dariani, B. M., Vanini, A. S., Comsa, D. S., and Banabic, D., Application of a GTN Damage Model to Predict the Fracture of Metallic Sheets Subjected to Deep-Drawing, Proceedings of the Romanian Academy, Series A, Vol. 15, 2014, pp. 300–309.

[5] Chen, F. K., Lin, S. Y., A Formability Index for The Deep Drawing of Stainless-Steel Rectangular Cups, The International Journal of Advanced Manufacturing Technology, Vol. 34, No. 9, 2007, pp. 878-888.

[6] Padmanabhan, R., Oliveira, M. C., Alves, J. L., and Menezes, L. F., Influence of Process Parameters on the Deep Drawing of Stainless Steel, Finite Elements in Analysis and Design, Vol. 43, No. 14, 2007, pp. 1062-1067.

[7] Gurson, A. L., Continuum Theory of Ductile Rupture by Void Nucleation and Growth: Part I—Yield Criteria and Flow Rules for Porous Ductile Media, Journal of Engineering Materials and Technology, Vol. 99, No. 1, 1977, pp. 2–15.

[8] Tvergaard, V., Influence of Voids on Shear Band Instabilities Under Plane Strain Conditions, International Journal of fracture, Vol. 17, No. 4, 1981, pp. 389-407.

[9] Tvergaard, V., On Localization in Ductile Materials Containing Spherical Voids, International Journal of fracture, Vol. 18, No. 4, 1982, pp. 237-252.

[10] Tvergaard, V., Needleman, A., Analysis of the Cup-Cone Fracture in A Round Tensile Bar, Acta Metallurgica, Vol. 32, No. 1, 1984, pp. 157-169.

[11] Chen, Z., Dong, X., The GTN Damage Model Based on Hill’48 Anisotropic Yield Criterion and Its Application in Sheet Metal Forming, Computational Materials Science, Vol. 44, No. 3, 2009, pp. 1013-1021.

[12] Brunet, M., Sabourin, F., and Mguil-Touchal, S., The Prediction of Necking and Failure in 3 D, Sheet Forming Analysis Using Damage Variable. Le Journal de Physique IV, Vol. 6, No. C6, 1996, pp. C6-473.

[13] Brunet, M., Mguil, S., and Morestin, F., Analytical and experimental studies of necking in sheet metal forming processes. Journal of Materials Processing Technology, 80, 1998, pp. 40-46.

[14] Khademi, M., Mirnia, M. J., and Naeini, H. M., Numerical Analysis of Ductile Fracture in Stretch Bending of AA6061-T6 Aluminum Alloy Sheet Using GTN Damage Model, International Journal of Solids and Structures, Vol. 301, 2024, pp. 112947.

[15] Sun, X., Mo, X., Liu, Y., Shen, W., Li, C., Li, Y., and Xue, F., GTN Poroplastic Damage Model Construction and Forming Limit Prediction of Magnesium Alloy Based on BP-GA Neural Network, Materials Today Communications, Vol. 41, 2024, pp. 110295.

[16] Banabic, D., and Kami, A., Applications of the Gurson’s Model in Sheet Metal Forming, In MATEC Web of Conferences, EDP Sciences, Vol. 190, 2018, pp. 01002.

[17] Aravas, N., Papadioti, I., A Non-Local Plasticity Model for Porous Metals with Deformation-Induced Anisotropy: Mathematical and Computational Issues, Journal of the Mechanics and Physics of Solids, Vol. 146, 2021, pp. 104190.

[18] Santos, R. O., Moreira, L. P., Butuc, M. C., Vincze, G., and Pereira, A. B., Damage Analysis of Third-Generation Advanced High-Strength Steel Based on the Gurson–Tvergaard–Needleman (GTN) Model, Metals, Vol. 12, No. 2, 2022, pp. 214. https://doi.org/10.3390/met12020214.

[19] Miloud, M. H., Zidane, I., and Mendas, M., Coupled Identification of The Hardening Behavior Laws and Gurson–Tvergaard–Needleman Damage Parameters-Validation on Tear Test of 12NiCr6 CT Specimen, Frattura ed Integrità Strutturale, Vol. 13, No. 49, 2019, pp. 630-642.

[20] Tvergaard, V., Needleman, A., Analysis of the Cup-Cone Fracture in A Round Tensile Bar, Acta metallurgica, Vol. 32, No. 1, 1984, pp. 157-169.

[21] Tvergaard, V., Influence of Voids on Shear Band Instabilities Under Plane Strain Conditions, International Journal of fracture, Vol. 17, No. 4, 1981, pp. 389-407.
[22] Tvergaard, V., On Localization in Ductile Materials Containing Spherical Voids, International Journal of Fracture, Vol. 18, No. 4, 1982, pp. 237-252.
[23] Chu, C., Needleman, A., Void Nucleation Effects in Biaxially Stretched Sheets, Journal of Engineering Materials and Technology, Vol. 102, 1980, pp. 249–56.
[24] Miloud, M. H., Imad, A., Benseddiq, N., Bachir Bouiadjra, B., Bounif, A., and Serier, B., A Numerical Analysis of Relationship Between Ductility and Nucleation and Critical Void Volume Fraction Parameters of Gurson–Tvergaard–Needleman Model. Proceedings of the Institution of Mechanical Engineers, Part C: Journal of Mechanical Engineering Science, Vol. 227, No. 11, 2013, pp. 2634-2646.
[25] Cox, T., Low, J. J., An Investigation of The Plastic Fracture of AISI4340 and 18Nickel-200 Grade Maraging Steels, Metall Trans A, Vol. 5, 1974, pp. 1457–1470.
[26] Sun, D. Z., Siegele, D., Voss, B., and Schmitt, W., Application of Local Damage Models to The Numerical Analysis of Ductile Rupture, Fatigue & Fracture of Engineering Materials & Structures, Vol. 12, No. 3, 1989, pp. 201-212.
[27] Sun, D. Z., Voss, B., and Schmitt, W., Numerical Prediction of Ductile Fracture Resistance Behaviour Based on Micromechanical Models, Defect Assessment in Components-Fundamentals and Applications, 1989, pp. 447-458.
[28] Sun, D. Z., Kienzler, R., Voss, B., and Schmitt, W., Application of Micromechanical Models to The Prediction of Ductile Fracture, Astm Special Technical Publication, Vol. 1131, 1992, pp. 368-378.
[29] Guillemer-Neel, C., Feaugas, X., and Clavel, M., Mechanical Behavior and Damage Kinetics in Nodular Cast Iron: Part I. Damage Mechanisms. Metallurgical and Materials Transactions A, Vol. 31, No. 12, 2000, pp. 3063-3074.
[30] Zhang, Z. L., Thaulow, C., and Ødegård, J., A Complete Gurson Model Approach for Ductile Fracture, Engineering Fracture Mechanics, Vol. 67, No. 2, 2000, pp. 155-168.
[31] Kuna, M., Springmann, M., Determination of Ductile Damage Parameters by Local Deformation Fields, In Fracture of Nano and Engineering Materials and Structures, Springer, Dordrecht, 2006, pp. 535-536.
[32] Djouabi, M., Ati, A., and Manach, P. Y., Identification Strategy Influence of Elastoplastic Behavior Law Parameters on Gurson–Tvergaard–Needleman Damage Parameters: Application to DP980 Steel, International Journal of Damage Mechanics, Vol. 28, No. 3, 2019, pp. 427-454.
[33] Hadj Miloud, M., Modélisation De La Rupture Ductile De L’acier 12 NiCr6 Par Le Modèle Micromecanique De Gurson (Doctoral dissertation, Université Mohamed Boudiaf des Sciences et de la Technologie-Mohamed Boudiaf d'Oran), 2017.
[34] Li, Z. H., Bilby, B. A., and Howard, I. C., A study of the Internal Parameters of Ductile Damage Theory, Fatigue & Fracture of Engineering Materials & Structures, Vol. 17, No. 9, 1994, pp. 1075-1087.
[35] Zhang, Z. L., A Sensitivity Analysis of Material Parameters for the Gurson Constitutive Model, Fatigue & Fracture of Engineering Materials & Structures, Vol. 19, No. 5, 1996, pp. 561-570.
[36] Guzmán, C. F., Experimental and Numerical Characterization of Damage and Application to Incremental Forming, (A Thesis submitted to the University of Liège in Partial Ful_Llment of the Requirements for The Degree of Docteur en Sciences de l'Ingénieur), 2015.
[37] Parsa, M. H., Ettehad, M., and Matin, P. H., Forming Limit Diagram Determination of Al 3105 Sheets and Al 3105/Polypropylene/Al 3105 Sandwich Sheets Using Numerical Calculations and Experimental Investigations. Journal of Engineering Materials and Technology, Vol. 135, No. 3, 2013.
[38] Li, J., Li, S., Xie, Z., & Wang, W., Numerical Simulation of Incremental Sheet Forming Based on GTN Damage Model, The International Journal of Advanced Manufacturing Technology, Vol. 81, 2015, pp. 2053-2065.

Experimental Analysis and Statistical Prediction of Tissue Temperature in High-Speed Cortical Bone Drilling Process

Mehdi Safari[1], Vahid Tahmasbi[2], Jalal Joudaki[3, *]
Department of Mechanical Engineering,
Arak University of Technology, Iran
E-mail: m.safari@arakut.ac.ir , tahmasbi@arakut.ac.ir, joudaki@arakut.ac.ir
*Corresponding author

Mojtaba Zolfaghari[4]

Faculty of Engineering,
Arak University, Iran
E-mail: m-zolfaghari@araku.ac.ir

Received: 12 December 2024, Revised: 20 February 2025, Accepted: 12 March 2025

Abstract: The drilling process in surgery is used for joining the pins and prostheses to the human body. Proper drilling can improve the strength of the joint. In this article, the drilling of cortical bone is experimentally investigated at high-speed ranges. For this purpose, the effects of input process variables, including the rotational speed, feed rate, and drill diameter, on the maximum temperature of bone tissue are studied. The response surface methodology (RSM) method is employed for designing the experiments (15 experiments). The results show that the temperature of the tissue first decreases until it reaches a minimum value by increasing the rotational speed, and then the temperature of the tissue begins to increase with the further increase of the rotational speed. Also, the maximum value of tissue temperature was reduced by increasing the feed rate of the tool in the drilling process. In addition, with an increase in the drill diameter, the maximum temperature of the tissue is reduced. The temperature of the bone tissue is predicted using a regression equation as a function of process variables.

Keywords: Feed Rate, High-Speed Bone Drilling Process, Response Surface Methodology, Rotational Speed, Tissue Temperature

Biographical notes: Mehdi Safari received his Ph.D. in Mechanical Engineering from the Isfahan University of Technology (IUT) in 2014. He is currently an Associate Professor at the Department of Mechanical Engineering, Arak University of Technology, Arak, Iran. His current research interests include experimental tests, finite element modelling, metal forming, machining, and manufacturing processes. **Vahid Tahmasbi** received his Ph.D. in Mechanical Engineering from the K.N. Toosi University of Technology (KNTU) in 2018. He is currently an Associate Professor at the Department of Mechanical Engineering, Arak University of Technology, Arak, Iran. His research interests include experimental tests, machining, advanced manufacturing processes, and biomechanics. **Jalal Joudaki** received his Ph.D. in Mechanical Engineering from the Iran University of Science and Technology (IUST) in 2016. He is currently an Associate Professor at the Department of Mechanical Engineering, Arak University of Technology, Arak, Iran. His research interests include experimental tests, finite element modelling, metal forming, and manufacturing processes. **Mojtaba Zolfaghari** received his Ph.D. in Mechanical Engineering from the Bu-Ali Sina University (BASU) in 2014. He is currently an Associate Professor at the Faculty of Engineering of Arak University, Arak, Iran. His research interests include experimental tests, finite element modelling, machining, and manufacturing processes.

1 INTRODUCTION

The drilling of human bone is one of the most important objects of health science that is extensively used in orthopedic surgery, dentistry, fracture treatment, and bone sampling. Today, in bone drilling, the goal is to achieve the lowest amount of mechanical and thermal damage to the bone tissue. This process is one of the most important, sensitive, and widely used mechanical processes in the field of medical engineering due to the complexity and special conditions of the bone material. Bone fracture treatment is performed by restoring the original location of the organ and fixing it with implantable components. Through the operation of bone drilling, screws and implants can be placed inside the broken parts to fix the damaged parts to each other. It should be noted that the term bone, as the main member and constituent of the skeleton of the human body and other vertebrates, refers to a family of materials that have a complex and organized structure. Bone tissue is a non-homogeneous, anisotropic, and porous substance whose porosity is between 5% and 95%, depending on factors such as location, function, and performance conditions. Bone tissue is a smart tissue and changes its structure when a crack occurs, depending on the conditions. The most effective parameters process in the drilling of the bone can be divided into two groups related to process control and parameters related to the geometry and characteristics of the drill. The rotational speed, the feed rate of the tool, the cooling condition, the depth of drilling, and the pre-drilling diameter are the most important parameters related to the control of the drilling process. The drill diameter, helix angle, chisel edge angle, point angle of the drill, rake angle, and the criteria of tool life (erosion of the tool) are the most geometrical variables of the drill tool. Also, the temperature increases in the drilling process, the axial force applied to the bone tissue, the torque created in the drilling process, and the surface roughness can be mentioned as the most important output responses of the bone drilling process. The most important parameter of an automated drilling process is the rotational speed. The next effective parameter is the feed rate. Research in the field of bone piercing is continuously progressing and expanding. One of the most important parameters that must be considered and constantly checked during the drilling is the amount of heat generated due to the frictional contact in the bone tissue. The generated heat transfers according to the conductivity of the bone, and the thermal conductivity measurement shows that the thermal conductivity coefficient is as low as 0.38-2.3 W/(m.°K) [1]. So, the generated heat transfers very slowly, and most of the heat remains in the drilling location. This is undesired because this heat changes the nature of the bone. This provides the basis for the phenomenon of thermal necrosis, bone tissue death, cell death, and reducing strength in the drilling location [2]. The strength of the remaining drilled material is very important in orthopedic surgery. Reducing the strength leads to insufficient supporting of installed automatic screws in the next step, and consequently, problems to restrain the support equipment and stabilize the fracture position in this hole appear. The main problem is weak bone welding in the desired direction due to the lack of strength in the retaining screw and the bone (the drilling area). The rate of failure in plaque implantation in leg fractures has been reported up to 7.1% [3-4]. By studying rabbit bone, Lundskog [5] concluded that bone undergoes cell death when exposed to a temperature of 55°C for 30 seconds. By conducting microscopic studies on rabbit bone, Erickson et al. [6] concluded that a temperature of 47°C for 60 seconds causes thermal necrosis in cortical bone. Two factors that affect thermal necrosis are the specified temperature magnitude and exposure time to that temperature. A threshold limit of temperature to prevent thermal necrosis has been reported by some researchers; the temperature has no significant effect on bone tissue below the threshold temperature, but at higher temperatures, the bone cells are affected by the generated heat. The threshold limit of temperature was reported as 47°C for 60 seconds time duration. According to the tests carried out, the tolerable time for the bone decreases exponentially for a rise in temperature above 47°C. At 48°C, this period is reduced to 30 seconds, while at 53°C, the thermal necrosis happens immediately [7-8]. Brisman [9] reported that an independent increase in speed or axial force increases the temperature in the bone, while increasing the combination of these two parameters improves the cutting efficiency without causing a significant temperature change. Histological studies focusing on the effect of high-speed drilling in the orthopedic surgery process have been carried out by Boyne [10], Moss [11], and Spartz [12]. In these studies, it has been suggested that high-speed drilling has less harmful effects than conventional (low-speed) drilling. Abouzgia et al. [13] by experimenting on cow bone at a speed of 49000 rpm without cooling reported that by increasing force up to 4 N, the temperature increases first, and then it decreases by increasing the force above 4 N. However, increasing the axial force may cause micro-cracks around the hole and damage the bone or lead to the drill breaking inside the bone. Iyer et al. [14] conducted a study on the rabbit tibia. The generated heat during bone cutting in living tissue was measured at three levels: low speed (2000 rpm), medium speed (30000 rpm), and high speed (400000 rpm). An inverse relation between the drilling speed and the generated heat was observed.

Li et al. [15] studied the heat transfer of the drilling process on bones by developing a 3D finite element model in ANSYS software. The maximum temperature of bone has been measured according to varying the influencing process parameters (spindle speed, feed rate, and drill diameter). The results show an increase in maximum temperature by increasing any of the process inputs. The maximum temperature is predicted by developing an empirical equation, and it can be optimized to obtain the minimum temperature. Ying et al. [16] investigated the variation of temperature and force during the cutting by conventional cutting and ultrasonic vibration-assisted cutting experimentally and numerically. A finite element model is developed in ABAQUS software using the Johnson-Cook material model. The results show that the ultrasonic vibration decreases the cutting force while it increases the temperature. Also, the cutting force decreases with decreasing cutting speed, while the temperature increases. Dahibhate et al. [17] investigated the temperature variation during bone drilling of sheep rib bone. The experiments have been conducted for process parameters including the drill diameter (2.5, 3.2, 4.5 mm), feed rate (50, 60, 70 mm/min), and spindle speeds (1000, 1500, 2000 rpm). A linear regression equation was developed for the prediction of bone drilling temperature. The analysis of experimental results by statistical tools shows that the most effective parameter is the drill diameter. The second affecting parameter is feed rate.

Also, the rate and quality of postoperative healing in the jawbone were measured. The results show that the healing rate and quality of the bone formed in drilled holes at high speed are better than using the low and medium speeds in the first 6 weeks after drilling [18]. Reingewirtz et al. [19] by studying the high-speed drilling of the beef femur, concluded that the temperature increases directly in the range of 400-7000 rpm rotational speed, and it decreases by increasing the rotational speed in the range of 7000-24000 rpm. It was also concluded that changes in the feed rate from 80 to 200 mm/min have a negligible effect on the temperature in the range of low speeds, such as 400-800 rpm. Udiljak et al. [20] investigated the study of high-speed porcine bone drilling. The drilling machine was prepared with 10000 to 16000 rpm rotational speeds, and a standard surgical drill was used. It was concluded that the rate of temperature increase at high speeds has decreased compared to low speeds, and no significant effect on temperature changes at speeds above 10000 rpm was observed. Li et al. [21] investigated experimentally the effects of cutting speed and feed rate during the drilling of beef femurs. The results show that the maximum temperature increases by increasing the cutting speed and decreasing the feed rate. By studying the cow femur in two different speed ranges of 500-1000 rpm (low speed) and 3000-18000 rpm (high speed), Shakoori et al. [22] reported that the temperature decreases with increasing the rotational speed in conventional drilling. Tahmasbi et al. [23] developed a regression equation using response surface methodology to find the temperature in the bone drilling process according to the process variables (rotational speed, feed rate, and tool diameter).

As the literature survey shows, obtaining a good hole quality in the drilling of bones is important and has several advantages in surgery and patient life. In recent years, attention has been drawn to the high-speed drilling of bones. In this research, the effect of drilling process parameters on the generated heat will be investigated experimentally. The experimental tests have been planned according to response surface methodology (RSM). The effective parameters will be determined by analysis of the variance (ANOVA). The attitude of the current study is to find a reliable equation for predicting the temperature in bone drilling at high speeds.

2 MATERIALS AND METHODS

In the experiments, fresh femur bovine bone aged about 3-4 years was used [23]. A 100 mm length diaphysis part of the cow thigh (middle part) has been used in the experimentation. The cortical bone has about 8-10 mm thickness. Also, to make things easier in the experimentations, the beginning and end parts of the femur were cut with a saw. In “Fig. 1”, a fresh femur bovine bone that was used in the experiments can be seen.

Fig. 1 A fresh femur bovine bone was used in the experiments.

It should be noted that the experimentations have been carried out on the bovine cortical femur because its physical and mechanical characteristics are very similar to the human long bones [24]. Therefore, many researchers have used cow femur to investigate the cortical bone drilling process. For carrying out this research, a long time should not have passed since the bone tissue was alive, so that the thermomechanical and physical properties and density of the new bone tissue are preserved and resemble the living tissue undergoing surgery. The thermomechanical and physical properties of the bone change widely over time and will no longer have the necessary similarity with the conditions of surgery [25]. Also, if the fresh bone is not used (for about 3-4 hours) to preserve its properties, the fresh bone should be quickly placed in the freezer at -25℃. In this study, the femur of the cow, which was removed from its body immediately after slaughter, has been used. Due to the time gap between slaughtering and drilling, to keep the bones fresh after removing the excess meat that remained on its surface, the bones were immediately frozen to keep them fresh and placed in the open air for a few hours before the experiment. The thickness of the outer cortex of the bone wall, which is the cortical part of the bone, is about 8-10 mm. Before performing the experiments, the surface of the bone is completely cleaned of the remaining meat and fats on the surface of the bone, because the presence of these complications causes problems in the way of draining the chips and increases the possibility of clogging the drill grooves. To facilitate the measurement of bone temperature and the proper placement of bone on the load cell to read the drilling force, samples with a width of about 15 to 20 mm have been created using a milling machine. By doing this cutting, smooth pieces that can be drilled and tested are better selected. These tests have been done at room temperature without using any coolant liquid.

In this research, to perform high-speed experiments, a high-speed motor with a wide range of rotational speeds is used. The maximum available rotational speed of the motor is 18,000 rpm. This motor is installed on the head of the milling machine using a base so that the drilling tool can be installed on it. K-type thermocouples have been used for measuring the temperature while drilling. The thermocouple is placed at a 3 mm depth, 0.5 mm distance from the wall of the hole created in the bone tissue to measure the temperature. The position is determined based on the investigations that have been done in previous research [26]. Also, to measure the force in this research, single base load cells were used; the maximum amount of force that can be measured is up to 30 kg with an accuracy of 0.01 kg. The standard high-speed steel (HSS) drills have been selected for performing the drilling process. The diameters of the drills are 2, 4, and 6 mm, respectively. Of course, the other geometrical characteristics of the drills, such as point angle, helix angle, and other characteristics, are the same in all of the experiments. The experiments have been carried out according to the design of experiments (DOE) planning, which determines the optimal number of experiments to find the proper equation between the output variable and input variable. The response surface methodology (RSM) is one of the DOE techniques that predict the output carriable with good correlation. This method is suitable for finding the effect of the interaction of process parameters. In this research, three process parameters, including feed rate, rotational speed, and drill diameter, are selected as input variables. According to “Table 1”, the rotational speed is adjusted between 10000-18000 rpm, the feed rate is adjusted between 10-50 mm/min, and the drill diameters are set between 2-6 mm. “Table 2” displays the experiments that should be performed.

a) **Table 1** The levels of each input parameter for the high-speed bone drilling process

Input Variables	Symbol	Min Value	Mid Value	Max Value
Rotational speed (rpm)	N	10000	14000	18000
Feed rate (mm/min)	F	10	30	50
Drill diameter (mm)	D	2	4	6

Table 2 The designed experiment plan according to RSM

Experiment number	N(rpm)	F(mm/min)	D(mm)
1	10000	10	2
2	18000	10	2
3	10000	50	2
4	18000	50	2
5	10000	10	6
6	18000	10	6
7	10000	50	6
8	18000	50	6
9	10000	30	4
10	18000	30	4
11	14000	10	4
12	14000	50	4
13	14000	30	2
14	14000	30	6
15	14000	30	4

3 RESULTS AND DISCUSSION

According to the analysis of the maximum temperature values obtained from the experiments, the analysis of variance (ANOVA) results for the data of the experiments are shown in “Table 3”. The ANOVA determines the effect of the input variables and their interactions on the output variable.

Table 3 Analysis of variance of the maximum temperature

Source	DF	Adj SS	Adj MS	F-Value	P-Value
Model	8	1199.59	149.949	42.08	0.000
Linear	3	317.77	105.925	29.72	0.000
N	1	171.23	171.230	48.05	0.000
F	1	138.53	138.533	38.87	0.000
D	1	8.01	8.010	2.25	0.162
Square	2	232.36	116.178	32.60	0.000
N*N	1	48.31	48.314	13.56	0.004
F*F	1	44.66	44.656	12.53	0.005
2-Way Interaction	3	649.46	216.486	60.75	0.000
N*F	1	35.96	35.955	10.09	0.009
N*D	1	116.43	116.434	32.67	0.000
Error	11	39.20	3.564		
Lack-of-Fit	6	30.59	5.098	2.96	0.127
Pure Error	5	8.61	1.723		
Total	19	1238.79			

Considering the confidence level of 95% in the experiments, the input variables with a P-value less than 0.05 are considered effective parameters on the tissue temperature in the high-speed bone drilling process. The results of Table 3 show that the rotational speed, feed rate, and the diameter of the drill are the effective parameters of the output variable (tissue temperature).

Equation 1 expresses the tissue temperature in high-speed bone drilling, which, of course, is appropriate for the range considered for the input parameters in “Table 2”.

$$\begin{aligned} T \;=\; & 97.7 - 0.00513N - 1.164F \\ & + 0.32D + 0.000000N^2 + 0.00934F^2 \\ & - 0.000027N \times F - 0.000477N \times D \\ & + 0.1971F \times D \end{aligned} \tag{1}$$

The coefficient of determination “R^2” is used to show the quality of curve fitting. It is the amount of agreement between predicted data by the regression (statistical) model and experimental data. The value of R^2 is 1 for a theoretically perfect statistical model. The coefficient of determination (R^2) was 0.9453 for the response of tissue temperature, which means that the proposed equation can predict 94.53% of the experimental data. Considering the value of R-sq=94.53% and also the appropriate dispersion of residual analysis according to “Fig. 2”, it can be said that the modelling done has acceptable accuracy.

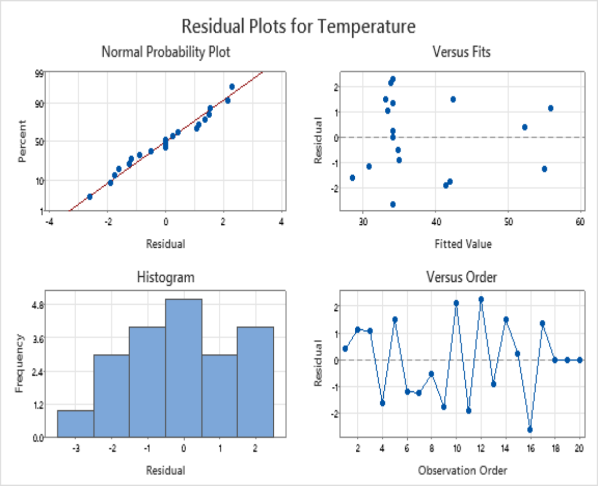

Fig. 2 The residual plots for the model in the high-speed bone drilling process.

To describe the effect of variation in input parameters on the output variable (tissue temperature), the diagram of the mean effect plot and the interaction plot were utilized. In “Fig. 3”, the effect of rotational speed on the maximum value of tissue temperature is presented. It is obvious that by increasing the rotational speed, the tissue temperature first decreased until it reached a minimum value, and then the temperature of the tissue began to increase.

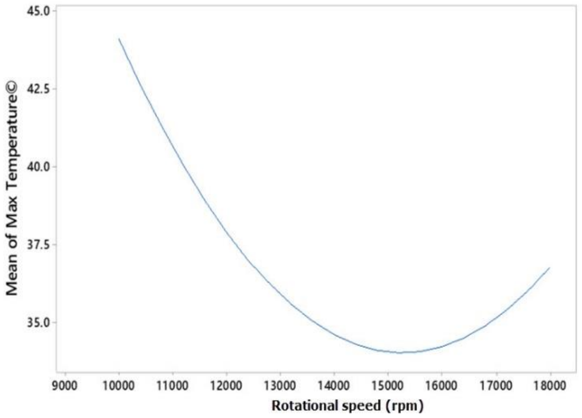

Fig. 3 The effect of rotational speed on the maximum value of tissue temperature in the high-speed bone drilling process.

In this research, the choice of high-speed drilling was in the range of 10,000 to 18,000 rpm. It should be noted that in the high-speed bone drilling process, the size of the deformed chips in the form of powder becomes smaller by increasing the rotational speed, which leads to the ease and better removal of the chips from the drilled hole which is the reason for the decreasing slope of the temperature graph from the speed of 10,000 to the range of 15,000 rpm. But after passing the range of 15,000 rpm, despite the constant force, the temperature shows an increasing trend. Considering the three sources of heat generation in the drilling process, i.e. chip formation force, chip accumulation in the flute, and the frictional contact between the chip, drill, and bone, it can be assumed that with increasing the rotational speed of the drill, the generated heat due to the friction between the chip or the drill body and the hole wall will increase and this heat generation factor, from a certain rotational speed onward overcomes the positive effect of force loss and reduction of chip accumulation and leads to a further increase in temperature.

In “Fig. 4”, the effect of feed rate on the maximum value of tissue temperature is shown. As can be seen, the maximum value of tissue temperature reduces with an increase in the feed rate of the drill. The reason is that with an increase in the drill feed rate, the drilling time decreases, and consequently, the generated heat due to the friction is reduced, and as a result, the temperature also decreases. In addition, in “Fig. 5”, the effect of drill diameter on the maximum value of tissue temperature is shown.

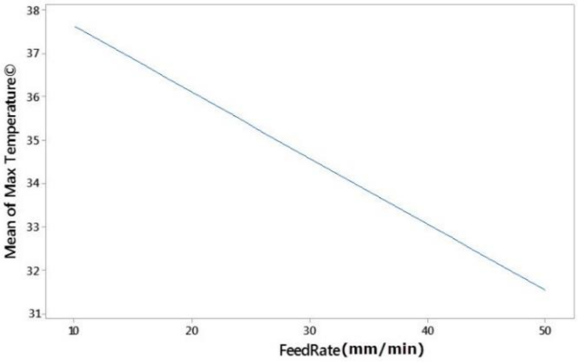

Fig. 4 The effect of feed rate on the maximum value of tissue temperature in the high-speed bone drilling process.

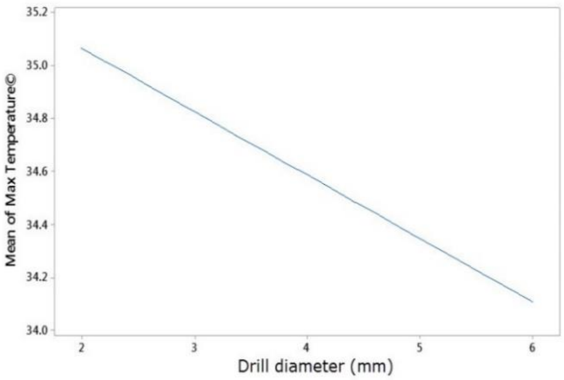

Fig. 5 The effect of drill diameter on the maximum value of tissue temperature in the high-speed bone drilling process.

As it is concluded from “Fig. 5”, with an increase in the drill diameter, the maximum value of tissue temperature is reduced. The reason is that by increasing the drill diameter, the exit channel of the chips in the drill will be bigger, which leads to a decrease in tissue temperature. Figure 6 shows the interactions of process parameters on the tissue temperature in a high-speed bone drilling process, which again confirms the effects of input variables on the maximum value of tissue temperature. The results show that the minimum temperature occurs at a high feed rate and high rotational speed, while at a low feed rate, the temperature is generally higher and it is undesired. Also, the temperature decreases by increasing the tool diameter and increasing the rotational speed. From “Fig. 4 and Fig. 5”, it is obvious that the interaction of tool diameter and feed rate is descending.

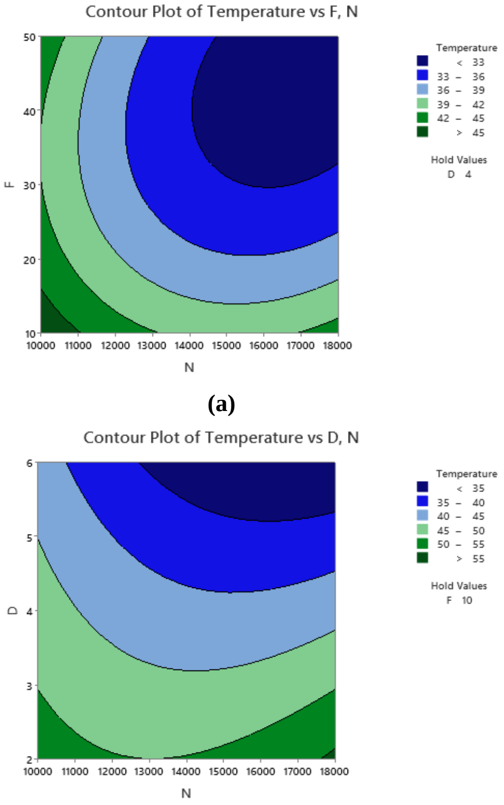

(a)

(b)

Fig. 6 The interactions of: (a): rotational speed, feed rate, and (b): drill diameter on the tissue temperature in the high-speed bone drilling process.

4 CONCLUSIONS

In this work, the drilling process of cortical bone at high-speed ranges was investigated experimentally, and by using statistical tools (ANOVA), the effects of input process parameters including the rotational speed, feed rate, and drill diameter on the maximum temperature of bone tissue were studied. To perform a comprehensive study, containing the effect of each input parameter and their interaction effects of parameters on the tissue temperature, the design of experiment (DOE) method was employed. The main findings of the research can be listed as follows.

- The ANOVA analysis shows that the rotational speed, feed rate, and drill diameter were effective parameters of the tissue temperature.

- The coefficient of determination (R^2) was 0.9453 for the response of tissue temperature which indicated that the regression equation can predict the temperature with good accuracy.

- The ANOVA results showed that by increasing the rotational speed, the temperature of the tissue first decreased until it reached a minimum value, and then with the further increase of the rotational speed, the tissue temperature began to increase.

- It was concluded that the maximum value of tissue temperature was reduced by increasing the feed rate of the drill. The reason was that by increasing the drill feed rate, the contact time between the bone tissue and the drill was reduced, and consequently, the amount of heat generated due to friction was reduced, so the temperature was also decreased.

- It was proved from the results that with an increase in the drill diameter, the maximum value of tissue temperature was reduced. The reason was that by increasing the drill diameter, the exit channel of the chips in the drill would be bigger, which would lead to a decrease in tissue temperature.

REFERENCES

[1] Hillery, M. T., Shuaib, I., Temperature Effects in the Drilling of Human and Bovine Bone, Journal of Materials Processing Technology, Vol. 92, 1999, pp. 302–308, https://doi.org/10.1016/S0924-0136(99)00155-7.

[2] Davidson, S. R., James, D. F., Measurement of Thermal Conductivity of Bovine Cortical Bone, Medical Engineering & Physics, Vol. 22, No. 10, 2000, pp. 741–747, https://doi.org/10.1016/S1350-4533(01)00003-0.

[3] Bachus, K. N., Rondina, M. T., and Hutchinson, D. T., The Effects of Drilling Force on cortical temperatures and Their Duration: an in Vitro Study, Medical Engineering & Physics, Vol. 22, No. 10, 2000, pp. 685–691, https://doi.org/10.1016/s1350-4533(01)00016-9.

[4] Davidson, S. R., James, D. F., Drilling in Bone: Modeling Heat Generation and Temperature Distribution, Journal of Biomechanical Engineering, Vol. 125, No, 3, 2003, pp. 305–314, https://doi.org/10.1115/1.1535190.

[5] Lundskog, J., Heat and Bone Tissue: An Experimental Investigation of the Thermal Properties of Bone Tissue and Threshold Levels for Thermal Injury, Scandinavian Journal of Plastic and Reconstructive Surgery, Vol. 9, 1972, pp. 1–80.

[6] Eriksson, R. A., Albrektsson, T., and Magnusson, B. J. S. J. O. P., Assessment of Bone Viability After

Heat Trauma: A Histological, Histochemical and Vital Microscopic Study in the Rabbit, Scandinavian Journal of Plastic and Reconstructive Surgery, Vol. 18, No. 3, 1984, pp. 261–268, https://doi.org/10.3109/02844318409052849.

[7] Hillery, M. T., Shuaib, I., Temperature Effects in the Drilling of Human and Bovine Bone, Journal of Materials Processing Technology, Vol. 92, 1999, pp. 302–308, https://doi.org/10.1016/S0924-0136(99)00155-7.

[8] Bachus, K. N., Rondina, M. T., and Hutchinson, D. T., The Effects of Drilling Force on Cortical Temperatures and Their Duration: an in Vitro Study, Medical Engineering & Physics, Vol. 22, No. 10, 2000, pp. 685–691, https://doi.org/10.1016/s1350-4533(01)00016-9.

[9] Brisman, D. L., The Effect of Speed, Pressure, and Time on Bone Temperature During the Drilling of Implant Sites, International Journal of Oral & Maxillofacial Implants, Vol. 11, No. 1, 1996, pp. 35–37.

[10] Boyne, P. J., Histologic Response of Bone to Sectioning by High-Speed Rotary Instruments, Journal of Dental Research, Vol. 45, No. 2, 1966, pp. 270–276, https://doi.org/10.1177/00220345660450020901.

[11] Moss, R. W., Histopathologic Reaction of bone to Surgical Cutting, Oral Surgery, Oral Medicine, Oral Pathology, Vol. 17, No. 3, 1964, pp. 405–414, https://doi.org/10.1016/0030-4220(64)90515-8.

[12] Spatz, S., Early Reaction in Bone Following the Use of Burs Rotating at Conventional and Ultra Speeds: A Comparison Study, Oral Surgery, Oral Medicine, Oral Pathology, Vol. 19, No. 6, 1965, pp. 808–816, https://doi.org/10.1016/0030-4220(65)90353-1.

[13] Abouzgia, M. B., James, D. F., Temperature Rise During Drilling Through Bone, The International Journal of Oral & Maxillofacial Implants, Vol. 12, No. 3, 1997, pp. 342–353.

[14] Iyer, S., Weiss, C., and Mehta, A., Effects of Drill Speed on Heat Production and the Rate and Quality of Bone Formation in Dental Implant Osteotomies, Part I: Relationship Between Drill Speed and Heat Production, The International Journal of Prosthodontics, Vol. 10, No. 5, 1997, pp. 411–414.

[15] Li, X., Zhu, W., Wang, J., and Deng, Y., Optimization of Bone Drilling Process Based on Finite Element Analysis, Applied Thermal Engineering, Vol. 108, 2016, pp. 211–220, https://doi.org/10.1016/j.applthermaleng.2016.07.125.

[16] Ying, Z., Shu, L. and Sugita, N., Experimental and Finite Element Analysis of Force and Temperature in Ultrasonic Vibration Assisted Bone Cutting, Annals of Biomedical Engineering, Vol. 48, 2020, pp. 1281–1290, https://doi.org/10.1007/s10439-020-02452-w.

[17] Dahibhate, R. V., Jaju, S. B., and Sarode, R. I., Development of Mathematical Model for Prediction of Bone Drilling Temperature, Materials Today: Proceedings, Vol. 38, 2020, pp. 2732–2736, https://doi.org/10.1016/j.matpr.2020.08.537.

[18] Iyer, S., Weiss, C., and Mehta, A., Effects of Drill Speed on Heat Production and the Rate and Quality of Bone Formation in Dental Implant Osteotomies. Part II: Relationship Between Drill Speed and Healing, The International Journal of Prosthodontics, Vol. 10, No. 6, 1997, pp. 536–540.

[19] Reingewirtz, Y., Szmukler- Moncler, S., and Senger, B., Influence of Different Parameters on Bone Heating and Drilling Time in Implantology, Clinical Oral Implants Research, Vol. 8, No. 3, 1997, pp. 189–197, https://doi.org/10.1034/j.1600-0501.1997.080305.x.

[20] Udiljak, T., Ciglar, D., and Skoric, S., Investigation into Bone Drilling and Thermal Bone Necrosis, Advances in Production Engineering & Management, Vol. 2, No. 3, 2007, pp. 103–112.

[21] Lee, J., Ozdoganlar, O. B., and Rabin, Y., An Experimental Investigation on Thermal Exposure During Bone Drilling, Medical Engineering & Physics, Vol. 34, No. 10, 2012, pp. 1510–1520, https://doi.org/10.1016/j.medengphy.2012.03.002.

[22] Shakouri, E., Sadeghi, M. H., Maerefat, M., and Shajari, S., Experimental and Analytical Investigation of the Thermal Necrosis in High-Speed Drilling of Bone, Proceedings of the Institution of Mechanical Engineers, Part H: Journal of Engineering in Medicine, Vol. 228, No. 4, 2014, pp. 330–341, https://doi.org/10.1177/0954411914524933.

[23] V. Tahmasbi, M. Ghoreishi, M. Zolfaghari, Temperature in Bone Drilling Process: Mathematical Modeling and Optimization of Effective Parameters, International Journal of Engineering, Transactions A: Basics, Vol. 29, No. 7, 2016, pp. 946–953, https://doi.org/10.5829/idosi.ije.2016.29.07a.09.

[24] Wang, W., Shi, Y., Yang, N., and Yuan, X., Experimental Analysis of Drilling Process in Cortical Bone, Medical Engineering & Physics, Vol. 36, No. 2, 2014, pp. 261–266, https://doi.org/10.1016/j.medengphy.2013.08.006.

[25] Singh, G., Gahi, A., Jain, V., and Gupta, D., An Investigation on Thermal Necrosis During Bone Drilling, International Journal of Machining and Machinability of Materials, Vol. 18, No. 4, 2016, pp. 341–349, https://doi.org/10.1504/ijmmm.2016.077708.

[26] Augustin, G., Davila, S., Mihoci, K., Udiljak, T., Vedrina, D. S., and Antabak, A., Thermal Osteonecrosis and Bone Drilling Parameters Revisited, Archives of Orthopaedic and Trauma Surgery, Vol. 128, 2008, pp. 71–77, https://doi.org/10.1007/s00402-007-0427-3.

Effect of Damping and Apparent Resistance on Energy

Harvesting from Piezoelectric Beam using Dynamic Stiffness Method

Majid Jabbari[1],*, Bijan Ahmadi[2], Sajad Hamedi[3]
Department of Mechanical Engineering, Khomeinishahr Branch, Islamic Azad University, Khomeinishahr, Isfahan, Iran
E-mail: jabbari@iaukhsh.ac.ir
*Corresponding author

Received: 13 October 2024, Revised: 15 December 2024, Accepted: 7 January 2025

Abstract: There are different sources of energy in the environment, and one of the sources that is converted into electrical energy is the vibrations of the environment. One of the methods of energy extraction is the use of piezoelectric materials. The main advantage of piezoelectric materials is their high-power density and ease of use. In this study, a dynamic stiffness method is developed to extract energy from the piezoelectric cantilever beam despite damping, impedance, and concentrated mass. In order to get the maximum energy for concentrated mass, it is suggested that the effect of some parameters on the proposed system be investigated. Such parameters include damping and impedance effects noted. According to this study, the effect of Kelvin-Voigt damping on the voltage amplitude of the initial acceleration at the first resonant frequency is almost linear, while this value changes homographically at the second resonant frequency. The change in voltage amplitude over the base acceleration amplitude due to the change in the viscous damping coefficient at the first and second resonant frequencies is almost the same, but the amount of reduction is greater in the second case. Also, the effect of impedance on this system is investigated, and the system response is obtained using the dynamic stiffness method. The effect of increasing the impedance on the conductivity of the beam tip relative to the foundation support is such that as impedance increases, its natural frequencies increase, thus making the system more rigid.

Keywords: Damping, Dynamic Stiffness, Energy Harvesting, Piezoelectric Beam

Biographical notes: Majid Jabbari is an assistant professor at the Department of Mechanical Engineering in Islamic Azad University, Khomeinishahr Branch. He received his PhD from IUT in 2016. His current research interests are in the field of intelligent piezoelectric structures and computer-aided design and engineering. **Bijan Ahmadi** graduated with a master's degree in Mechanical Engineering from the Islamic Azad University, Khomeinishahr Branch in 2017. **Sajad Hamedi** graduated with a master's degree in Mechanical Engineering from the Islamic Azad University, Khomeinishahr Branch in 2018.

1 INTRODUCTION

The energy supply of a system from its environment is generally called energy extraction. Research in this field has attracted the attention of many engineers and researchers with the development of wireless telecommunications and the advent of low-consumption electronic devices. For example, in wireless sensor networks, the power consumption of the sensors is low enough to supply energy from the environment. Therefore, by receiving the required energy from the environment, not only is there no need for batteries and external energy sources, but due to the lack of need to charge and replace the battery, the need for special care of the system disappears, which in turn reduces costs and Environmental pollution is very effective. The growth and development of low-power electronic devices, wireless technology, and wearable and portable smart devices have led to an increase in the use of these electronic devices by individuals. These devices have facilitated our communication while requiring electrochemical batteries to supply energy. In cases of emergency personnel and field environmental research, these devices generate a significant additional load. In addition, these loads increase again due to the need to carry heavy electrochemical batteries. With the continuous development of these devices and the achievements that have been achieved in the operation of these devices, the required electrical power has also been significantly increased. However, the increase in resources is not limited to the performance of the devices, in addition, due to the limited battery life, there is still a need for constant replacement. Electrical behavior depends on centralized parameters such as resistance, capacitor, so in the simulations performed, the parameters expressing the mechanical field are considered. In 2008, Erturk and Inman [1] examined the harmonic-excited SDOF model. They showed that the conventional harmonic base excitation relationship for predicting beam motion makes large errors and showed model errors. Then they presented modifying factors to improve the SDOF model by stimulating the harmonic base in transverse and longitudinal vibrations. They determined that the SDOF model could be used for high ratios of concentrated mass to mass of beam in transverse vibration. In fact, in the case where the concentrated mass is small, there is no conventional effective mass of the cantilever beams and rods, or it produces a negligible result compared to the system response. Therefore, the proposed modified SDOF model should be used. In 2004, Sodano et al. [2] obtained a more accurate estimate than the SDOF model for the systems with distributed parameters by the Rayligh-Ritz (RR) discrete formulation. In this approach, conversion of displacements that was selected in accordance with the basic functions was used. To confirm the method, which used the Hamilton principle, they performed a laboratory study for bimorph cantilever beam with PZT material. Dutoit et al. [3] proposed an SDOF model for MEM energy harvesters. His model consisted of Euler_Bernolli beam with a concentrated mass, the Equations of which were based on the RR discretization method and the Hamilton principle and dealt with the d-31 mode. They used the piezoelectric structural relationships and the resulting electrical displacement to express the relationship between electrical output and vibrational mode shapes. Hence, a non-optimized prototype presented the power density value $30\mu\frac{W}{cm^2}$. They examined the ratio of output power to various resistance and proposed considerations for the design of piezoelectric energy harvesters, which ultimately tested the validity of the presented model by performing experiments and comparisons with previous work. However, in the 1990s, Hagood et al. [4] had used RR discretization as a modeling approach for electromechanical systems. Using Hamilton's principle, they derived coupled motion Equations for any desired elastic structure with piezoelectric and passive electronic components and developed the proposed spatial models for the output voltage of the electrodes, the direct output load of the electrodes, and the state in which the piezoelectric electrodes are indirectly connected to an arbitrary electrical circuit with built-in voltage and current sources and finally, they used these Equations for the cantilever beam. In 2006, Chen et al. [5] proposed a micro-dimensional transducer model of a piezoelectric bimorph cantilever beam that used the Hamilton principle to derive matrices of discrete mass, stiffness, and damping in the transformed space. In accordance with the base deflection approach, they formulated the relationship between voltage and induced mechanical strain. Their analytical method was based on solving with one state, and their model showed that the induced voltage is proportional to the excitation frequency and width of the piezoelectric material and is inversely proportional to the beam length and damping coefficient. They hypothesized the effect of electromechanical bonding as viscous damping. Incorporating electromechanical bonding into mechanical Equations as viscous damping coefficients is a common approach for electromagnetic harvesters [6]. But the effect of electromechanical bonding on piezoelectrics is much more complex than considering it as a viscous damping. Rafique and Bonello [7] showed that considering the effect of electromechanical bonding as a viscous damper is valid only at low resistance loads. In addition, they proved a detailed validation of the modal analysis model presented in [8] for a bimorph beam without concentrated mass around the first resonance region, validating these relationships at frequencies higher than those considered in [8]. They investigated the effect of electromechanical bonding on the mechanical properties of the harvester, such as added resultant stiffness and damping, and by modal analysis and experiments showed that the resonant frequency and amplitude of the response due to electromechanical connection will be associated with changes. In 2013, Al-Adwani et al. [9] introduced a Shear Mode Harvester (SMH) to replace the energy harvesters in thickness mode (TMH) and longitudinal mode (LMH) in order to increase the harvested power. The reason for this choice was since the strain constant of piezoelectric material in shear is larger than the strain constant in longitudinal modes and thickness. To achieve the harvested energy in the shear mode, the piezoelectric element was polarized along a length parallel to the length of the electrode between the oscillator base and the concentrated mass. The base sinusoidal excitation in the direction of polarization causes the element to experience shear strain. They showed the optimal performance characteristics of SMH in comparison with TMH and LMH by providing numerical examples. In addition, they investigated the effect of resistance load and excitation frequency on SMH. The dynamic stiffness method relates the amplitude of the applied forces to the vibrational response of the system. This method is used to analyze systems that are harmonically excited and can provide an infinite number of natural modes for a finite number of node coordinates of continuous structures. In the present study, first, the formulas of the dynamic stiffness method are extracted, then the bimorph cantilever beam with concentrated mass at the desired distance from the end of the beam is divided into two elements and with the help of direct stiffness method, the dynamic stiffness matrix of the whole beam is obtained. This is done to damp the effect and apparent resistance in energy harvesting from the piezoelectric beam using the dynamic stiffness method.

2 THEORIES

Since common piezoelectric cantilever energy harvesters are often designed and manufactured as thin beams, and also most bimorph beams have thin structures, it seems reasonable to assume the beam as a Euler-Bernolli beam. The piezoelectric layers and the central layer are well bonded, and the electrodes that have been extended along the entire length of the beam are flexible and have a negligible thickness compared to the total thickness of the beam. In addition, the electrodes have been assumed to be well-conductive. Hence, only one electric potential difference along each electrode can be defined. Equations (1) and (2) are used to derive the behavior of moving beams with piezoelectric layers.

$$B\frac{\partial^4 u}{\partial x^4} + A\frac{\partial^5 u}{\partial x^4 \partial t} + c_a\frac{\partial u}{\partial t} + m\frac{\partial^2 u}{\partial t^2} = 0 \tag{1}$$

$$D_3 = d_{31}Y_P S + d_{31}c_P\dot{S} + \varepsilon_{33}^S E_3 \tag{2}$$

$$\begin{aligned} \varepsilon_{33}^S &= \varepsilon_{33}^T - d_{31}^2 Y_P \\ B &= Y_p I_p + Y_s I_s \\ A &= c_p I_p + c_s I_s \end{aligned} \tag{3}$$

Where S is axial strain, d_{31}, piezoelectric coefficient, E_3, Induced Electric Field, ε_{33}^T, permittivity at constant stress, D_3, component of electric displacement vector, Y_P, Modulus of elasticity of piezoelectric material, Y_S, Modulus of elasticity of the middle layer, C_P, Kelvin-Voigt damping coefficient for a piezoelectric layer, C_S, Kelvin-Voigt damping coefficient for a middle layer, I_P, the second torque of the surface around the neutral axis for a piezoelectric layer, I_S, the second torque of the surface around the neutral axis for a middle layer, m, mass per unit length, u, beam displacement in the y direction, C_a, the average viscous damping coefficient of ambience per unit length.

By placing Equation (2) in Gaussian law and deriving from it, the current intensity I as a function of time is obtained as Equation (4) where β, C_p, and f are respectively according to Equations (5) to (7). C_p in Equation (5) is the internal capacity of a piezoelectric layer, and h_{pc} in Equation (6) is the distance from the neutral axis to the midpoint of the piezoelectric layer [10].

$$i(t) = f\beta\int_0^L \frac{\partial^3 u}{\partial x^2 \partial t}dx - \frac{f}{a}C_p\dot{v} \tag{4}$$

$$\beta = -\mathrm{d}_{31}\mathrm{Y}_{\mathrm{p}}\mathrm{h}_{\mathrm{pc}}\mathrm{b} \tag{5}$$

$$C_p = \varepsilon_{33}^S\frac{bL}{h_p} \tag{6}$$

$$f = \begin{cases} 1, & for\ series \\ 2, & for\ parallel \end{cases} \tag{7}$$

h_p is the thickness of a piezoelectric layer, $v(t)$ is the voltage of the whole set is equal to 2 and 1 for series and parallel, respectively, L is the length, and b is the width of the beam.

For dynamic stiffness analysis, harmonic excitation is assumed. Hence, the displacement is obtained from Equations (3-30). Using the Equations (8) and (10), Equation (10) would be achieved [11].

$$u(x,t) = \tilde{u}(x)e^{j\omega t} \tag{8}$$

$$\begin{gathered} B(e^{j\omega t})\left(\frac{\partial^4\tilde{u}}{\partial x^4}\right) + A(j\omega)(e^{j\omega t})\left(\frac{\partial^4\tilde{u}}{\partial x^4}\right) + c_a(j\omega)e^{j\omega t}\tilde{u} \\ + m(j\omega)^2 e^{j\omega t}\tilde{u} = 0 \end{gathered} \tag{9}$$

$$\tilde{u}^{iv} - k\tilde{u} = 0 \tag{10}$$

$$k = \omega^{\frac{1}{2}}\left[\frac{m}{\hat{B}/\left(1-j\frac{ca}{m\omega}\right)}\right]^{\frac{1}{4}} \tag{11}$$

$$\hat{B} = B\left(1 + j\omega\frac{A}{B}\right) \tag{12}$$

Because the excitation is harmonic, parameters such as M (x, t), Q (x, t), θ (x, t) and v (t) are in the form of (13) Equations.

$$M(x,t) = \widetilde{M}(x)\,e^{j\omega t} \quad Q(x,t) = \tilde{Q}(x)\,e^{j\omega t} \quad \theta(x,t) = \widetilde{\theta}(x)\,cos\,e^{\,j\omega t} \quad v(t) = \widetilde{v}\,e^{j\omega t} \quad i(t) = \tilde{\imath}\,e^{j\omega t} \tag{13}$$

Using Equations (9), (12) and (4), the bending moment amplitude is obtained from (14) Equation [12].

$$\widetilde{M}(x) = \hat{B}\,\tilde{u}'' + \vartheta\widetilde{v} \quad \tilde{Q}(x) = \hat{B}\tilde{u}''' \tag{14}$$

If Z is the symbol of the apparent resistance of the electric charge, Equation (15) can be written. By placing (15) in (4), the voltage amplitude would be achieved by

Equation (16), in which G can be obtained in Equation (17) [13].

$$\tilde{v} = Z\tilde{\imath} \tag{15}$$

$$\tilde{v} = G\left[\tilde{\theta}(L) - \tilde{\theta}(O)\right] \tag{16}$$

$$G = \frac{j\omega f\beta}{j\omega\left(\frac{f}{a}\right)C_p + \frac{1}{Z}} \tag{17}$$

The dynamic stiffness matrix of the beam with the concentrated mass shown in "Fig. 3" can be determined by calculating relations (18) [14].

$$\mathrm{f} = \mathrm{Du} \qquad \mathrm{f} = [\tilde{F}_0\ \tilde{\Gamma}_0\ \ \tilde{F}_L\ \tilde{\Gamma}_L]^T \qquad \mathrm{u} = \left[\tilde{u}_0\ \tilde{\theta}_0\ \ \tilde{u}_L\ \tilde{\theta}_L\right]^T \tag{18}$$

It should be noted that the dimensions of the concentrated mass are assumed in comparison with the dimensions of the previous beam, therefore, the displacement of the end of the beam and the concentrated mass will be the same. also the moment of inertia of the concentrated mass is neglected. Hence, according to "Fig. 1", relation (19) is written in which $\mathrm{f_e}$ corresponds to relation (18) [15].

$$\mathrm{f_e} = \mathrm{D_e u} \qquad \mathrm{f_e} = \left[\tilde{F}_0\ \tilde{\Gamma}_0\ \ \tilde{F}_{L_e}\ \tilde{\Gamma}_{L_e}\right]^T \tag{19}$$

From "Fig. 1", the boundary conditions are obtained as Equations (20).

$$\tilde{M}(O) = -\tilde{\Gamma}_0 \quad \tilde{M}(L) = \tilde{\Gamma}_{L_e} \quad \tilde{Q}(O) = \tilde{F}_0 \quad \tilde{Q}(L) = -\tilde{F}_{L_e} \tag{20}$$

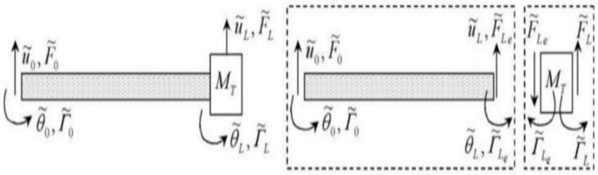

Fig. 1 Free body diagram of the beam with a concentrated mass (The damping forces are not displayed).

As a result, Equation (21) would be achieved by solving Equation (14) [16]. By applying the boundary conditions and Equation (21) in Equations (18) and (19), relations (22) to (25) are obtained.

$$\tilde{u}(x) = C_1 \cosh kx + C_2 \sinh kx + C_3 \cos kx + C_4\ \sin kx \tag{21}$$

$$\tilde{\Gamma}_0 = \hat{B}k^2(-C_1 + C_3) + \vartheta G\left(\tilde{\theta}_0 - \tilde{\theta}_L\right) \tag{22}$$

$$\tilde{\Gamma}_{L_e} = \hat{B}k^2(C_1 \cosh kL + C_2 \sinh kL - C_3 \cos kL - C_4\ \sin kL\ ) + \vartheta G\left(\tilde{\theta}_L - \tilde{\theta}_0\right) \tag{23}$$

$$\tilde{F}_0 = \hat{B}k^3(C_2 -\ C_4) \tag{24}$$

$$\tilde{F}_{L_e} = \hat{B}k^3(-C_2 \cosh kL - C_1 \sinh kL + C_4 \cos kL - C_3\ \sin kL\ ) \tag{25}$$

The relations from (22) to (25) can be written in matrix form as Equation (26).

$$\begin{bmatrix} \tilde{F}_0 \\ \tilde{\Gamma}_0 \\ \tilde{F}_{L_e} \\ \tilde{\Gamma}_{L_e} \end{bmatrix} = \vartheta G \begin{bmatrix} O & O & O & O \\ O & 1 & O & -1 \\ O & O & O & O \\ O & -1 & O & 1 \end{bmatrix} \begin{bmatrix} \tilde{u}_0 \\ \tilde{\theta}_0 \\ \tilde{u}_L \\ \tilde{\theta}_L \end{bmatrix} + \hat{B}k^2 \begin{bmatrix} 0 & k & 0 & -k \\ -1 & 0 & 1 & 0 \\ -k \sinh kL & -k \cosh kL & -k \sin kL & k \cos kL \\ \cosh kL & \sinh kL & -\cos kL & -\sin kL \end{bmatrix} \begin{bmatrix} C_1 \\ C_2 \\ C_3 \\ C_4 \end{bmatrix} \tag{26}$$

The relation (27) is obtained by computing the derivative of Equation (21). Hence, $\tilde{u}$ and $\tilde{\theta}$ at the beginning and end of the beam will be according to the relations (28) to (31), which are written in matrix form as Equation (3-65). u and C are also according to Equations (32) and (33).

$$\tilde{\theta}\ (x) = k\ (C_1 \sinh kx + C_2 \cosh kx - C_3 \sin kx + C_4\ \cos kx\ ) \tag{27}$$

$$\tilde{u}_0 = C_1 + C_3 \tag{28}$$

$$\tilde{\theta}_0 = k(C_2 +\ C_4) \tag{29}$$

$$\tilde{u}_L = C_1 \cosh kL + C_2 \sinh kL + C_3 \cos kL + C_4 \sin kL \tag{30}$$

$$\tilde{\theta}_L = k(C_1 \sinh kL + C_2 \cosh kL - C_3 \sin kL + C_4 \cos kL) \tag{31}$$

$$\mathrm{u} = \mathrm{AC} \qquad \mathrm{C} = [C_1 \quad C_2 \quad C_3 \quad C_4] \tag{32}$$

$$\mathrm{A} = \begin{bmatrix} 1 & 0 & 1 & 0 \\ 0 & k & 0 & k \\ \cosh kL & \sinh kL & \cos kL & \sin kL \\ k \sinh kL & k \cosh kL & -k \sin kL & k \cos kL \end{bmatrix}$$

$$(33)$$

To obtain f_e as a function of u, C from (30) is placed in Equation (24). If C is placed from Equation (30) to Equation (24), the dynamic stiffness matrix of the beam is obtained using the above relations as Equation (34), in which D_e is known as the dynamic stiffness matrix of the Beam without electric coupling and can be achieved in short circuit conditions [17].

$$\mathrm{D_e} = \begin{bmatrix} s_1 & s_2 & s_3 & s_4 \\ s_2 & s_5 & -s_4 & s_6 \\ s_3 & -s_4 & s_1 & -s_2 \\ s_4 & s_6 & -s_2 & s_5 \end{bmatrix} + \vartheta G \begin{bmatrix} 0 & 0 & 0 & 0 \\ 0 & 1 & 0 & -1 \\ 0 & 0 & 0 & 0 \\ 0 & -1 & 0 & 1 \end{bmatrix} \tag{34}$$

$$S_1 = \frac{\hat{B}k^3(cos\,kL\,.\,sinh\,kL + cosh\,kL\,.\,sin\,kL)}{\Delta}$$

$$S_2 = \frac{\hat{B}k^2(sin\,kL\,.\,sinh\,kL)}{\Delta}$$

$$S_3 = -\frac{\hat{B}k^3(sin\,kL + sinh\,kL)}{\Delta}$$

$$S_4 = \frac{\hat{B}k^2(cosh\,kL - cos\,kL)}{\Delta}$$

$$S_5 = \hat{B}k\frac{(cosh\,kL\,.\,sin\,kL - cos\,kL\,.\,sinh\,kL)}{\Delta}$$

$$S_6 = \hat{B}k\frac{(sinh\,kL - sin\,kL)}{\Delta}$$

According to “Fig. 2”, which shows the free diagram of the concentrated mass, the relations (35) and (36) can be written. In these two relations, M_T represents the concentrated mass, and I_T represents the moment of inertia of the concentrated mass. In Equation (35), C_T indicates the ambient damping coefficient per concentrated mass and is considered as Equation (37) in order to compare the dynamic stiffness method with modal analysis [18].

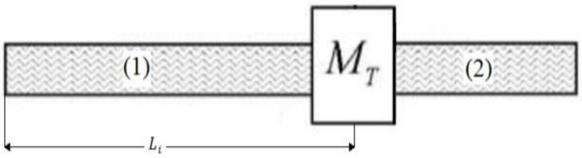

Fig. 2 Bimorph beam with concentrated mass at a distance of L_i from the base of the beam.

$$F_L - F_{L_e} = M_T\ddot{u}_L + c_T\dot{u} \tag{35}$$

$$\Gamma_L - \Gamma_{L_e} = I_T\ddot{\theta}_L \tag{36}$$

$$c_T = c_a\frac{M_T}{m} \tag{37}$$

Equations (38) and (39) would be achieved, if $e^{i\omega t}$ is removed from relations (35) and (36). Also, if Equation (13) is subtracted from (10), the relation (40) is obtained.

$$\tilde{F}_L - \tilde{F}_{L_e} = -\omega^2 M_T\,\tilde{u}_L + j\omega c_a\frac{M_T}{m}\tilde{u}_L \tag{38}$$

$$\tilde{\Gamma}_L - \tilde{\Gamma}_{L_e} = -\omega^2 I_T\,\tilde{\theta}_L \tag{39}$$

$$\mathrm{f} - \mathrm{f_e} = (\mathrm{D} - \mathrm{D_e})\mathrm{u} \tag{40}$$

By placing the relations (38) and (39) in (40), Equation (41) is written. Hence, by using relation (41), Equation (42) is obtained in which D_m corresponds to Equation (43) [19].

$$\begin{bmatrix} \tilde{F}_0 - \tilde{F}_0 \\ \tilde{\Gamma}_0 - \tilde{\Gamma}_0 \\ \tilde{F}_L - \tilde{F}_{L_e} \\ \tilde{\Gamma}_L - \tilde{\Gamma}_{L_e} \end{bmatrix} = \begin{bmatrix} 0 & 0 & 0 & 0 \\ 0 & 0 & 0 & 0 \\ 0 & 0 & -\omega^2 M_T - j\omega c_a\frac{M_T}{m} & 0 \\ 0 & 0 & 0 & -\omega^2 I_T \end{bmatrix} \begin{bmatrix} \tilde{u}_0 \\ \tilde{\theta}_0 \\ \tilde{u}_L \\ \tilde{\theta}_L \end{bmatrix} \tag{41}$$

$$\mathrm{D} = \mathrm{D_e} + \begin{bmatrix} 0 & 0 \\ 0 & \mathrm{D_m} \end{bmatrix} \tag{42}$$

$$\mathrm{D_m} = \begin{bmatrix} -\omega^2 M_T + j\omega c_a\frac{M_T}{m} & 0 \\ 0 & -\omega^2 I_T \end{bmatrix} \tag{43}$$

The matrix R is defined as relation (44), therefore, u is obtained according to relation (45) [18].

$$\mathrm{R} = \mathrm{D}^{-1} \tag{34}$$

$$\mathrm{u} = \mathrm{Rf} \tag{45}$$

Given that there is no external excitation on the concentrated mass, Equation (45) can be extended to Equation (46).

$$\begin{bmatrix} \tilde{u}_0 \\ \tilde{\theta}_0 \\ \tilde{u}_L \\ \tilde{\theta}_L \end{bmatrix} = \begin{bmatrix} R_{11} & R_{12} & R_{13} & R_{14} \\ R_{21} & R_{22} & R_{23} & R_{24} \\ R_{31} & R_{32} & R_{33} & R_{34} \\ R_{41} & R_{42} & R_{43} & R_{44} \end{bmatrix} \begin{bmatrix} \tilde{F}_0 \\ \tilde{\Gamma}_0 \\ 0 \\ 0 \end{bmatrix} \tag{46}$$

Using the presented relations, the output voltage is obtained as in Equation (47) [20]. Also, the output displacement as Equation (48) can be achieved by placing relations (46) and (47) in Equation (46) [20].

$$\tilde{v} = G\left[\frac{R_{41}R_{22}-R_{42}R_{21}}{\alpha}\right]\tilde{u}_0 + G\left[\frac{R_{42}R_{11}-R_{41}R_{12}-\alpha}{\alpha}\right]\tilde{\theta}_0 \quad (47)$$

$$\tilde{u}_L = \left(\frac{R_{31}R_{22}-R_{32}R_{21}}{\alpha}\right)\tilde{u}_0 + \left(\frac{R_{32}R_{11}-R_{31}R_{12}}{\alpha}\right)\tilde{\theta}_0 \quad (48)$$

Given that the sample beam is of the bimorph type, the relations related to the bimorph beam are extracted. The purpose of this work is to convert the beam into two arbitrary elements and to obtain the effect of concentrated mass displacement on the system. To obtain the output voltage of the system, Gauss's law for a piezoelectric layer is written as Equation (49).

$$q = -\int_o^L yY_p d_{31}\frac{b\partial^2 u}{\partial x^2}dx + \int_o^L b\varepsilon_{33}^S E_3 dx \quad (49)$$

Because the electrodes are completely conductive and the electrical potential is the same throughout the electrode, the amount of charge accumulated in the middle section of the top layer is obtained according to relation (50). Hence, by computing the derivative of Equation (50) with respect to time, the intensity of electric current through the external resistance will be under Equation (51) for a piezoelectric layer.

$$q = -h_{pc}Y_p d_{31}\int_o^L b\frac{\partial^2 u}{\partial x^2}dx - \frac{\varepsilon_{33}^S v(t)}{h_p}\int_o^L bdx \quad (50)$$

$$i(t) = -h_{pc}Y_p d_{31}\int_o^L b\frac{\partial^3 u}{\partial x^2\partial t}dx - \frac{\varepsilon_{33}^S \dot{v}(t)}{h_p}\int_0^L bdx \quad (51)$$

Equation (52) represents the current flowing through the apparent resistance for the whole system in series and parallel connection. Assuming the excitation of the system is harmonic, the output voltage amplitude is written according to relation (53).

$$i(t) = -h_{pc}Y_p d_{31} f\int_0^L b\frac{\partial^3 u}{\partial x^2\partial t}dx - \frac{f\varepsilon_{33}^S \dot{v}(t)}{ah_p}\int_0^L bdx \quad (52)$$

$$\tilde{v} = \left[\frac{-j\omega h_{pc}Y_p d_{31}}{\frac{-j\omega\varepsilon_{33}^S}{h_p}\left(\frac{f}{a}\right)\int_0^L bdx+\frac{1}{Z}}\right]\int_o^L bu''dx \quad (53)$$

Equation (53) can be used for beams of uniform thickness with the number of arbitrary elements and different cross sections, but for the system shown in "Fig. 2", the voltage amplitude is obtained as Equation (54) in which $\tilde{\theta}_{L_i}^{(2)}$ *and* $\tilde{\theta}_{L_i}^{(1)}$ are slope range in L_i for element 1 and element 2, respectively.

$$\tilde{v} = G\left[\tilde{\theta}_L - \tilde{\theta}_{L_i}^{(2)} + \tilde{\theta}_{L_i}^{(1)} - \tilde{\theta}_0\right] \quad (54)$$

Due to the continuity of the beam and the concentration of the mass, $\tilde{\theta}_{Li}^{(1)}$ and $\tilde{\theta}_{Li}^{(2)}$ are equal and the voltage amplitude is obtained according to Equation (27). Again, it is observed that the output voltage depends only on the beginning and end slopes of the beam and is independent of $\tilde{\theta}_{Li}$. This is because the width of the beam is uniform, but if the value of b changes at L_i then the output voltage will depend on the slope at the point L_i.

$$\tilde{v} = G\left[\tilde{\theta}_L - \tilde{\theta}_o\right] \quad (55)$$

If D_1 and D_2 are the dynamic stiffness matrices of element 1 and element 2 in "Fig. 2", respectively, the dynamic stiffness matrix of the whole system can be obtained by the direct stiffness method, in which the relations (56) to (58) are written for the whole system.

$$\mathrm{f} = \mathrm{Du} \quad (56)$$

$$\mathrm{u} = \left[\tilde{u}_0\ \tilde{\theta}_0\ \tilde{u}_{L_i}\ \tilde{\theta}_{L_i}\ \tilde{u}_L\ \tilde{\theta}_L\right] \quad (57)$$

$$\mathrm{f} = \left[\tilde{F}_0\ \tilde{\Gamma}_0\ \tilde{F}_{L_i}\ \tilde{\Gamma}_{L_i}\ \tilde{F}_L\ \tilde{\Gamma}_L\ \right] \quad (58)$$

Due to the lack of external excitation at points L and L_i, the values of external force and torque are equal to zero, hence by considering Equation (47), the voltage amplitude and displacement range of the end of the beam will be obtained by Equations (59) and (60) as a function of $\tilde{u}_0$ and $\tilde{\theta}_0$.

$$\tilde{v} = G\left[\frac{R_{61}R_{22}-R_{62}R_{21}}{\alpha}\right]\tilde{u}_0 + G\left(\frac{R_{62}R_{11}-R_{61}R_{12}-\alpha}{\alpha}\right)\tilde{\theta}_0 \quad (59)$$

$$\tilde{u}_L = \left(\frac{R_{51}R_{22}-R_{52}R_{21}}{\alpha}\right)\tilde{u}_0 + \left(\frac{R_{52}R_{11}-R_{51}R_{22}}{\alpha}\right)\tilde{\theta}_0 \quad (60)$$

3 SAMPLE SPECIFICATIONS AND RESULTS

The system is analyzed with the specifications given in "Table 1". Also, the damping ratios for the first two modes are $\zeta_1 = 0.0166$ and $\zeta_2 = 0.0107$, respectively, and the amount of concentrated mass (M_T) is equal to $0.5m_b$ [21]. By using the values ζ_1 and ζ_2 that are presented for two modes, and also Equation (60), the values C_a and A can be achieved. The values ζ_3 and ζ_4 are obtained by using the values ζ_1 and ζ_2, although it may not be valid for the higher modes of C_a and A [1].

Table 1 Dimensions and mechanical and physical properties of the system

h_p (mm)	0.267	L (mm)	60

h_s (mm)	0.300	(kg/m^3) Piezoelectric layer density	7800
Y_p (GPa)	6200	(kg/m^3) middle layer density	2700
Y_S (GPa)	7200	d_{31} (m/V)	-320×10^{-12}
b (mm)	25	ε_{33}^{T} $(\frac{F}{m})$	3.3646×10^{-8}

Because the maximum ratio of output voltage to base acceleration for a distance of 38 mm mass from the base occurs at the first resonant frequency, and at the second resonant frequency, the maximum ratio of output voltage to base acceleration for concentrated mass is obtained in 16 mm, the effect of Kelvin-Voigt damping coefficients and viscous damping for these two concentrated mass locations is investigated. For this purpose, the FRFs of voltage to base acceleration ratio are plotted for several A / B values and compared with the undamped mode (“Fig. 3”).

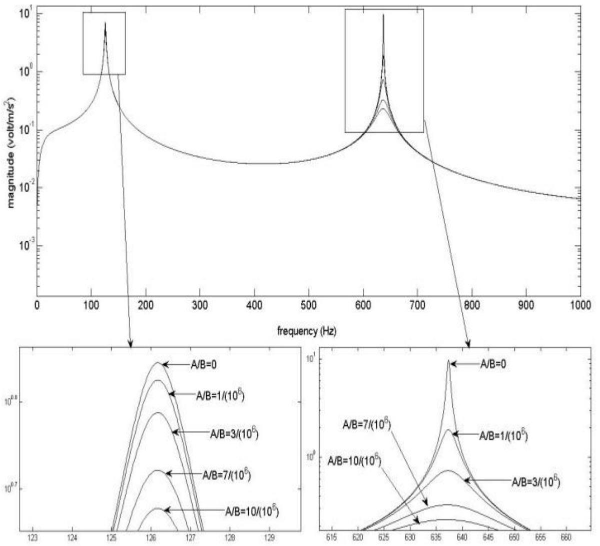

Fig. 3 The FRF of output voltage to base acceleration ratio to rise A/B values.

As shown in “Fig. 3”, despite the small A/B values, changing it greatly affects the system output. This effect on the output voltage to the base acceleration ratio at the second resonant frequency is greater, so that this decline has been 97.61% for changing the value of A / B from 0 to 10 × 10^{-6}, but at first resonant frequency, it dropped to 31.97% for changing the value of A / B from 0 to 10 × 10^{-6}. In the undamped mode for concentrated mass with 16 mm far from the base, the voltage to base acceleration ratio at the second resonant frequency is greater than this value at the first resonant frequency, but gradually with the growth of the value A/B due to the fact that the rise of damping at the second resonant frequency causes that the voltage falls considerably, the output voltage to base acceleration ratio at the first resonant frequency compared to this value in the second resonant frequency is remarkable. As far as A / B is equal to 6 × 10 × 10^{-6}, the proportion of output voltage to base acceleration at the first resonant frequency is 4.76 volt/ m and at the second resonant frequency is 0.2314 volt/ m (“Fig. 4”).

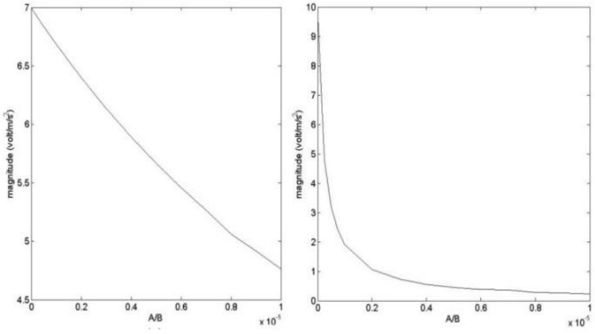

(b) **(a)**

Fig. 4 (a): The ratio of output voltage to base acceleration at the second resonant frequency in accordance with A/B changes, and (b): The ratio of output voltage to base acceleration at the first resonant frequency in accordance with A/B changes.

As can be seen in “Fig. 4”, the decline in output voltage at the first resonant frequency occurs due to the growth of damping with a gentle slope and almost linearly, but at the second resonant frequency this drop was initially abrupt, then the effect of growth of this damping on the system output will be dropped by rising the A/B. The diagrams in “Fig. 4” are drawn based on A/B variations. These changes for $\omega_{r_1} = 126.21$ Hz and $\omega_{r_2} = 637.4$ Hz are equal to 0.004 < ζ_1<0 and 0.02< ζ_2< 0. For this reason, a marked drop in voltage at the second resonant frequency can be justified. For the concentrated mass with 38 mm far from the base, the effect of A/B changes is shown in “Fig. 5”.

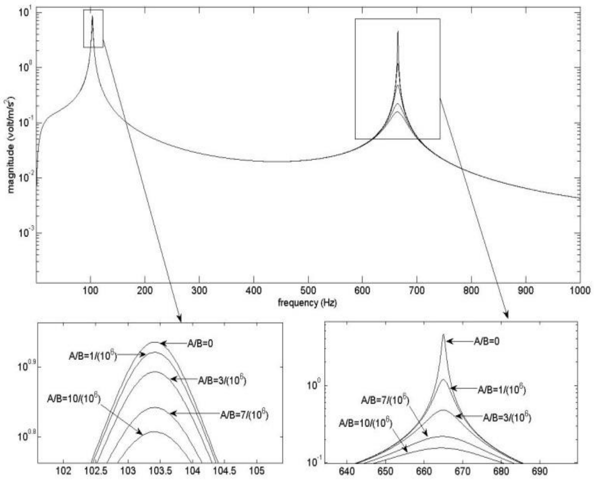

Fig. 5 The ratio of output voltage to base acceleration based on excitation frequency to raise the values A/B 38.

As in “Fig. 3”, the effect of the A/B changes for the second resonant frequency on the graph is very high, but this decline occurs at the first resonant frequency with a gentle slope and almost linearly (“Fig. 6”).

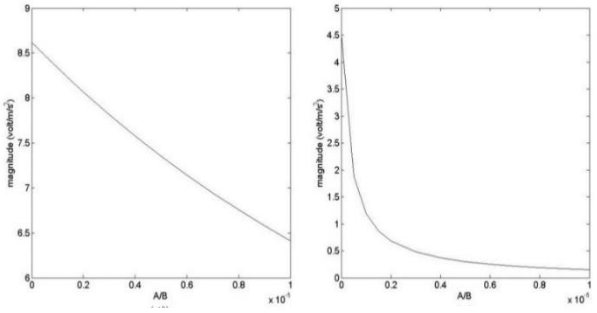

(a) **(b)**

Fig. 6 (a): The ratio of output voltage to base acceleration at the first resonant frequency in accordance with A/B changes for 38, and (b): The ratio of output voltage to base acceleration at the second resonant frequency in accordance with A / B changes for 38.

For the concentrated mass with 38 mm far from the base, the proportion of voltage to base acceleration from the second resonant frequency is less than this ratio at the first resonant frequency in which by changes of A/B, it would decline to 96.5% and 25.65%, respectively. It should be noted that this range of changes for A / B is equal to $0 < \zeta_1 < 0.0032$ and $0 < \zeta_2 < 0.0209$.

The FRFs of voltage to base acceleration ratio for various values of C_a/m for a system with concentrated mass and a distance of 16 mm are according to “Fig. 7”.

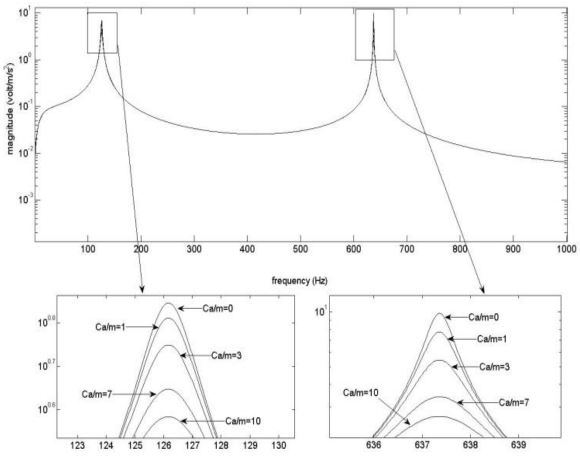

Fig. 7 The ratio of output voltage to base acceleration based on excitation frequency to raise the values C_a/m.

Unlike Kelvin-White damping, the changes of viscous damping upon the reduction of the voltage-to-acceleration ratio for the first and second resonant frequencies follow almost the same pattern (“Fig. 8”). However, the graph changes for the second resonant frequency are greater than the first resonant frequency, so that this decline is 72.66% and 45.19%, respectively. The range of changes from 0 to 10 for C_a / m is equal to $0 < \zeta_1 < 0.0063$ and $0 < \zeta_2 < 0.0012$.

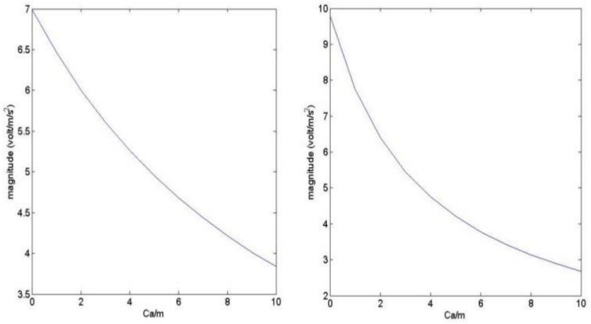

(a) **(b)**

Fig. 8 (a): The ratio of output voltage to base acceleration at the first resonant frequency in accordance with C_a/m changes for 16, and (b): The ratio of output voltage to base acceleration at the second resonant frequency in accordance with C_a/m changes for 16.

(b)

For a system with a concentrated mass at a distance of 38 mm from the base, the FRFs of the voltage to base acceleration ratio have been drawn (“Fig. 9”).

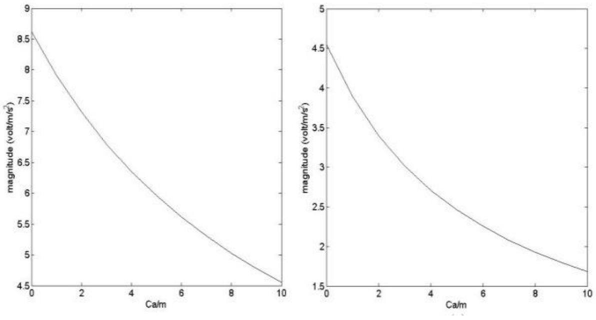

(a) **(b)**

Fig. 9 (a): The ratio of output voltage to base acceleration at the first resonant frequency in accordance with C_a / m changes for 38, and (b): The ratio of output voltage to base acceleration at the second resonant frequency in accordance with C_a / m changes for 38.

Similar to what happens for the concentrated mass at a distance of 16 mm due to the change in C_a/m, the reduction in diagrams 4-16 a and b is almost the same, and this decline is greater at the second resonant frequency. This drop for the first and second resonant frequencies is 47.20% and 62.95%, respectively. The range of changes from 0 to 10 for C_a / m is equal to $0 < \zeta_1 < 0.0077$ and $0 < \zeta_2 < 0.0012$. As a result, it can be said that a little growth in A/B from the undamped mode causes a sharp drop in the proportion of voltage to base acceleration for the second resonant frequency, although it should be noted that this decline would be gentle for the first resonant frequency. The reason is that the rise of A/B causes the greater growth of ζ_r for the next modes of the system. Therefore, one of the factors that reduces the effect of the system response in the resonant frequencies is Kelvin-Voigt damping. Regarding the effect of viscous damping, it should be said that the rise of C_a/m causes less growth in ζ_r for higher modes of the system. Despite this, the decline in the second resonant frequency is greater than the decline in the first resonant frequency, which, unlike Kelvin-Voigt damping, does not cause a sudden reduction in system output due to the rise of damping frequency in the second resonant frequency and occurs gently. Therefore, because the proportion of the voltage to acceleration drops sharply due to the rise of Kelvin-Voigt damping coefficients in the second resonant frequency, the best place for energy harvesting is where the concentrated mass is 38mm away from the base.

According to the analysis performed in the previous section, a system with a concentrated mass that is 38 mm away from the base was proposed. Therefore, this system is used to investigate the effect of apparent resistance. In addition, it is assumed that the qualification factors remain constant due to the displacement of the concentrated mass, according to which the relations $C_a/m = 7.71934$ and $A/B = 8.5000198 \times 10^{-6}$ are established. The output power for the system changes with the alteration of the apparent resistance. These changes have been drawn for a resistor R of 10 Ω, which is very close to the short circuit conditions ("Figs. 4-12"). The harvested voltage rises with increasing R to reach its maximum in open-circuit mode. The effect of increasing the apparent resistance ("Fig. 10") on the portability of the beam tip relative to the base is such that as the apparent resistance rises, its natural frequencies grow, hence making the system more rigid [22].

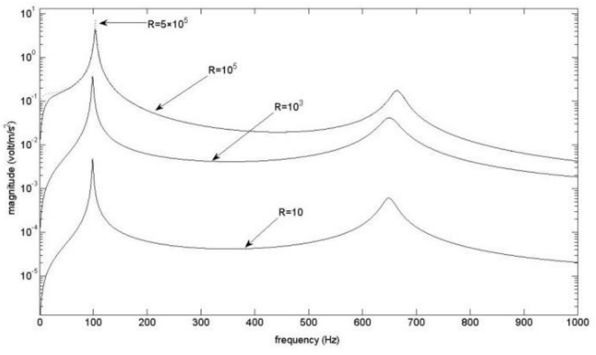

Fig. 10 The FRF of Voltage to Base acceleration ratio with rise of apparent resistance in ohms from short circuit to open circuit mode.

Increasing the apparent resistance from 10^3 Ω to 10^5 Ω raises the natural first and second frequencies by 5.04% and 2.19%. The growth in natural frequencies can be neglected by raising the apparent resistance from 10^5 Ω to 5×10^5 Ω. It should be noted that the frequency of the peaks of the transmittable diagram overlaps the FRF frequency of the voltage-to-base acceleration ratio.

In some cases, the net load of the capacitor is expressed as Z = 1 / jωC in which the capacitance of the capacitor is $C = nC_p$. The transmissibility diagram of the beam tip relative to the beam base is drawn to rise the values of n: n = 0 is equivalent to the open circuit conditions, n = ∞ is equivalent to the short circuit state, and $n = 10^{-4}$ is considered when experimental open circuit conditions are in place [23]. A comparison of "Figs. 11 and 12" shows that the system becomes more rigid as the conditions change from short circuit to open circuit, but the reduction in the amplitude of the diagram is negligible.

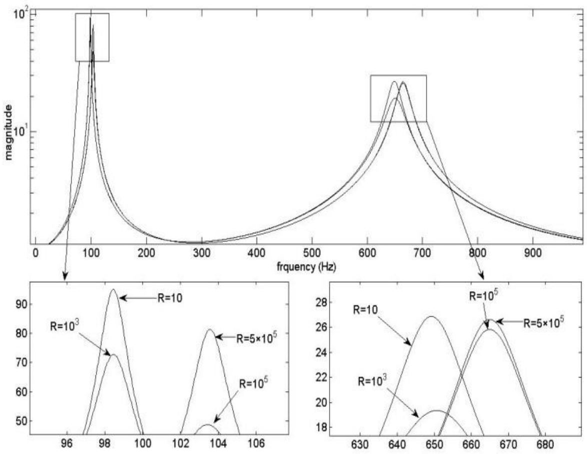

Fig. 11 Transmissibility of the beam tip relative to the beam base to raise the apparent resistance values ohms from the short circuit state to the open circuit state.

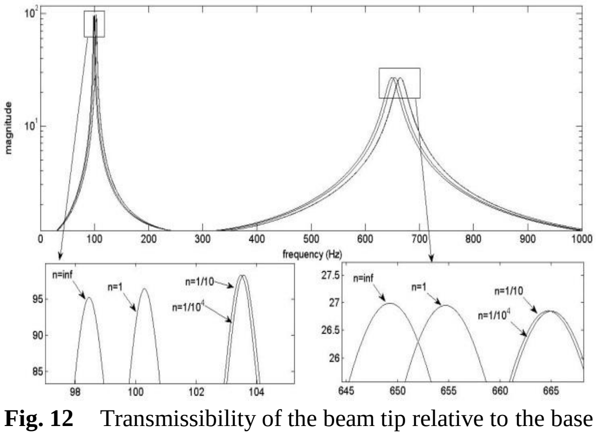

Fig. 12 Transmissibility of the beam tip relative to the base beam in accordance with changes in various values of capacitor load.

4 CONCLUSIONS

In this study, a dynamic stiffness method was developed to harvest energy from a piezoelectric beam despite damping and apparent resistance with concentrated mass. The intended purpose is to investigate the effect of damping and apparent resistance on energy harvesting from piezoelectric beams using the dynamic stiffness method. According to the results obtained in this study, changes in Kelvin-Voigt damping coefficients and viscous damping were investigated in which with rising the Kelvin-Voigt damping coefficient from undamped mode, the proportion of voltage amplitude to base acceleration in the second resonant frequency dropped sharply, but with further growth of this coefficient, the amplitude declined with a gentle slope. A reduction in FRF of voltage to acceleration ratio at the first resonant frequency occurred almost linearly with a gentle slope due to the rise in Kelvin-Voigt damping. The effect of rising the viscous damping on the FRF amplitude of voltage to base acceleration ratio in the first resonant frequency resembled the changes in the Kelvin-Voigt damping coefficient, however the effect of this coefficient on decreasing the amplitude of the diagram in the second resonant frequency was not as severely as before and was almost close to decline of the diagram amplitude in the first resonant frequency.

Regarding the effect of damping coefficients for the maximum output voltage harvesting, a system was proposed whose concentrated mass was 38 mm away from the base, and the effect of apparent resistance and capacitor load on the transmissibility of the beam tip relative to the base was investigated for this system. As a result of raising the resistance load from the short circuit to open circuit conditions, the natural frequencies of the system became more magnified. In fact, raising the resistance load made the system more rigid. A similar change in the system's natural frequencies occurred from short circuit to open circuit conditions to change the capacitor load. It should be noted that the reduction in the FRF of the Voltage to acceleration ratio was significant in the resistance load alteration, although the reduction of this amplitude in changing the capacitor load could be ignored. Given that the dynamic stiffness matrix of the beam element was obtained with a uniform cross section and concentrated mass, the element matrix can be used to analyze the set of interconnected beams. Also, a trapezoidal beam can be divided into different parts, and the dynamic stiffness matrix of each segment can be calculated separately. Finally, by assembling the stiffness matrices of the elements by the direct stiffness method, the electrical output for this beam can be obtained. The DSM method can be used for a variety of boundary conditions, so obtaining electrical outputs for different boundary conditions can be deliberated.

REFERENCES

[1] Erturk, A., Inman, D. J., On Mechanical Modeling of Cantilevered Piezoelectric Vibration Energy Harvesters, J. Intell. Mater. Syst. Struct., Vol. 19, 2008, pp. 1311-1325.

[2] Sodano, H. A., Park, G., and Inman, D. J., Estimation of Electric Charge Output for Piezoelectric Energy Harvesting, Strain, Vol. 40, 2004, pp. 49-58.

[3] DuToit, N. E., Wardle, B. L., and Kim, S. G., Design Considerations for MEMs-Scale Piezoelectric Mechanical Vibration Energy Harvesters, Integrated Ferroelectrics, Vol. 71, 2005, pp. 121–160.

[4] Hagood, N. W., Chung, W. H., and Von Flotow, A., Modelling of Piezoelectric Actuator Dynamics for Active Structural Control, J. Intell. Mater. Syst. and Struct., 1990.

[5] Chen, S. N., Wang, G. J., and Chien, M. C., Analytical Modeling of Piezoelectric Vibration-Induced Micro Power Generator, Mechatronics, Vol. 16, 2006, pp. 379-387.

[6] Williams, C. B., Yates, R. B., Analysis of a Micro-Electric Generator for Microsystems, Sensors and Actuators A, Vol. 52, 1996, pp. 8-11.

[7] Rafique, S., Bonello, P., Experimental Validation of a Distributed Parameter Piezoelectric Bimorph Cantilever Energy Harvester, Smart Mater. Struct., Vol. 19, 2010, pp. 094008.

[8] Erturk, A., Inman, D. J., A Distributed Parameter Electromechanical Model for Cantilevered Piezoelectric Energy Harvesters, ASME J. Vibr. Acoust., Vol. 130, 2008, pp. 041002.

[9] Aladwani, A., Aldraihem, O., and Baz, A., Single Degree of Freedom Shear-Mode Piezoelectric Energy Harvester, ASME J. Vibr. Acoust., Vol. 135, 2013, pp. 051011.

[10] Bonello, P., Rafique, S., J., Modeling and Analysis of Piezoelectric Energy Harvesting Beams Using the Dynamic Stiffness and Analytical Modal Analysis Methods, ASME J. Vibr. Acoust., Vol. 133, 2011, pp. 011009.

[11] Banerjee, J. R., Sobey, A. J., Dynamic Stiffness Formulation and Free Vibration Analysis of A Three-Layered Sandwich Beam, International Journal of Solids and Structures, Vol. 42, 2005, pp. 2181–2197.

[12] Banerjee, J. R., Cheung, C. W., Morishima, R., Perera, M., and Njuguna, J., Free Vibration of A Three-Layered Sandwich Beam Using the Dynamic Stiffness Method and Experimen, International Journal of Solids and Structures, Vol. 44, 2007, pp. 7543–7563.

[13] Khalili S. M. R., Nemati N., Malekzadeh, K., and Damanpack, A. R., Free Vibration Analysis of Sandwich Beams Using Improved Dynamic Stiffness Method, Composite Structures, Vol. 92, 2010, pp. 387–394.

[14] Damanpack, A. R., Khalili, S. M. R., High-Order Free Vibration Analysis of Sandwich Beams with A flexible Core Using Dynamic Stiffness Method, Composite Structures, Vol. 94, 2012, pp. 1503–1514.

[15] Jafari, M., Mahjoob, M. J., An Exact Three-Dimensional Beam Element With Nonuniform Cross Section, School of Mechanical Engineering, Vol. 77, 2010, pp. 61–72.

[16] Ratazzi, A. R., Bambill, D. V., and Rossit, C. A., Free Vibrations of Beam System Structures with Elastic Boundary Conditions and an Internal Elastic Hinge, Chinese Journal of Engineering, Vol. 89, 2013, pp. 556–568.

[17] Su, H., Banerjee, J. R., Development of Dynamic Stiffness Method for Free Vibration of Functionally Graded Timoshenko Beams, Computers and Structures, Vol. 147, 2015, pp. 107–116.

[18] Jeon, Y. B., Sood, R., Jeong, J. H., and Kim, S. G., MEMS Power Generator with Transverse Mode Thin Film PZT, Sensors and Actuators A, Vol. 122 2005, pp. 16–22.

[19] Erturk, A., Inman, D. J., An Experimentally Validated Bimorph Cantilever Model for Piezoelectric Energy Harvesting From Base Excitations, Smart Mater. Struct., Vol. 18, 2009, pp. 79–88.

[20] Leung, Y. T., Dynamic Stiffness Method for Exponentially Varying Harmonic Excitation of Continuous Systems, Journal of Sound and Vibration, Vol. 98, No. 3, 1985, pp. 337-347.

[21] Lin, J. H., Wu, X. M., Ren, T. L., and Liu, L. T., Modeling and Simulation of Piezoelectric MEMS Energy Harvesting Device, Integrated Ferroelectrics, Vol. 95, 2007, pp. 128–141.

[22] Kim, J. E., Kim, Y. Y., Analysis of Piezoelectric Energy Harvesters of a Moderate Aspect Ratio With a Distributed Tip Mass, Journal of Vibration and Acoustics, Vol. 115, 2011, pp. 178–194.

[23] Aladwani, A., Arafa, M., Aldraihem, O., and Baz, A., Cantilevered Piezoelectric Energy Harvester With a Dynamic Magnifier, ASME J. Vibr. Acoust., Vol. 134, 2012, pp. 031004.

On the Analysis of Two-Dimensional Functionally Graded Rotating Thick Hollow Cylinder

Mostafa Omidi Bidgoli[1, *]
Department of Mechanical Engineering, Islamic Azad University, Badroud branch, Badroud, Iran
E-mail: mostafaomidibidgoli@gmail.com
*Corresponding author

Mohammad Hosseini[2], **Ali Fata**[3]
Department of Mechanical Engineering, University of Hormozgan, Bandar Abbas, Iran
E-mail: mohammad.hosseini@hormozgan.ac.ir, fata.ali@gmail.com

Received: 10 September 2024, Revised: 25 February 2025, Accepted: 18 March 2025

Abstract: Rotary components are widely used in industries. There is both mechanical and thermal loading in most rotating cylinder applications. On the other hand, functionally graded material has better performance under different loads. Therefore, a finite length two dimensional functionally graded material (2D-FGM) thick hollow cylinder under angular velocity is investigated, in this research. Volume fraction distribution of functionally graded material and geometry of the cylinder are axisymmetric but not uniform along the radial and axial directions. The finite element method based on Rayliegh-Ritz energy formulation is applied to obtain the governing Equation and associated boundary conditions of a 2D-FG thick hollow cylinder. Using this method, the effects of the power law exponents and angular velocity on the displacements and distribution of stresses are investigated for simply supported 2D-FG thick hollow cylinder. The results indicate that 2D-FGM facilitates improved design, allowing for better control of both maximum stresses and stress distribution through material distribution.

Keywords: 2D Functionally Graded Material, FEM, Rotating Cylinder, Thick Hollow Cylinder

Biographical notes: Mostafa Omidi Bidgoli is an assistant professor and accomplished mechanical engineer specializing in solid mechanics, with expertise in FGM, stress and strain analysis, and creep analysis. He received his Ph.D. in

Mechanical Engineering from the University of Kashan in 2019. He is an assistant professor at IAU, Badroud branch. **Mohammad Hosseini** is an assistant professor and accomplished mechanical engineer specializing in solid mechanics, with expertise in nano-structures, MEMS, and NEMS, stress analysis, and finite element methods. He received his Ph.D. in Mechanical Engineering from Shahid Chamran University of Ahvaz in 2017. **Ali Fata** is an associate professor of Mechanical Engineering at Hormozgan University, specializing in Manufacturing Engineering and advanced materials processing. He received his Ph.D. in Mechanical Engineering from Amir Kabir University in 2012.

1 INTRODUCTION

Rotating cylinders with functionally graded materials (FGMs) have attracted much attention recently as an innovation in materials, engineering, and structural design. FGMs are heterogeneous composite materials whose mechanical properties vary continuously between several different materials. Also, the rotary cylinder is widely used in various industries. Functionally graded cylinders are used in internal combustion engines, gas turbines, medicine, etc. The presence of variable stresses and thermal fields in rotating cylinders requires careful design and the use of materials with specific properties. FGMs have the ability to adapt to these challenges by gradually changing the composition and properties of the materials along the design. In most rotating cylinder applications, there is both mechanical and thermal loading. The cylinder can be made of functionally graduated to perform optimally under different loads. It is necessary to theoretically examine the behavior of the functionally graded structure before the construction process, considering the high costs of laboratory tests. In the last few years, much research has been carried out to investigate the behavior of the rotating functional graduated cylinder, which will be discussed in the following.

Shi and Xie [1] presented an exact solution for a hollow FG cylinder under the simultaneous action of an applied magnetic field and internal pressure. They analyzed residual stresses caused by unloading internal pressure and the effect of some parameters on the plastic zone size. Li et al. [2] derived the governing Equation of a functionally graded cylinder or circular disk. The structure was under axisymmetric mechanical and thermal loads. They investigate the effect of some parameters, such as the inhomogeneity parameter, thermal and magnetic fields, internal pressure, and rotating velocity. Using the Pseudospectral Chebyshev Method, Yarimpabuç and Çalişkan [3] investigated the elastic behavior of FG rotating hollow cylindrical pressure vessels. Daghigh et al. [4] discussed the time-dependent behavior of FGM rotating disks of variable thickness subject to mechanical load and uniform temperature. In the frameworks of first-order shear deformation theory, Sedighi et al. [5] studied the time-dependent creep behavior of thick-walled cylinders under internal pressure, and heat flux at the inner and outer surfaces has been investigated. Omidi Bidgole et al. [6] used first-order shear deformation theory to analyze transient stress and deformations of short-length FG rotating cylinders subjected to thermal and mechanical loads on a friction bed. Based on the finite element method, Maitra et al. [7] presented an analysis for rotating truncated radially FG conical shells under constant and variable internal pressure. Creep analysis of an FG rotating disc of variable thickness was discussed by Saadatfar et al. [8]. They explained the effect of design parameters on the creep behavior of the disc. Using the Biot poroelastic law, Babaei et al. [9] derived the governing Equation and discussed the dynamic behavior of the FG-saturated porous rotating thick truncated cone. Xu et al. [10] presented a model to explain elastic wave propagation in a 2D-FG thick hollow cylinder. Yarımpabuç [11] used a closed-form solution to study the transient thermal stress analysis of a radially FG hollow cylinder subjected to high-temperature difference and periodic rotation effect. Jabbari and Zamani Nejad [12] investigated the effect of thermal and mechanical loads on the strain and stress distribution of rotating radially FG shells of variable thickness. Mehditabar et al. [13] studied the mechanical behavior of radially FG rotating hollow cylindrical shells under dynamic loading. Gharibi et al. [14] derived and solved the governing Equation of radially FG rotating thick cylindrical pressure vessels. Jabbari et al. [15] analyzed axially FG rotating thick cylindrical of variable thickness subject to thermo-elastic loads. They used higher-order shear deformation theory and the multilayer method to derive the governing Equation.

Jafari Fesharaki et al. [16] presented a 2D solution for the electro-mechanical behavior of functionally graded piezoelectric hollow cylinders under 2D electro-mechanical loads.

Zafarmand and Hasani [17] studied the elastic behavior of a 2D-FGM rotating disk of variable thickness. They investigate the effect of the thickness profile and material inhomogeneity index on the displacement distribution and stresses. Dai et al. [18] analyzed displacements and stresses of radially FG piezoelectric rotating hollow cylinders. Also, much research has been done on rotating structures in addition to the ones reviewed in this article [19-44].

As can be seen, much research has been done on rotating functionally graduated cylinders. Most of the articles have assumed material changes either in the radial direction or in the axial direction. In this paper, the stress analysis of 2D-FGM rotating thick hollow cylinders has been investigated for the first time. The problem is modeled using 2D axisymmetric elasticity theory and the finite element method based on the Rayleigh-Ritz energy formulation. The influence of power law exponents and rotational velocity on the distribution of displacements and stresses is considered.

2 MATERIAL AND GEOMETRY OF STRUCTURE

Figure 1 shows a thick hollow cylinder, where r and z are the radial, and length axis of cylindrical coordinate system.

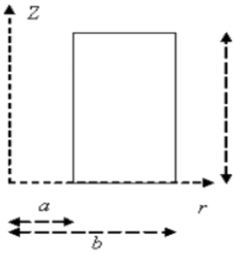

Fig. 1 Geometry of the cylinder.

The inner surface of the cylinder is made of ceramics, and the outer surface is made of metal alloys. Material properties vary through both the radial and axial directions. The volume fraction of constituent materials can be expressed as:

$$\mathrm{Vc}_1=\left(1-\left(\frac{\mathrm{r}-\mathrm{a}}{\mathrm{b}-\mathrm{a}}\right)^{\mathrm{n_r}}\right)\left(1-\left(\frac{\mathrm{z}}{\mathrm{L}}\right)^{\mathrm{n_z}}\right) \tag{1}$$

$$\mathrm{Vc}_2=\left(1-\left(\frac{\mathrm{r}-\mathrm{a}}{\mathrm{b}-\mathrm{a}}\right)^{\mathrm{n_r}}\right)\left(\frac{\mathrm{z}}{\mathrm{L}}\right)^{\mathrm{n_z}} \tag{2}$$

$$\mathrm{Vm}_1=\left(\frac{\mathrm{r}-\mathrm{a}}{\mathrm{b}-\mathrm{a}}\right)^{\mathrm{n_r}}\left(1-\left(\frac{\mathrm{z}}{\mathrm{L}}\right)^{\mathrm{n_z}}\right) \tag{3}$$

$$\mathrm{Vm}_2=\left(\frac{\mathrm{r}-\mathrm{a}}{\mathrm{b}-\mathrm{a}}\right)^{\mathrm{n_r}}\left(\frac{\mathrm{z}}{\mathrm{L}}\right)^{\mathrm{n_z}} \tag{4}$$

Therefore, the material properties at each point can be obtained by the linear rule of mixtures as:

$$\mathrm{E}=\mathrm{Ec}_1\mathrm{Vc}_1+\mathrm{Ec}_2\mathrm{Vc}_2+\mathrm{Em}_1\mathrm{Vm}_1+\mathrm{Em}_2\mathrm{Vm}_2 \tag{5}$$

For instance, the volume fraction distribution of the second ceramic and the variation of modulus of elasticity through the cylinder for typical values of $\mathrm{n_r}=\mathrm{n_z}=2$ are shown in “Figs. 2 and 3”, respectively. In this case, a=1 m, b=1.5 m, and L=1 m. The essential constituents of the 2D-FGM cylinder are presented in “Table 1”.

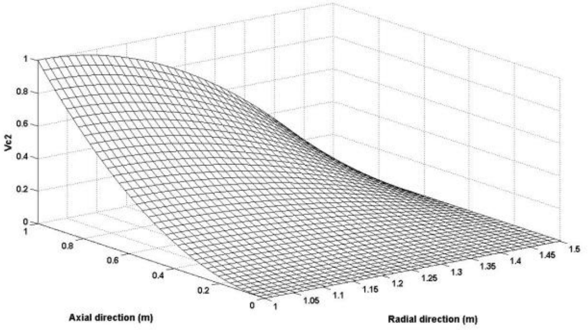

Fig. 2 Volume fraction distribution of second ceramic through the cylinder for $n_r = n_z = 2$.

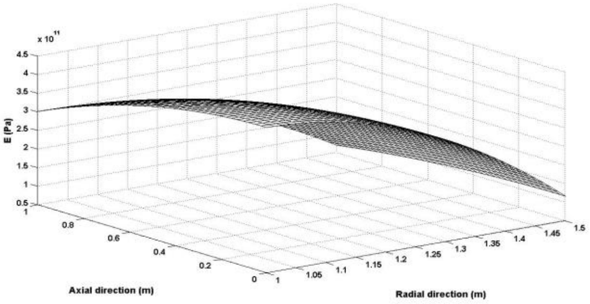

Fig. 3 Distribution of modulus of elasticity through the cylinder for $n_r = n_z = 2$.

Table1 Basic constituent of 2D-FGM cylinder

Constituent	Material	E (GPa)	Density (kg/m3)
m_1	Ti6Al4V	115	4515
m_2	Al 1,100	69	2715
c_1	SiC	440	3210
c_2	Al2O3	300	3470

3 Governing Equations of Rotating Thick Hollow Cylinder

Figure 1 shows a rotating thick hollow cylinder. Based on the axial symmetry assumption, the formulation is reduced to two dimensions. Due to axisymmetric geometry, axisymmetric material properties, and axisymmetric load distribution, the circumferential displacement, shear stresses, and strains in r_θ and θ_z planes are zero. Governing Equations in axisymmetric cylindrical coordinates were obtained as:

$$\frac{\partial\sigma_{rr}}{\partial r}+\frac{(\sigma_{rr}-\sigma_{\theta\theta})}{r}+\frac{\partial\tau_{rz}}{\partial z}+\rho(r,z)\,r\,\omega^2=0 \tag{6}$$

$$\frac{\partial \tau_{rz}}{\partial r}+\frac{\partial \sigma_{zz}}{\partial z}+\frac{\tau_{rz}}{r}=0 \tag{7}$$

Linear strain-displacement relations are:

$$[\varepsilon]=\begin{bmatrix}\varepsilon_{rr}\\ \varepsilon_{\theta\theta}\\ \varepsilon_{zz}\\ \varepsilon_{rz}\end{bmatrix}=\begin{bmatrix}\dfrac{\partial u}{\partial r}\\ \dfrac{u}{r}\\ \dfrac{\partial v}{\partial z}\\ \dfrac{1}{2}\left(\dfrac{\partial u}{\partial z}+\dfrac{\partial v}{\partial r}\right)\end{bmatrix} \tag{8}$$

Where u and v are the radial and axial displacements, respectively. "Eq. (8)" could be rewritten as:

$$[\varepsilon]=[d]\{f\} \qquad \{f\}=\begin{Bmatrix}u\\ v\end{Bmatrix} \tag{9}$$

Where:

$$[d]=\begin{bmatrix}\dfrac{\partial}{\partial r} & 0\\ \dfrac{1}{r} & 0\\ 0 & \dfrac{\partial}{\partial z}\\ \dfrac{1}{2}\dfrac{\partial}{\partial z} & \dfrac{1}{2}\dfrac{\partial}{\partial r}\end{bmatrix}$$

Based on the Hooke's law, the stress-strain relationship is:

$$[\sigma]=\begin{bmatrix}\sigma_{rr}\\ \sigma_{\theta\theta}\\ \sigma_{zz}\\ \tau_{rz}\end{bmatrix}=[D][\varepsilon] \tag{10}$$

Where:

$$[D]=\frac{E}{(1+\upsilon)(1-2\upsilon)}\times\begin{bmatrix}1-\upsilon & \upsilon & \upsilon & 0\\ \upsilon & 1-\upsilon & \upsilon & 0\\ \upsilon & \upsilon & 1-\upsilon & 0\\ 0 & 0 & 0 & 1-2\upsilon\end{bmatrix}=E\,\mathbf{\Lambda} \tag{11}$$

In "Eq. (11)", E is the Young's modulus, which is a function of r and z components. Also, υ denotes Poisson's ratio, and it is constant.

The cylinder has simply supported boundary conditions, so displacement boundary conditions are as follows:

$$\mathrm{u}(\mathrm{r},0)=\mathrm{u}(\mathrm{r},\mathrm{L})=0 \qquad \text{S-S} \tag{12}$$

4 FINITE ELEMENT MODELLING

The finite element method is used to solve the governing Equations for 2D-FGM thick hollow cylinders. The displacement matrix of each element (e) in terms of the nodal displacement matrix $\{\delta\}$ and shape function $\boldsymbol{N}$ is:

$$\{f\}^{(e)}=\boldsymbol{N}^{(e)}\{\delta\}^{(e)} \tag{13}$$

By substituting "Eq. (13)" into "Eq. (9)", the strain matrix of the element (e) is determined as:

$$\{\varepsilon\}^{(e)}=\boldsymbol{B}^{(e)}\{\delta\}^{(e)} \tag{14}$$

Where $\boldsymbol{B}^{(e)}=[d]\boldsymbol{N}^{(e)}$ is the strain-displacement matrix. $\boldsymbol{N}^{(e)}$ matrix is as follows for the quadratic six nodded triangular element:

$$\boldsymbol{N}=\begin{bmatrix}N_1 & 0 & N_2 & 0 & N_3 & 0 & N_4 & 0 & N_5 & 0 & N_6 & 0\\ 0 & N_1 & 0 & N_2 & 0 & N_3 & 0 & N_4 & 0 & N_5 & 0 & N_6\end{bmatrix} \tag{15}$$

Where:

$$N_1=\frac{\left(r_{23}(z-z_3)-z_{23}(r-r_3)\right)\left(r_{46}(z-z_6)-z_{46}(r-r_6)\right)}{\left(r_{23}z_{13}-z_{23}r_{13}\right)\left(r_{46}z_{16}-z_{46}r_{16}\right)}$$

$$N_2=\frac{\left(r_{31}(z-z_1)-z_{31}(r-r_1)\right)\left(r_{54}(z-z_4)-z_{54}(r-r_4)\right)}{\left(r_{31}z_{21}-z_{31}r_{21}\right)\left(r_{54}z_{24}-z_{54}r_{24}\right)}$$

$$N_3=\frac{\left(r_{21}(z-z_1)-z_{21}(r-r_1)\right)\left(r_{56}(z-z_6)-z_{56}(r-r_6)\right)}{\left(r_{21}z_{31}-z_{21}r_{31}\right)\left(r_{56}z_{36}-z_{56}r_{36}\right)} \tag{16}$$

$$N_4 = \frac{\left(r_{31}\left(z - z_1\right) - z_{31}\left(r - r_1\right)\right)\left(r_{23}\left(z - z_3\right) - z_{23}\left(r - r_3\right)\right)}{\left(r_{31}z_{41} - z_{31}r_{41}\right)\left(r_{23}z_{43} - z_{23}r_{43}\right)}$$

$$N_5 = \frac{\left(r_{31}\left(z - z_1\right) - z_{31}\left(r - r_1\right)\right)\left(r_{21}\left(z - z_1\right) - z_{21}\left(r - r_1\right)\right)}{\left(r_{31}z_{51} - z_{31}r_{51}\right)\left(r_{21}z_{51} - z_{21}r_{51}\right)}$$

$$N_6 = \frac{\left(r_{21}\left(z - z_1\right) - z_{21}\left(r - r_1\right)\right)\left(r_{23}\left(z - z_3\right) - z_{23}\left(r - r_3\right)\right)}{\left(r_{21}z_{61} - z_{21}r_{61}\right)\left(r_{23}z_{63} - z_{23}r_{63}\right)}$$

Where r_i and z_i are the radial and axial coordinates of the ith node, respectively.

$$r_{ij} = r_i - r_j,$$
$$z_{ij} = z_i - z_j$$

And $\boldsymbol{B}^{(e)}$ matrix is:

$$\boldsymbol{B} = \begin{bmatrix} \frac{\partial N_1}{\partial r} & 0 & \frac{\partial N_2}{\partial r} & 0 & \frac{\partial N_3}{\partial r} & 0 & \frac{\partial N_4}{\partial r} & 0 & \frac{\partial N_5}{\partial r} & 0 & \frac{\partial N_6}{\partial r} & 0 \\ \frac{1}{r}N_1 & 0 & \frac{1}{r}N_2 & 0 & \frac{1}{r}N_3 & 0 & \frac{1}{r}N_4 & 0 & \frac{1}{r}N_5 & 0 & \frac{1}{r}N_6 & 0 \\ 0 & \frac{\partial N_1}{\partial z} & 0 & \frac{\partial N_2}{\partial z} & 0 & \frac{\partial N_3}{\partial z} & 0 & \frac{\partial N_4}{\partial z} & 0 & \frac{\partial N_5}{\partial z} & 0 & \frac{\partial N_6}{\partial z} \\ \frac{1}{2}\frac{\partial N_1}{\partial z} & \frac{1}{2}\frac{\partial N_1}{\partial r} & \frac{1}{2}\frac{\partial N_2}{\partial z} & \frac{1}{2}\frac{\partial N_2}{\partial r} & \frac{1}{2}\frac{\partial N_3}{\partial z} & \frac{1}{2}\frac{\partial N_3}{\partial r} & \frac{1}{2}\frac{\partial N_4}{\partial z} & \frac{1}{2}\frac{\partial N_4}{\partial r} & \frac{1}{2}\frac{\partial N_5}{\partial z} & \frac{1}{2}\frac{\partial N_5}{\partial r} & \frac{1}{2}\frac{\partial N_6}{\partial z} & \frac{1}{2}\frac{\partial N_6}{\partial r} \end{bmatrix} \tag{17}$$

Which the components of $\boldsymbol{B}^{(e)}$ matrix are presented in Appendix A.

The material inhomogeneity of the FG hollow cylinder can be defined using nodal values. Consequently, a graded finite element approach can be utilized to accurately capture smooth variations in material properties at the element level. FGM modeling using graded elements yields more precise results than partitioning the solution domain into homogeneous elements. So, shape functions similar to those of the displacement components can be used:

$$E = \sum_{i=1}^{6} E_i \; N_i = \square \; \boldsymbol{\Xi} \tag{18}$$

$$\rho = \sum_{i=1}^{6} \rho_i \; N_i = \square \; \Re \tag{19}$$

where E_i and ρ_i are the modulus of elasticity and mass density corresponding to i^{th} node. $\square$, $\boldsymbol{\Xi}$ and $\Re$ are vectors of shape functions, modulus of elasticity, and mass densities of each element, respectively, and are defined as follows:

$$\mathrm{N} = [N_1 \quad \ldots \quad N_6]_{1\times 6},$$
$$\boldsymbol{\Xi} = [E_1 \quad \ldots \quad E_6]^T{}_{1\times 6},$$
$$\rho = [\rho_1 \quad \cdots \quad \rho_6]^T{}_{1\times 6} \tag{20}$$

Therefore, “Eq. (11)” may be rewritten as:

$$\mathbf{D} = \square \; \boldsymbol{\Xi} \boldsymbol{\Lambda} \tag{21}$$

Based on the principle of minimum potential energy and the Rayleigh-Ritz method, governing Equations can be derived. The total potential energy of the rotating 2D-FGM thick hollow cylinder can be written as:

$$\Pi^{(e)} = \frac{1}{2}\int_{V^{(e)}} \left(\boldsymbol{\varepsilon}^{(e)}\right)^T \boldsymbol{\sigma}^{(e)} dV - \int_{A^{(e)}} (\boldsymbol{q})^T \Gamma dV = \frac{1}{2}\int_{V(e)} \left(\boldsymbol{\delta}^{(e)}\right)^T \boldsymbol{B}^T (\boldsymbol{\Xi\Lambda}) \boldsymbol{B}\, \boldsymbol{\delta}^{(e)} dV - \int_{A(e)} \left(\boldsymbol{\delta}^{(e)}\right)^T \boldsymbol{N}^T \Gamma dV \tag{22}$$

Utilizing the principle of minimum total potential energy leads to:

$$\frac{\partial \Pi^{(e)}}{\partial \left(\boldsymbol{\delta}^{(e)}\right)^T} = 0$$
$$\Rightarrow \left(\int_{V^{(e)}} \mathbf{B}^T (\square \; \boldsymbol{\Xi\Lambda}) \mathbf{B} dV\right) \boldsymbol{\delta}^{(e)} = \int_{A^{(e)}} \mathbf{N}^T \Gamma dV \tag{23}$$

In compact form:

$$\mathbf{K}^{(e)} \boldsymbol{\delta}^{(e)} = F^{(e)} \tag{24}$$

Where:

$$\boldsymbol{K}^{(e)} = \int_{V_{(e)}} \mathbf{B}^T (\square \; \boldsymbol{\Xi\Lambda}) \mathbf{B} \; dV \tag{25}$$

$$F^{(e)} = \int_{A^{(e)}} \mathbf{N}^T \Gamma dV \quad , \quad \Gamma = \begin{bmatrix} \Gamma_r \\ 0 \end{bmatrix} \tag{26}$$

$\mathit{\Gamma}_r$ is defined as follows:

$$\mathit{\Gamma}_r = \rho r\omega^2 = \square\,\Re r\omega^2 \qquad (27)$$

Therefore, the finite element form of the governing Equations of FG thick hollow cylinder will written as:

$$\mathbf{K\delta} = F \qquad (28)$$

5 RESULTS

5.1. Verification of Solving Method

To validate the results of this study, a comparison was made between the radial displacement findings of the current research and those obtained from ANSYS WORKBENCH (“Fig. 4”). Accordingly, in relationships, it is assumed that $(n_r,\ n_z)$ are zero. Therefore, the cylinder is homogeneous and is made of m_2. The following parameters were used for validation.

a=1 (m), b=1.5 (m), L=1, E=69GPa, ρ=2715, ω =100 rad/s and ν =0.3.

A good agreement was observed for the radial displacement of the cylinder at z=$\frac{L}{2}$.

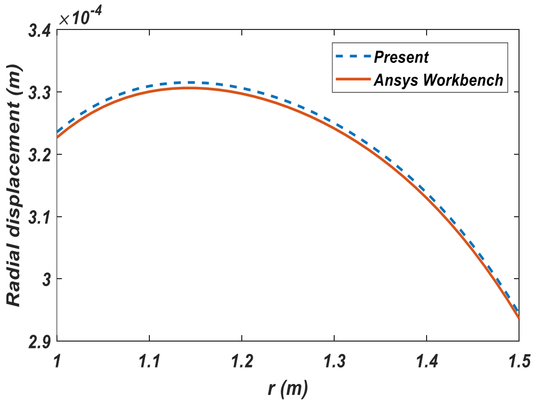

Fig. 4 Comparison between the radial displacement of the present study and Ansys Workbench.

5.2. Numerical Results

Numerical results have been studied for 2D-FGM rotating thick hollow cylinders. The effects of angular velocity and various power law exponents on the displacements and stress distributions have been investigated. The values of the parameters are:

a=1 (m), b=1.5 (m), L=1 (m),
ω =100 rad/s and ν =1/3.

The effect of the different power law exponents on the radial displacement at z=$\frac{L}{2}$ of the simply supported 2D-FGM thick hollow cylinder is depicted in “Fig. 5”.

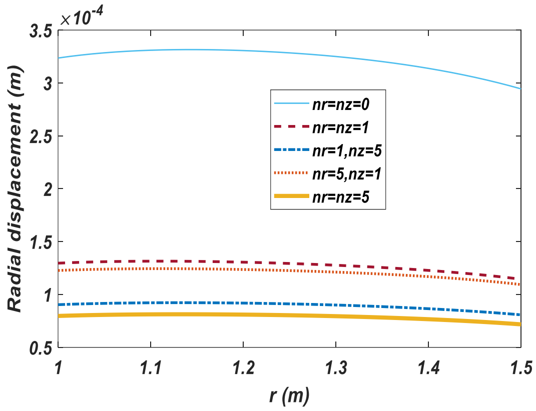

Fig. 5 Radial displacement at z=L/2 for different power law exponents.

It can be seen that the maximum radial displacement belongs to $n_r = n_z$=0. In this case, the cylinder is made of m₂, and it has minimum stiffness. Also, the minimum displacement occurs for $n_r = n_z$=5 with maximum stiffness. Figures 6-8 explain the effect of power law exponents on the radial, tangential, and axial stresses at z=$\frac{L}{2}$, respectively. Results show that the axial stresses are less affected by power law exponents, but tangential and radial stresses are mainly affected. Also, results show that maximum and minimum stresses belong to n_r=5, n_z=1, and n_r=n_z=0, respectively.

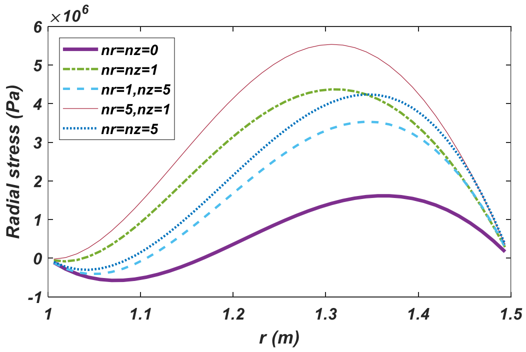

Fig. 6 Radial stress at z=L/2 for different power law exponents.

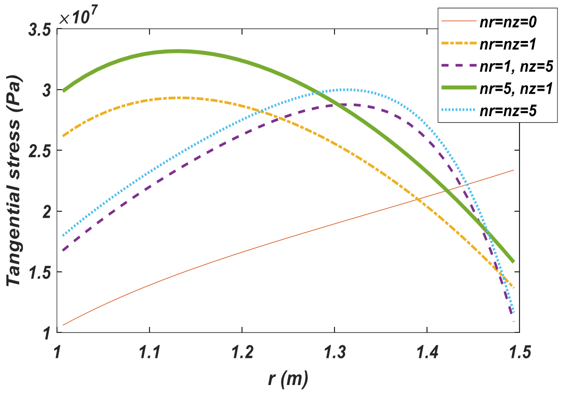

Fig. 7 Tangential stress at z=L/2 for different power law exponents.

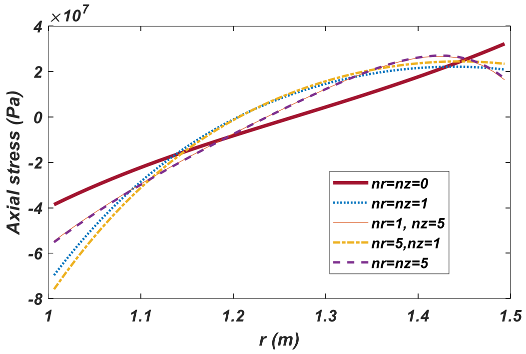

Fig. 8 Distribution of the axial stress at z=L/2 for different power law exponents.

Distribution of radial displacement, radial, tangential, and axial stresses for power law exponents n_r=1, n_z=5 are shown in "Fig. 9". The effect of the circular velocity on the radial stress at z=$\frac{L}{2}$ for the simply supported 2D-FGM thick hollow cylinder is shown in "Fig. 10". Radial stress is increased as angular velocity increases.

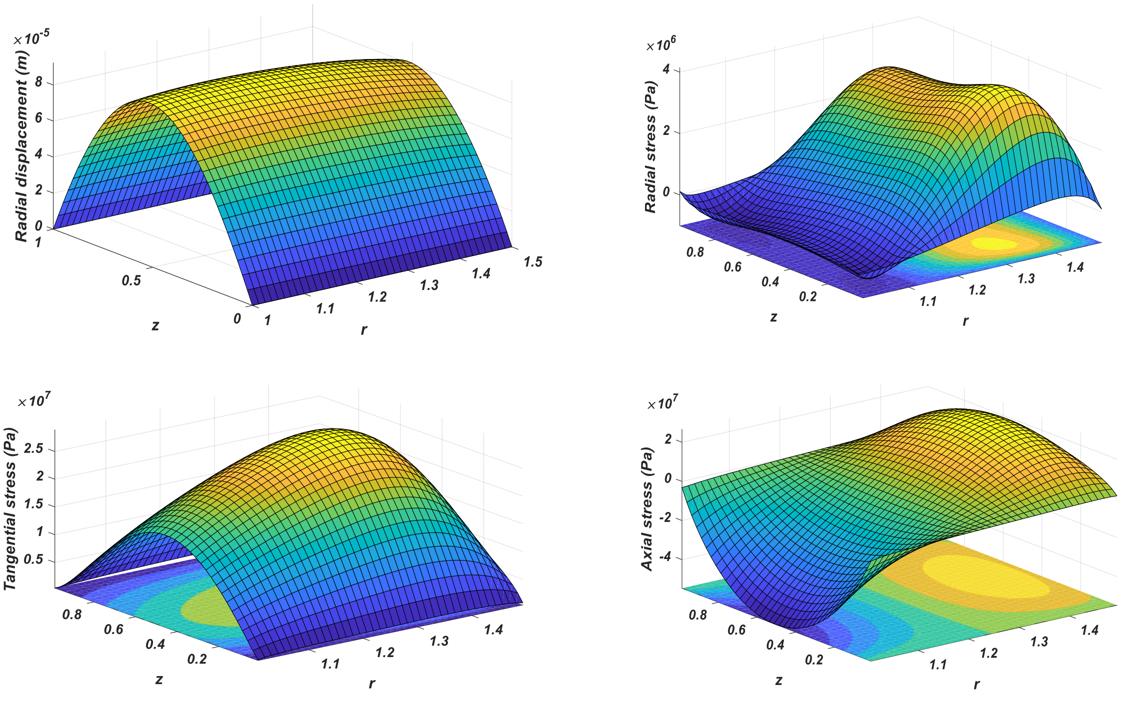

Fig. 9 Radial displacement, radial, tangential, and axial stresses for n_r=1, n_z=5.

Int. J. Advanced Design and Manufacturing Technology, 2025, Vol. 18, No. 2, pp. 71-80

DOI: ***ISSN: 2252-0406*** ***https://admt.isfahan.iau.ir***

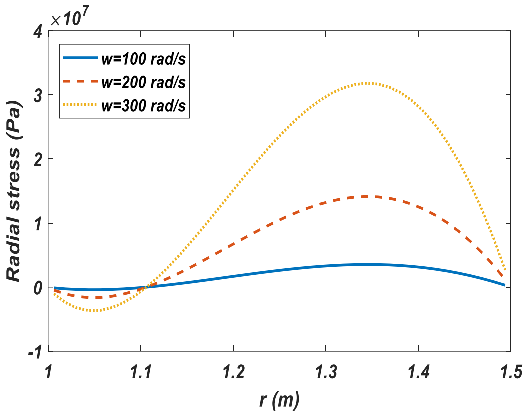

Fig. 10 Radial stress at z=L/2 for different rotational velocities.

6 CONCLUSIONS

This pioneering analysis introduces 2D axisymmetric elasticity modeling to evaluate stress distributions in rotating two-dimensional functionally graded thick hollow cylinders for the first time. The graded finite element method and Rayleigh-Ritz energy formulation were strategically employed to solve governing Equations.

The effects of power law exponents and angular velocity on displacement and stress distributions were examined. Based on the results, 2D-FGM utilization leads to a better design to control both the maximum stresses and stress distribution by changing the material distribution. The main results of the present study are:

- Maximum radial displacement belongs to $n_r=n_z=0$. Also, the minimum displacement belongs to $n_r=n_z=5$ with maximum stiffness.
- The axial stresses are less affected by power law exponents, but tangential and radial stresses are mainly affected. Also, maximum and minimum stresses belong to $n_r=5$, $n_z=1$, and $n_r=n_z=0$, respectively.
- Radial stress increased by increasing the angular velocity.

APPENDIX A

$$\frac{\partial N_1}{\partial r}=\frac{-z_{23}[r_{46}(z-z_6)-z_{46}(r-r_6)]-z_{46}[r_{23}(z-z_3)-z_{23}(r-r_3)]}{(r_{23}z_{13}-z_{23}r_{13})(r_{46}z_{16}-z_{46}r_{16})}$$

$$\frac{\partial N_1}{\partial z}=\frac{r_{23}[r_{36}(z-z_6)-z_{36}(r-r_6)]+r_{46}[r_{13}(z-z_3)-z_{13}(r-r_3)]}{(r_{23}z_{13}-z_{23}r_{13})(r_{46}z_{16}-z_{46}r_{16})}$$

$$\frac{\partial N_2}{\partial r}=\frac{-z_{31}[r_{54}(z-z_4)-z_{54}(r-r_4)]-z_{54}[r_{31}(z-z_1)-z_{31}(r-r_1)]}{(r_{21}z_{51}-z_{21}r_{51})(r_{21}z_{51}-z_{21}r_{43})}$$

$$\frac{\partial N_2}{\partial z}=\frac{r_{31}[r_{54}(z-z_4)-z_{54}(r-r_4)]+r_{54}[r_{21}(z-z_1)-z_{31}(r-r_1)]}{(r_{21}z_{21}-z_{31}r_{21})(r_{54}z_{24}-z_{54}r_{24})}$$

$$\frac{\partial N_3}{\partial r}=\frac{-z_{21}[r_{56}(z-z_6)-z_{56}(r-r_6)]-z_{56}[r_{21}(z-z_1)-z_{21}(r-r_1)]}{(r_{21}z_{31}-z_{21}r_{31})(r_{56}z_{36}-z_{56}r_{36})}$$

$$\frac{\partial N_3}{\partial z}=\frac{r_{21}[r_{56}(z-z_6)-z_{56}(r-r_6)]+r_{56}[r_{21}(z-z_1)-z_{21}(r-r_1)]}{(r_{21}z_{31}-z_{21}r_{31})(r_{56}z_{36}-z_{56}r_{36})}$$

$$\frac{\partial N_4}{\partial r}=\frac{-z_{21}[r_{23}(z-z_3)-z_{22}(r-r_2)]-z_{23}\left(r_{31}(z-z_1)-z_{31}(r-r_4)\right)}{(r_{31}z_{41}-z_{31}r_{41})(r_{23}z_{43}-z_{23}r_{43})}$$

$$\frac{\partial N_4}{\partial z}=\frac{r_{21}[r_{23}(z-z_2)-z_{23}(r-r_2)]+r_{23}[r_{21}(z-z_1)-z_{31}(r-r_1)]}{(r_{21}z_{41}-z_{21}r_{41})(r_{23}z_{43}-z_{23}r_{43})}$$

$$\frac{\partial N_5}{\partial r}=\frac{-z_{31}[r_{21}(z-z_1)-z_{21}(r-r_1)]-z_{21}[r_{31}(z-z_1)-z_{31}(r-r_1)]}{(r_{21}z_{51}-z_{21}r_{51})(r_{21}z_{51}-z_{21}r_{43})}$$

$$\frac{\partial N_5}{\partial z}=\frac{r_{31}[r_{21}(z-z_1)-z_{21}(r-r_1)]+\mathrm{r}_{21}[\mathrm{r}_{21}(\mathrm{z}-\mathrm{z}_1)-\mathrm{z}_{31}(\mathrm{r}-\mathrm{r}_1)]}{(\mathrm{r}_{31}\mathrm{z}_{51}-\mathrm{z}_{31}\mathrm{r}_{51})(\mathrm{r}_{21}\mathrm{z}_{51}-\mathrm{z}_{21}\mathrm{r}_{51})}$$

$$\frac{\partial \mathrm{N}_6}{\partial \mathrm{r}}=\frac{-\mathrm{z}_{21}[\mathrm{r}_{23}(\mathrm{z}-\mathrm{z}_3)-\mathrm{z}_{23}(\mathrm{r}-\mathrm{r}_3)]-\mathrm{z}_{21}[\mathrm{r}_{21}(\mathrm{z}-\mathrm{z}_1)-\mathrm{z}_{31}(\mathrm{r}-\mathrm{r}_1)]}{(\mathrm{r}_{21}\mathrm{z}_{61}-\mathrm{z}_{21}\mathrm{r}_{61})(\mathrm{r}_{23}\mathrm{z}_{63}-\mathrm{z}_{23}\mathrm{r}_{63})}$$

$$\frac{\partial \mathrm{N}_6}{\partial \mathrm{z}}=\frac{\mathrm{r}_{21}[\mathrm{r}_{23}(\mathrm{z}-\mathrm{z}_3)-\mathrm{z}_{23}(\mathrm{r}-\mathrm{r}_3)]+\mathrm{r}_{23}[\mathrm{r}_{31}(\mathrm{z}-\mathrm{z}_1)-\mathrm{z}_{31}(\mathrm{r}-\mathrm{r}_1)]}{(\mathrm{r}_{21}\mathrm{z}_{61}-\mathrm{z}_{21}\mathrm{r}_{61})(\mathrm{r}_{23}\mathrm{z}_{63}-\mathrm{z}_{23}\mathrm{r}_{63})}$$

Parameters

a	inner radius of cylinder
b	outer radius of cylinder
L	cylinder length
$\mathrm{n_r}$	nonnegative radial volume fraction exponents
$\mathrm{n_z}$	nonnegative axial volume fraction exponents
$\mathrm{Vc_1}$	volume fraction of first ceramic
$\mathrm{Vc_2}$	volume fraction of second ceramic
$\mathrm{Vm_1}$	volume fraction of first metal
$\mathrm{Vm_2}$	volume fraction of second metal
E_i	modulus of elasticity of ith node

Research paper

COPYRIGHTS
© 2025 by the authors. Licensee Islamic Azad University Isfahan Branch. This article is an open access article distributed under the terms and conditions of the Creative Commons Attribution 4.0 International (CC BY 4.0) (https://creativecommons.org/licenses/by/4.0/)

OPEN ACCESS

ρ_i	mass density of ith node
□	vectors of shape functions
$\boldsymbol{\Xi}$	modulus of elasticity of each element
$\Re$	mass densities of each element
$V^{(e)}$	volume of the element
Γ	body force vector due to rotational velocity
Γ_r	components of body force in the r-direction

REFERENCES

[1] Shi, P., Xie, J., Exact Solution of Magneto-Elastoplastic Problem of Functionally Graded Cylinder Subjected to Internal Pressure, Applied Mathematical Modelling, Vol. 123, 2023, pp. 835-855,

[2] Li, X., Xie, J., and Shi, P., Magneto-Thermal–Mechanical Analysis of Functionally Graded Rotating Cylinder and Circular Disk, Archive of Applied Mechanics, Vol. 93, 2023, pp. 1449-1457.

[3] Yarımpabuç, D., Çalıskan, A. J. C. M., Computations, Applications: An International Journal, "Elastic Analysis of Functionally Graded Rotating Pressurized Cylinders, Vol. 15, 2023.

[4] Daghigh, V., Edalati, H., Daghigh, H., Belk, D. M., and Nikbin, K., Time-Dependent Creep Analysis of Ultra-High-Temperature Functionally Graded Rotating Disks of Variable Thickness, Forces in Mechanics, Vol. 13, 2023, pp. 100235.

[5] Seddighi, H., Ghannad, M., and Loghman, A.,Creep Behavior of Cylinders Subjected to an Internal Pressure and a Two Dimensional Temperature Field Using First Order Shear Deformation Theory, Journal of Solid Mechanics, Vol. 15, 2023, pp. 327-342.

[6] Omidi Bidgoli, M., Loghman, A., Arefi, M., and Faegh, R. K., Transient Stress and Deformation Analysis of A Shear Deformable FG Rotating Cylindrical Shell Made of AL-SIC Subjected to Thermo-Mechanical Loading, Australian Journal of Mechanical Engineering, Vol. 21, 2023, pp. 279-294.

[7] Maitra, K., Singh Parihar, R., Finite Element Analysis of Rotating Truncated Functionally Graded Conical Shell, Current Materials Science: Formerly: Recent Patents on Materials Science, Vol. 16, 2023, pp. 62-71.

[8] Saadatfar, M., Babazadeh, M. A., and Babaelahi, M., Creep Analysis in A Rotating Variable Thickness Functionally Graded Disc with Convection Heat Transfer and Heat Source, Mechanics of Time-Dependent Materials, 2023.

[9] Babaei, M., Asemi, K., and Kiarasi, F., Dynamic Analysis of Functionally Graded Rotating Thick Truncated Cone Made of Saturated Porous Materials, Thin-Walled Structures, Vol. 164, 2021, pp. 107852.

[10] Xu, C., Yu, Z. X., and Du, F., Dynamic Analysis of A Thick Hollow Cylinder Made of Two-Dimensional Functionally Graded Material Using Time-Domain Spectral Element Method, Mechanics of Advanced Materials and Structures, Vol. 26, 2019, pp. 1518-1535.

[11] Yarımpabuç, D., Transient-Thermoelastic Analysis of Periodically Rotated Functionally Graded Hollow Cylinder, Journal of Engineering Mathematics, Vol. 128, 2021, pp. 18.

[12] Jabbari and M., Nejad, M. Z., Mechanical and Thermal Stresses in Radially Functionally Graded Hollow Cylinders with Variable Thickness Due to Symmetric Loads, Australian Journal of Mechanical Engineering, Vol. 18, 2020, pp. S108-S121.

[13] Mehditabar, A., Rahimi, G. H., and Tarahhomi, M. H., Thermo-Elastic Analysis of A Functionally Graded Piezoelectric Rotating Hollow Cylindrical Shell Subjected to Dynamic Loads, Mechanics of Advanced Materials and Structures, Vol. 25, 2018, pp. 1068-1079.

[14] Gharibi, M., Zamani Nejad, M., and Hadi, A., Elastic Analysis of Functionally Graded Rotating Thick Cylindrical Pressure Vessels with Exponentially-Varying Properties Using Power Series Method of Frobenius, Journal of Computational Applied Mechanics, Vol. 48, 2017, pp. 89-98.

[15] Jabbari, M., Nejad, M. Z., and Ghannad, M., Thermo-Elastic Analysis of Axially Functionally Graded Rotating Thick Cylindrical Pressure Vessels With Variable Thickness Under Mechanical Loading, International Journal of Engineering Science, Vol. 96, 2015, pp. 1-18.

[16] Jafari Fesharaki, J., Jafari Fesharaki, V., Yazdipoor, M., and Razavian, B., Two-Dimensional Solution for Electro-Mechanical Behavior of Functionally Graded Piezoelectric Hollow Cylinder, Applied Mathematical Modelling, Vol. 36, 2012, pp. 5521-5533.

[17] Zafarmand, H., Hassani, B., Analysis of Two-Dimensional Functionally Graded Rotating Thick Disks with Variable Thickness, Acta Mechanica, Vol. 225, 2014, pp. 453-464.

[18] Dai, H. L., Dai, T., and Zheng, H. Y., Stresses Distributions in A Rotating Functionally Graded Piezoelectric Hollow Cylinder, Meccanica, Vol. 47, 2012, pp. 423-436.

[19] Shishesaz, M., Hosseini, M., Naderan Tahan, K., and Hadi, A., Analysis of Functionally Graded Nanodisks Under Thermoelastic Loading Based on The Strain Gradient Theory, Acta Mechanica, Vol. 228, 2017, pp. 4141-4168.

[20] Koohi Faegh Dehkourdi, R., Omidi Bidgoli, M., and Hosseini, M., A Case Study on the Influence of Friction Coefficient and Rotational Speed on Transient Thermoelastic Response of FGM Rotating Cylinder %J Mechanics Of Advanced Composite Structures, Mechanics Of Advanced Composite Structures, Vol. 9, 2022, pp. 399-408.

[21] Babaei, M., Kiarasi, F., Asemi, K., and Hosseini, M., Functionally Graded Saturated Porous Structures: A Review, Journal of Computational Applied Mechanics, Vol. 53, 2022, pp. 297-308.

[22] Shishesaz, M., Hosseini, M., Mechanical Behavior of Functionally Graded Nano-Cylinders Under Radial Pressure Based on Strain Gradient Theory, Journal of Mechanics, Vol. 35, 2018, pp. 441-454.

[23] Nejad, M. Z., Hadi, A., Non-Local Analysis of Free Vibration of Bi-Directional Functionally Graded Euler–Bernoulli Nano-Beams, International Journal of Engineering Science, Vol. 105, 2016, pp. 1-11.

[24] Shariati, M., Shishesaz, M., Mosalmani, R., Seyed Roknizadeh, S. A., and Hosseini, M., Nonlocal Effect on The Axisymmetric Nonlinear Vibrational Response of Nano-Disks Using Variational Iteration Method, Journal of Computational Applied Mechanics, Vol. 52, 2021, pp. 507-534.

[25] Barati, A., Hadi, A., Nejad, M. Z., and Noroozi, R., On Vibration of Bi-Directional Functionally Graded Nanobeams Under Magnetic Field, Mechanics Based Design of Structures and Machines, Vol. 50, 2022, pp. 468-485.

[26] Mohammadi, M., Hosseini, M., Shishesaz, M., Hadi, A., and Rastgoo, A., Primary and Secondary Resonance Analysis of Porous Functionally Graded Nanobeam Resting on A Nonlinear Foundation Subjected to Mechanical and Electrical Loads, European Journal of Mechanics - A/Solids, Vol. 77, 2019, pp. 103793.

[27] Haghshenas Gorgani, H., Mahdavi Adeli, M., and Hosseini, M., Pull-in Behavior of Functionally Graded Micro/Nano-Beams for MEMS and NEMS switches, Microsystem Technologies, Vol. 25, 2019, pp. 3165-3173.

[28] Hosseini, M., Hadi, A., Malekshahi, A., and Shishesaz, M., A Review of Size-Dependent Elasticity for Nanostructures, Journal of Computational Applied Mechanics, Vol. 49, 2018, pp. 197-211.

[29] kiarasi, F., babaei, M., Sarvi, P., asemi, K., hosseini, M., and Omidi Bidgoli, M., A Review on Functionally Graded Porous Structures Reinforced by Graphene Platelets, Journal of Computational Applied Mechanics, Vol. 52, 2021, pp. 731-750.

[30] Shariati, M., Shishesaz, M., Sahbafar, H., Pourabdy, M., and Hosseini, M., A Review on Stress-Driven Nonlocal Elasticity Theory, Journal of Computational Applied Mechanics, Vol. 52, 2021, pp. 535-552.

[31] M. Khatoonabadi, M. Jafari, F. Kiarasi, M. Hosseini, M. Babaei, and K. Asemi, "Shear buckling response of FG porous annular sector plate reinforced by graphene platelet subjected to different shear loads %J Journal of Computational Applied Mechanics," vol. 54, pp. 68-86, 2023.

[32] Daneshmehr, A., Rajabpoor, A., and Hadi, A., Size Dependent Free Vibration Analysis of Nanoplates Made of Functionally Graded Materials Based on Nonlocal Elasticity Theory with High Order Theories, International Journal of Engineering Science, Vol. 95, 2015, pp. 23-35.

[33] Barati, A., Mousavi Khoram, M., Shishesaz, M., and Hosseini, M., Size-Dependent Thermoelastic Analysis of Rotating Nanodisks of Variable Thickness, Journal of Computational Applied Mechanics, Vol. 51, 2020, pp. 340-360.

[34] Shishesaz, M.,, Shariati, M., and Hosseini, M., Size-Effect Analysis on Vibrational Response of Functionally Graded Annular Nano-Plate Based on Nonlocal Stress-Driven Method, International Journal of Structural Stability and Dynamics, pp. 2250098.

[35] Barati, A., Adeli, and M. M., Hadi, A., Static Torsion of Bi-Directional Functionally Graded Microtube Based on the Couple Stress Theory Under Magnetic Field, International Journal of Applied Mechanics, Vol. 12, 2020, pp. 2050021.

[36] Hosseini, M., Shishesaz, M., Tahan, K. N., and Hadi, A., Stress Analysis of Rotating Nano-Disks of Variable Thickness Made of Functionally Graded Materials, International Journal of Engineering Science, Vol. 109, 2016, pp. 29-53.

[37] Hosseini, M., Shishesaz, M., and Hadi, A., Thermoelastic Analysis of Rotating Functionally Graded Micro/Nanodisks of Variable Thickness, Thin-Walled Structures, Vol. 134, 2019, pp. 508-523.

[38] Noroozi, R., Barati, A., Kazemi, A., Norouzi, S., and Hadi, A., Torsional Vibration Analysis of Bi-Directional FG Nano-Cone with Arbitrary Cross-Section Based on Nonlocal Strain Gradient Elasticity, Advances in Nano Research, Vol. 8, 2020, pp. 13-24.

[39] Zarezadeh, E., Hosseini, V., and Hadi, A., Torsional Vibration of Functionally Graded Nano-Rod Under Magnetic Field Supported by A Generalized Torsional Foundation Based on Nonlocal Elasticity Theory, Mechanics Based Design of Structures and Machines, 2019, pp. 1-16.

[40] Mahmoudi, R., Barati, A., Hosseini, M., and Hadi, A., Torsional Vibration of Functionally Porous Nanotube Based on Nonlocal Couple Stress Theory, International Journal of Applied Mechanics, pp. 2150122.

[41] Adeli, M. M., Hadi, A., Hosseini, M., and Gorgani, H. H., Torsional Vibration of Nano-Cone Based on Nonlocal Strain Gradient Elasticity Theory, The European Physical Journal Plus, Vol. 132, 2017, pp. 393.

[42] Mohammadi, M., Farajpour, A., Moradi, A., and Hosseini, M., Vibration Analysis of The Rotating Multilayer Piezoelectric Timoshenko Nanobeam, Engineering Analysis with Boundary Elements, Vol. 145, 2022, pp. 117-131.

[43] Shariati, M., Hosseini, M., and Nakhli sahraei, M., Vibration of Nano-Disks Using Adomian Decomposition Method Based on Nonlocal Mindlin Plate Theory, presented at the The 30th Annual International Conference of Iranian Society of Mechanical Engineers Iran, Tehran, 2022.

[44] Hadi, A., Nejad, M. Z., and Hosseini, M., Vibrations of Three-Dimensionally Graded Nanobeams, International Journal of Engineering Science, Vol. 128, 2018, pp. 12-23.